Functionality enhancement of low-dimensional inorganic materials by nano-structure control

低次元無機化合物のナノ構造制御による高機能化

January 2010

Tomoyuki IWATA

岩 田 知 之

Functionality enhancement of low-dimensional inorganic materials by nano-structure control

低次元無機化合物のナノ構造制御による高機能化

January 2010

Tomoyuki IWATA
岩田　知之

Contents

Chapter 1

Introduction

1.1 Recent advances in the field of crystal structure analyses from X-ray powder diffraction data

Recent advances in the field of crystal-structure analysis from X-ray powder diffraction (XRPD) data have enabled us to investigate complex structures, including positional disordering of atoms and orientational disordering of atomic groups. A combined use of the Rietveld method, the maximum-entropy method (MEM) and the MEM-based pattern fitting (MPF) method has enabled us to disclose new structural details. However, the Rietveld method and MEM have a drawback in determining the electron density distributions because the observed structure factors, F_o(Rietveld), are biased toward the structural model assuming intensity partitioning. On the other hand, the MPF method can minimize the structural bias. Thus, the MEM and MPF analyses are alternately repeated (REMEDY cycle) until the reliability indices reach minima. Crystal structures can be seen clearly from electron-density distributions (EDD) determined by MPF.

In *Chapter 2*, the author has applied the combied use of MEM and MPF to the structural analyses of $Ca_{12}Al_{14}O_{32}Cl_2$ and $Ba_3MgSi_2O_8$. The latter structural model was originated from that of glaserite ($K_3Na(SO_4)_2$) and modified by a split-atom model. The EDD determined by MPF was used to verify the split-atom model.

1.2 Syntheses, crystal structures and thermoelectric properties of new layered carbides

In the system Zr-Al-C, there are two ternary carbides reported so far; they are $(ZrC)_2Al_3C_2$ and $(ZrC)_3Al_3C_2$. These carbides form a homologous series with the general formula of $(ZrC)_nAl_3C_2$ ($n = 2$ and 3). The crystals show the intergrowth structures with alternating layers of $[Zr_nC_{n+1}]$ and $[Al_3C_3]$. In the system U-Al-C, there are two types of ternary carbides $(UC)_2Al_3C_2$ and $(UC)Al_3C_2$. The former carbide is isostructural with $(ZrC)_2Al_3C_2$. The latter carbide, together with $(ScC)Al_3C_2$ and $(YC)Al_3C_2$, can be regarded as the intergrowth structure consisting of the $[RC_2]$ slabs separated by the Al_4C_3-type $[Al_3C_3]$ layers, where $R = U$, Sc and Y. Accordingly, these layered carbides are of the members with $n = 1$ for the homologous series $(RC)_nAl_3C_2$ ($R = Zr$, U, Sc and Y, $n = 1$, 2 and 3).

Recent efforts in our laboratory have aimed at defining a new homologous series of phases $(ZrC)_l(Al_4C_3)_m$ (l, m = integers). Members of this series that have been confirmed so far include $(ZrC)_2Al_4C_3$ ($l = 2$, $m = 1$), $(ZrC)_3Al_4C_3$ ($l = 3$, $m = 1$), $(ZrC)(Al_4C_3)_2$ ($l = 1$, $m = 2$) and $(ZrC)_2(Al_4C_3)_2$ ($l = 2$, $m = 2$). These compounds exhibit a close structural and compositional relationship; the crystal structures can be regarded as intergrowth structures consisting of the Al_4C_3-type $[Al_{4m}C_{3m+1}]$ layers separated by the NaCl-type $[Zr_lC_{l+1}]$ layers. These two types of layers share the two-dimensional networks of carbon atoms at their boundaries. The C-C distances of the networks, ranging from 0.3318 to 0.3328 nm, are comparable to those of ZrC and Al_4C_3 crystals; the former distance is 0.3319 nm (= $a(ZrC)/\sqrt{2}$) and that of the latter is 0.3335 nm (= $a(Al_4C_3)$), where $a(ZrC)$ and $a(Al_4C_3)$ represent the a-axis lengths. Fukuda *et al.* have therefore proposed that the closeness of the C-C distances between ZrC and Al_4C_3 crystals, being repressed by the equation $a(ZrC)/\sqrt{2} \approx a(Al_4C_3)$, is the principal reason for the formation of these layered carbides.

The $[Al_{4m}C_{3m+1}]$ layers were incorporated by several amounts of Si and/or Ge components,

whereas considerable amount of Y component dissolved into the $[Zr_lC_{l+1}]$ layers. Therefore the general formula has to be expanded to $(Zr_{1-x}Y_xC)_l\{(Al_{1-y-z}Si_yGe_z)_4C_3\}_m$, where the maximum x-, y- and z-values were 0.02, 0.07 and 0.02, respectively. After the publication of papers on $Zr_2(Al,Si)_4C_5$ and $Zr_3(Al,Si)_4C_6$, the isomorphous crystal structures were reported in the Hf-Al-C system for $Hf_2Al_4C_5$ and $Hf_3Al_4C_6$. Accordingly, it would be relevant to further expand the solid-solution formula to $(MC)_l(T_4C_3)_m$, where M = Zr, Y and Hf, T = Al, Si and Ge.

In *Chapter 3*, the author has experimentally verified, in the system Zr-Al-Si-C, the formation of $ZrAl_4C_4$, $ZrAl_8C_7$, $Zr(Al,Si)_8C_7$ and $Zr(Al,Si)_4C_4$. In the course of developing new materials, a new compound has been discovered in the Al-Si-O-C system. The author has also characterized the crystal structure as well as the microtexture.

1.3 Structural characterization of oxide-ion-conducting lanthanum silicates from X-ray powder diffraction data

Apatite-type rare-earth (*RE*) silicates, $RE_{9.33}(SiO_4)_6O_2$, are promising materials for gas-sensing devices and electrolyte materials because of the relatively high oxide-ion conductivity at moderate temperatures as well as at low oxygen partial pressures. The lanthanum silicate, $La_{9.33}(SiO_4)_6O_2$, has exhibited much higher conductivity than the other *RE* silicates. The conductivity of the former at 1073 K was ~13.5×10^{-4} Scm^{-1}, which is one order of magnitude larger than that of, for example, neodymium silicate $Nd_{9.33}(SiO_4)_6O_2$ (~2.6×10^{-4} Scm^{-1} at 1073 K). The crystal structures of both lanthanum and neodymium silicates were isotypic at ambient temperature, belonging to the space group $P6_3/m$. These two structural studies are reconciled with each other on the basis of the absence of interstitial oxygen sites in the crystal lattices.

In *Chapter 4*, the author has investigated the crystal structure of lanthanum silicate at high temperature. The structural change with increasing temperature has been compared with that of neodymium silicate with a view to clarifying the structural details that should be peculiar to the highly oxide-ion conducting apatite-type *RE* silicates. The author has also characterized the crystal structures of lanthanum- and oxygen-deficient apatite-type silicates, the general formula of which is represented by $La_{9.33-2x}(SiO_4)_6O_{2-3x}$, $(0 \leq x \leq 0.085)$. The crystal structures of x = 0.06 and 0.085 have been compared with that of x = 0 with a view to clarifying the structural change with increasing x-value.

Chapter 2

Analysis of Unknown and Disordered Structures from Laboratory X-Ray Powder Diffraction Data

2.1 Crystal structure of $Ca_{12}Al_{14}O_{32}Cl_2$ and luminescence properties of $Ca_{12}Al_{14}O_{32}Cl_2$:Eu^{2+}

Abstract

The crystal structure of $Ca_{12}Al_{14}O_{32}Cl_2$ was determined from laboratory X-ray powder diffraction data ($CuK\alpha_1$) using the Rietveld method, with the anisotropic displacement parameters being assigned for all atoms. The crystal structure is cubic (space group $I43d$, $Z = 2$) with lattice dimensions $a =$ 1.200950(5) nm and $V = 1.73211(1)$ nm^3. The reliability indices calculated from the Rietveld method were $R_{wp} = 8.48\%$ ($S = 1.21$), $R_p = 6.05\%$, $R_B = 1.27\%$ and $R_F = 1.01\%$. The validity of the structural model was verified by the three-dimensional electron density distribution, the structural bias of which was reduced as much as possible using the maximum-entropy methods-based pattern fitting (MPF). The reliability indices calculated from the MPF were $R_B = 0.75\%$ and $R_F = 0.56\%$. In the structural model there are one Ca site, two Al sites, two O sites and one Cl site. This compound is isomorphous with $Ca_{12}Al_{10.6}Si_{3.4}O_{32}Cl_{5.4}$. Europium doped sample $Ca_{12}Al_{14}O_{32}Cl_2$:Eu^{2+} was prepared and the photoluminescence properties were presented. The excitation spectrum consisted of two wide bands, which were located at about 268 and 324 nm. The emission spectrum, when excited at 324 nm, resulted in indigo light with a peak at about 442 nm.

Keywords: Calcium-chloro aluminate, Crystal structure, Powder diffraction, Rietveld refinement; Maximum entropy method; Electron density distribution; Luminescence

2.1.1 Introduction

Compounds of the type $Ca_{12}Al_{14}O_{32}X$ have been reported, where $X = 2F^-$ [1], $2Cl^-$ [2], O^{2-} [3-7] and $2OH^-$ [8]. All of these crystal structures are considered to be homeotypic to one another, belonging to the same space group $I43d$. For the compound with $X = 2F^-$, the crystal structure contained positional disordering of Ca sites and occupational disordering of F site [1]. The Ca sites are split into two positions, Ca(1) and Ca(2), with a separation of 0.05 nm. The interatomic distances are shorter for Ca(2)-F (= 0.231 nm) than for Ca(1)-F (= 0.282 nm), hence the F site is only occupied, with the occupancy of 1/3, when the Ca(2) position is also occupied.

The compound with $X = 2Cl^-$ ($Ca_{12}Al_{14}O_{32}Cl_2$) is one of the main constituents of a new type of Portland cement, termed "Eco-cement" [9]. This cement has been recently developed in order to solve the municipal waste problems caused by limited availability of landfill sites. The municipal waste incinerator ash is used as a part of the raw materials. Because the incinerator ash normally contains Cl components in relatively high concentrations, the resulting Eco-cement includes up to 20% of $Ca_{12}Al_{14}O_{32}Cl_2$ instead of $Ca_3Al_2O_6$, which is one of the main constitutes of normal Portland cement. The crystal structure of $Ca_{12}Al_{14}O_{32}Cl_2$ is, in spite of the importance in cement chemistry, still not elucidated so far. On the other hand, the crystal structure of $Ca_{12}[Al_{10.6}Si_{3.4}]O_{32}Cl_{5.4}$ has been determined by Feng *et al.* using single-crystal X-ray diffraction method [10]. In the structural model there are two distinct types of Al/Si sites, Al/Si(1) and Al/Si(2). The significantly shorter Al/Si(1)-O

distances (average = 0.1715 nm) compared with Al/Si(2)-O (average = 0.1762 nm) can be related to the distribution of Si in the Al/Si(1) site [10]. The incorporation of Si into Al sites led to an increase in Cl content to an extent that requires to maintain charge balance. The crystal structure is positionally ordered in that there is one Ca site.

The compound with X = O^{2-} has recently received much attention as a room temperature-stable electride [11]. This material, when activated with Eu^{2+}, showed indigo-light luminescence with a peak wavelength of about 440 nm under UV excitation [12]. The excitation and emission spectra showed the characteristic broadband of the Eu^{2+} ion. Co-doping of Eu^{2+} and Nd^{3+} ions resulted in long afterglow phosphorescence.

Recent advances in modern crystal-structure analyses have enabled us to readily determine three-dimensional distribution of electron densities from X-ray powder diffraction (XRPD) data using the maximum-entropy method (MEM) [13]. However, the Rietveld [14] and MEM analyses are insufficient to derive charge densities because the observed structure factors, F_o(Rietveld), are biased toward the structural models. The subsequent MEM-based pattern fitting (MPF) method [15] reduces the bias as much as possible. Thus, the MEM and MPF analyses are alternately repeated (REMEDY cycle) until the reliability indices no longer decrease. Crystal structures are represented not by structural parameters but by electron densities in MPF.

In the present study, we have prepared the $Ca_{12}Al_{14}O_{32}Cl_2$ powder specimen to refine the crystal structure from XRPD data using the MEM/Rietveld and MPF methods. The crystal has been applied to a new host material for phosphors. We have reported the photoluminescence properties of $Ca_{12}Al_{14}O_{32}Cl_2$:Eu^{2+} to compare with those of $Ca_{12}Al_{14}O_{33}$:Eu^{2+}.

2.1.2 Experimental
(1) Structure refinement

A specimen of $Ca_{12}Al_{14}O_{32}Cl_2$ for structural study was prepared from reagent-grade chemicals $CaCO_3$, Al_2O_3 and $CaCl_2\cdot2H_2O$. Well-mixed chemicals with Ca : Al : Cl = 6 : 7 : 1 in molar ratio were pressed into pellets (12 mm diameter and 3 mm thick), heated at 1273 K for 24 h, followed by quenching in air. Experimental XRPD intensities were collected at 298 K on a PANalytical X'Pert PRO Alpha-1 diffractometer equipped with a high-speed detector (X'Celerator) in the Bragg-Brentano geometry using monochromatized $CuK\alpha_1$ radiation (45 kV, 40 mA). Other experimental conditions were: continuous scan, 2θ range from 17.0032° to 148.4958°, total of 15738 datapoints, and total experimental time of 11.0 h. The divergence slit of 0.25° was employed to collect the quantitative profile intensities over the whole 2θ range.

(2) Luminescence

A phosphor specimen with the formula $Ca_{11.76}Eu^{2+}_{0.24}Al_{14}O_{32}Cl_2$ was prepared by a solid-state reaction. Well-mixed chemicals of $CaCO_3$, Al_2O_3, $CaCl_2\cdot2H_2O$ and Eu_2O_3 were heated at 1423 K for 2 h in reducing atmosphere of N_2 (95 vol.%) and H_2 (5 vol.%), followed by cooling to ambient temperature. The XRPD intensities were collected in a 2θ range from 17.00° to 80.00°. Excitation and emission spectra at 298 K were recorded with a Hitachi F-7000 fluorescence spectrometer.

2.1.3 Results and Discussion
(1) Structure refinement and description

Peak positions of the experimental diffraction pattern were first determined using the

4

computer program PowderX [16]. The 2θ values of 40 observed peak positions were then used as input data to the automatic indexing program TREOR90 [17]. One cubic cell was found with satisfactory figures of merit $M_{20}/F_{20} = 65/69(0.004680,62)$ and $M_{40}/F_{40} = 58/59(0.003824,179)$ [18,19]. The derived unit-cell parameter of $a = 1.200779(9)$ nm could index all the observed reflections in the experimental diffraction pattern. The observed diffraction peaks showed systematic absences $h+k+l \neq 2n$ for hkl and $2h+l \neq 4n$ for hhl reflections, which are consistent with the space group $I\overline{4}3d$.

Initial structural parameters were taken from Feng *et al.* [10] giving the occupancy of Cl site, g(Cl), to be 1/3, corresponding to the chemical formula of $Ca_{12}Al_{14}O_{32}Cl_2$. The structural parameters were refined by the Rietveld method using the program RIETAN-FP [20]. A Legendre polynomial was fitted to background intensities with twelve adjustable parameters. The pseudo-Voigt function [21] was used to fit the experimental peak profiles. Isotropic atomic displacement parameters were initially assigned to all atoms. The refinement resulted in the reliability (R) indices [22] of $R_{wp} = 8.65\%$ ($S = 1.23$), $R_p = 6.19\%$, $R_B = 1.58\%$ and $R_F = 1.03\%$. We subsequently assigned anisotropic atomic displacement (U) parameters to obtain the lower R indices of $R_{wp} = 8.48\%$ ($S = 1.21$), $R_p = 6.05\%$, $R_B = 1.27\%$ and $R_F = 1.01\%$. The number of reflections employed were 372, and the number of refined parameters were 25 for the profile and 24 for the structure. The structure data were standardized using the computer program STRUCTURE TIDY [23], which was implemented in the program RIETAN-FP. The three-dimensional EDD and crystal-structure model were visualized using the software package VESTA [24]. Crystal data are given in Table 2-2, and the final positional and U parameters of atoms are given in Tables 2-3 and 2-4, respectively. A portion of the crystal structure is illustrated in Fig. 2-4.

The MPF method was subsequently applied in order to confirm the validity of the final structural model. After one REMEDY cycle, R_B and R_F decreased to 0.75% and 0.56%, respectively. The significant improvements of these R factors indicate that the crystal structure is represented more adequately with electron densities than with the structural model. The EDD determined by MPF (Fig. 2-5) is explained satisfactorily by the present structural model (Fig. 2-4). We therefore concluded that, as long as the crystal structure is expressed by a structural model, the present structural model would be satisfactory. Observed, calculated, and difference XRPD patterns for the final MPF are plotted in Fig. 2-6.

Selected interatomic distances and bond angles, together with their standard deviations, are listed in Table 2-5. There are two Al sites in the structural model (Fig. 2-4), Al(1) and Al(2), in the ratio of 4 : 3. The Al(1) atom is coordinated to one O(2) atom and three O(1) atoms, with bond lengths ranging from 0.1723 to 0.1762 nm (the mean = 0.175 nm). The Al(2) atom is surrounded by four O(1) atoms (the mean = 0.175 nm). Ionic radii of Al^{3+} in the fourfold coordination [$r(Al^{3+}) = 0.039$ nm and $r(O^{2-}) = 0.138$ nm] predict the interatomic distance of 0.177 nm for Al-O [25]. These values are in good agreement with the mean interatomic distances of Al(1)-O and Al(2)-O. The shared O(1) atoms connect alternating [Al(1)O$_4$] and [Al(2)O$_4$] tetrahedra to form boat-shaped eight-membered rings. The Ca atom is seven-fold coordinated by one Cl, four O(1) and two O(2) atoms. Linear units Ca-Cl-Ca lie on two-fold axis parallel to <100>. This compound has been found to be isomorphous with $Ca_{12}Al_{10.6}Si_{3.4}O_{32}Cl_{5.4}$ [10]. The average Al/Si(1)-O distance of $Ca_{12}Al_{10.6}Si_{3.4}O_{32}Cl_{5.4}$ (<Al/Si(1)-O> = 0.1715 nm) is appreciably shorter than the corresponding Al(1)-O distance of $Ca_{12}Al_{14}O_{32}Cl_2$ (<Al(1)-O> = 0.1752 nm), which should be related to the preferential distribution of Si in the Al/Si(1) site.

(2) Luminescence properties

The XRPD pattern of $Ca_{11.76}Eu^{2+}_{0.24}Al_{14}O_{32}Cl_2$ was very similar to that of $Ca_{12}Al_{14}O_{32}Cl_2$, indicating that the Eu^{2+} ions are homogeneously dispersed in the host crystal to form a single phase.

The emission spectrum, when excited at a wavelength of the highest peak (= 324 nm) of the excitation spectrum, resulted in indigo light with a single peak at 442 nm (Fig. 2-7). The emission spectrum has a broadband character due to $4f$–$5d$ transitions of Eu^{2+} ion. The excitation spectrum shows two wide bands with their peaks at about 268 and 324 nm, which are most probably due to the crystal field splitting of the Eu^{2+} d orbitals. Both excitation and emission spectra were very similar to those of $Ca_{12}Al_{12}O_{33}:Eu^{2+}$ [12]. An attempt was made to synthesize the long afterglow phosphors by co-doping of Eu^{2+} and Nd^{3+} ions into the host $Ca_{12}Al_{14}O_{32}Cl_2$. However, the obtained phosphors $Ca_{12}Al_{14}O_{32}Cl_2:Eu^{2+},Nd^{3+}$ did not show appreciable phosphorescence as compared with $Ca_{12}Al_{12}O_{33}:Eu^{2+},Nd^{3+}$ in a previous study [12].

2.1.4 Conclusion

We determined the crystal structure of $Ca_{12}Al_{14}O_{32}Cl_2$, which has a cubic unit cell with space group $I43d$. The validity of the structural model was verified by the electron density distribution, the structural bias of which was reduced as much as possible using the MPF method. This compound was isomorphous with $Ca_{12}Al_{10.6}Si_{3.4}O_{32}Cl_{5.4}$. The photoluminescence properties of $Ca_{12}Al_{14}O_{32}Cl_2:Eu^{2+}$ were very similar to those of $Ca_{12}Al_{12}O_{33}:Eu^{2+}$.

Acknowledgments

References
[1] P. P. Williams, *Acta Crystallogr.* **B29**, 1550-1551 (1973).
[2] C. Brisi, M. L. Borlera, *Cemento* **80**, 155-164 (1983).
[3] H. Bartl, Neues Jahrb. *Mineral. Monatsh.* **91**, 404-413   (1969).
[4] W. Bussem and A. Eitel, *Z. Kristallogr.* **95**, 175-188 (1936).
[5] J. Jeevaratnam, L. S. Dent Glasser, F. P. Glasser, *Nature*, **194**, 764-765 (1962).
[6] G. Hentschel, Neues Jahrb. *Mineral. Monatsh.* **1**, 22-29 (1964).
[7] H. Boysen, M. Lerch, A. Stys, A. Senyshyn, *Acta Crystallogr.* **B63**, 675-682 (2007).
[8] H. Bartl, Neues Jahrb. *Mineral. Monatsh.* **91**, 397-404 (1969).
[9] S. Yokoyama, *Nyu Seramikkusu* **11**, 59-65 (1998).
[10] Q. Feng, F. P. Glasser, R. A. Howie, E. E. Lachowski, *Acta Crystallogr.* **C44**, 589-592 (1988).
[11] S.-W. Kim, S. Matsuishi, M. Miyakawa, K. Hayashi, M. Hirano, H. Hosono, *J. Mater. Sci. Mater. El.* **18**(Suppl. 1) (2007) S5-S14.
[12] J. Zhang, Z. Zhang, T. Wang, W. Hao, *Mater. Lett.* **57**, 4315-4318 (2003).
[13] M. Takata, E. Nishibori, M. Sakata, *Z. Kristallogr.* **216**, 71-86 (2001).
[14] H. M. Rietveld, *J. Appl. Crystallogr.* **2**, 65-71 (1969).
[15] F. Izumi, S. Kumazawa, T. Ikeda, W. Z. Hu, A. Yamamoto, K. Oikawa, *Mater.Sci.Forum* **378-381**, 59-64 (2001).
[16] C. Dong, *J. Appl. Crystallogr.* **32**, 838 (1999).
[17] P. E. Werner, L. Eriksson, M. Westdahl, *J. Appl. Crystallogr.* **18**, 367-370 (1985).
[18] P. M. de Wolff, *J. Appl. Crystallogr.* **1**, 108-113 (1968).
[19] G. S. Smith, R. L. Snyder, *J. Appl. Crystallogr.* **12**, 60-65 (1979).
[20] F. Izumi, T. Ikeda, *Mater. Sci. Forum* **321-324**, 198-203 (2000).

[21] H. Toraya, *J. Appl. Crystallogr.* **23**, 485-491 (1990).

[22] R. A. Young, in: R. A. Young (Ed.), The Rietveld Method, Oxford University Press, Oxford, U.K., 1993, pp. 1-38.

[23] L. M. Gelato, E. Parthé, *J. Appl. Crystallogr.* **20**, 139-143 (1987).

[24] F. Izumi and K. Momma, *Solid State Phenom.* **130**, 15-20 (2007).

[25] R. D. Shannon, *Acta Crystallogr.* **A32**, 751-767 (1976).

Table 2-2. Crystal data and structure refinement for $Ca_{12}Al_{14}O_{32}Cl_2$.

Chemical composition	$Ca_{12}Al_{14}O_{32}Cl_2$
Space group	$I\bar{4}3d$
a/nm	1.200950(5)
V/nm^3	1.73211(1)
Z	2
D_x/Mgm^{-3}	2.74
Radiation and wavelength/nm	$CuK\alpha_1$, 0.154059
2θ range/°	$17.0032 \leq 2\theta \leq 148.4958$
Number of reflections	372
Number of refined profile parameters	25
Number of refined structural parameters	24
R_{wp} (S), R_p, R_B and R_F (Rietveld)	8.48% (1.21), 6.05%, 1.27%, 1.01%
R_B and R_F (MPF)	0.75%, 0.56%.

Table 2-3. Atomic coordinates and equivalent isotropic displacement parameters for $Ca_{12}Al_{14}O_{32}Cl_2$.

Atom	Position	g	x	y	z	$10^5 \times U$(eq)/nm^2
O(1)	48e	1	0.03457(10)	0.44602(11)	0.14940(11)	10
Ca	24d	1	0.13961(5)	0	1/4	10
O(2)	16c	1	0.18427(11)	x	x	9
Al(1)	16c	1	0.01713(5)	x	x	7
Al(2)	12b	1	7/8	0	1/4	6
Cl	12a	1/3	3/8	0	1/4	23

U(eq) is defined as one-third of the trace of the orthogonalized U_{ij} tensor.

Table 2-4. Anisotropic displacement parameters ($10^5 \times U/nm^2$) for $Ca_{12}Al_{14}O_{32}Cl_2$.

Atom	U_{11}	U_{22}	U_{33}	U_{12}	U_{13}	U_{23}
O(1)	7.7(7)	11.4(9)	10.0(7)	-2.7(6)	-3.3(5)	0.1(6)
Ca	11.4(4)	11.4(3)	6.1(3)	0	0	2.4(3)
O(2)	9.5(6)	U_{11}	U_{11}	-2.3(6)	U_{12}	U_{12}
Al(1)	6.9(2)	U_{11}	U_{11}	-0.1(2)	U_{12}	U_{12}
Al(2)	5.0(7)	6.6(4)	U_{22}	0	0	0
Cl	9(2)	29(1)	U_{22}	0	0	0

The anisotropic displacement factor exponent takes the form $-2\pi^2[h^2a^{*2}*U_{11} + k^2b^{*2}*U_{22} + l^2c^{*2}U_{33} + 2hka^*b^*U_{12} + 2hla^*c^*U_{13} + 2klb^*c^*U_{23}]$.

Table 2-5. Selected interatomic distances (nm) and angles (°).

Ca-O(1)	0.2393(1) × 2	Al(1)-O(2)	0.1723(2)	Al(2)-O(1)	0.1749(1) × 4
Ca-O(2)	0.2410(1) × 2	Al(1)-O(1)	0.1762(1) × 3	O(1)-Al(2)-O(1)	112.68(3) × 4
Ca-O(1)	0.2501(1) × 2	O(1)-Al(1)-O(1)	100.35(7) × 3		103.24(7) × 2
Ca-Cl	0.28269(6)	O(1)-Al(1)-O(2)	117.52(5) × 3		
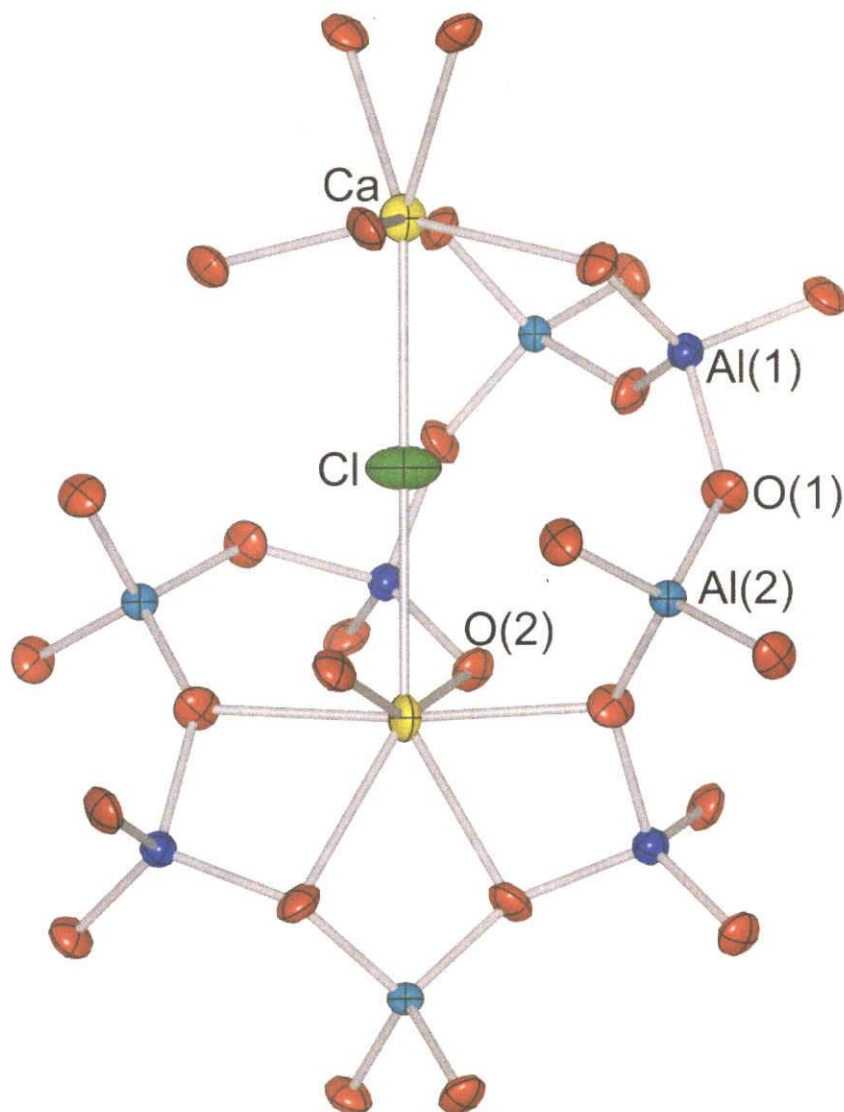
Fig.2-4 A portion of the crystal structure of $Ca_{12}Al_{14}O_{32}Cl_2$ showing eight-membered AlO_4 rings and Ca-Cl-Ca unit. Numbering of atoms corresponds to that given in Table II. Thermal ellipsoids represent 90% of probability.
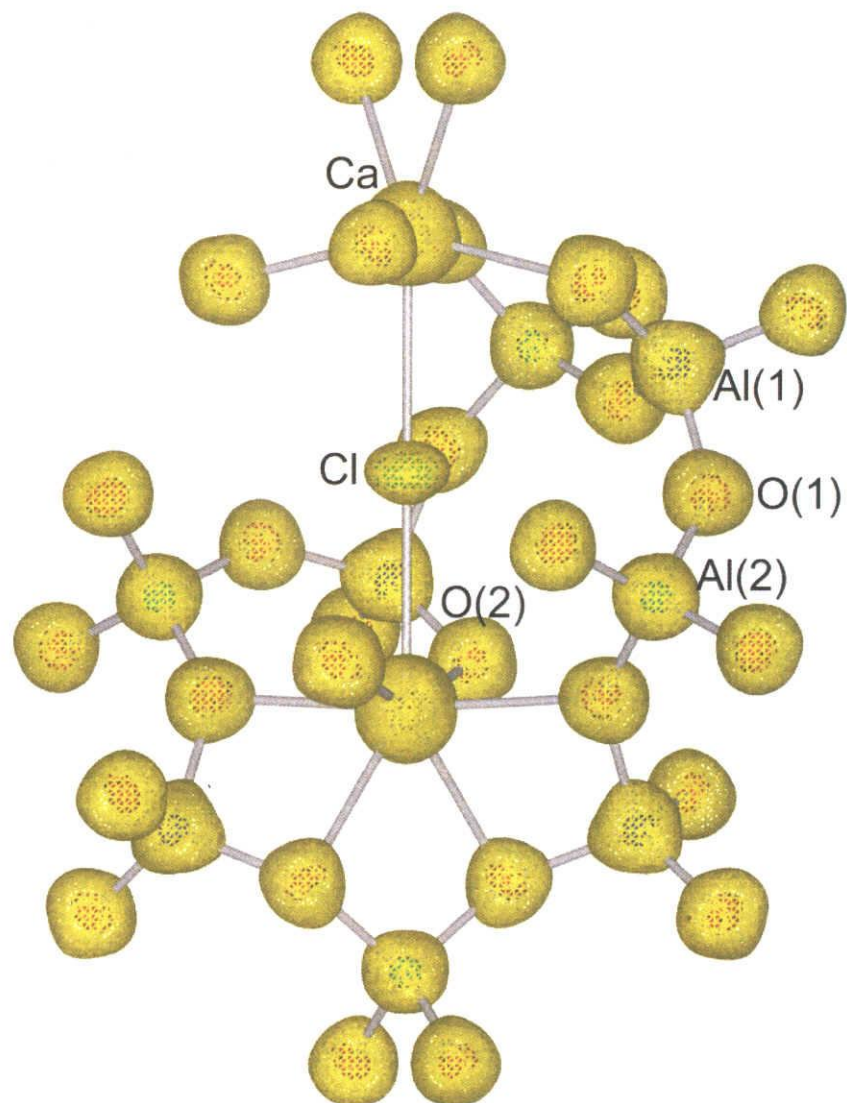
Fig.2-5 Electron-density distribution determined by MPF in the same portion as that of Fig.2-4. Isosurfaces expressed in wireframe style for an equidensity level of 0.002 nm^{-3}.
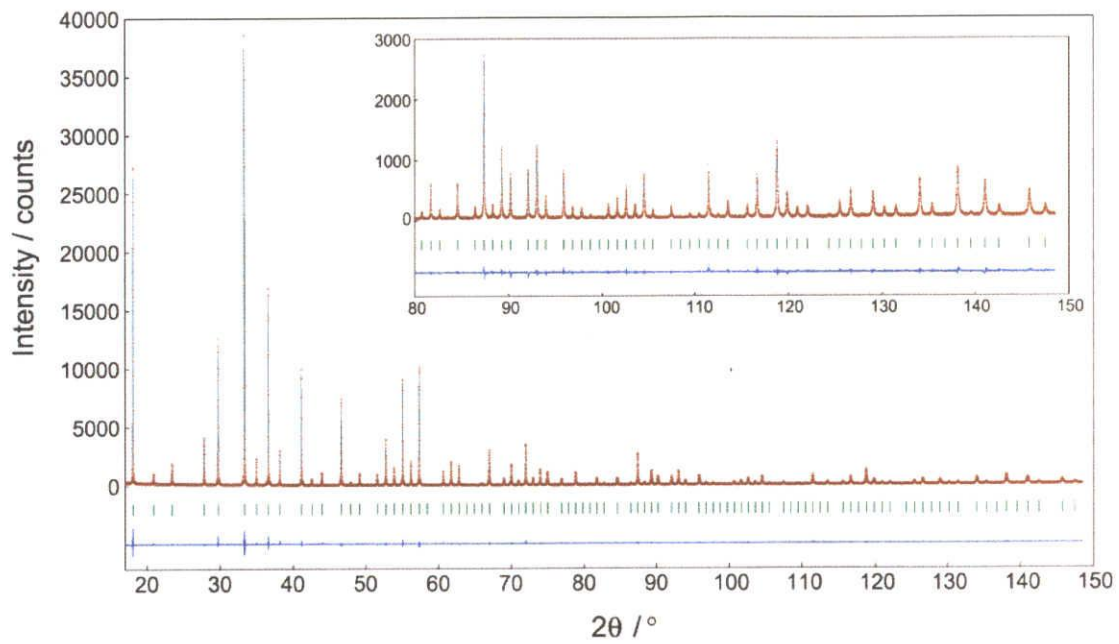
Fig.2-6 Comparison of the experimental diffraction pattern of $Ca_{12}Al_{14}O_{32}Cl_2$ (symbol: +) with the corresponding calculated pattern (upper solid line) determined by MPF method. The difference curve is shown in the lower part of the diagram. Vertical bars indicate the positions of possible Bragg reflections.

Fig.2-7 Emission (E_m) and excitation (E_x) spectra of $Ca_{11.76}Eu^{2+}_{0.24}Al_{14}O_{32}Cl_2$ at 298 K.

2.2. Reinvestigation of crystal structure and structural disorder of $Ba_3MgSi_2O_8$

Abstract

Crystal structure and structural disorder of $Ba_3MgSi_2O_8$ were reinvestigated by laboratory X-ray powder diffraction. The title compound was found to be trigo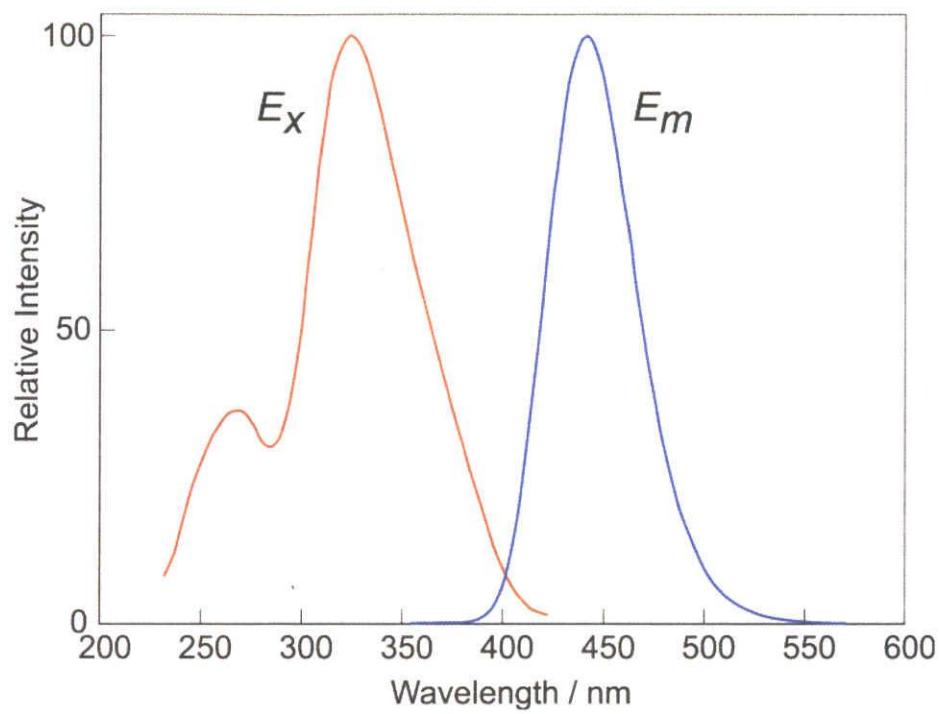nal with space group $P\bar{3}m1$, $Z = 1$, unit-cell dimensions $a = 0.561453(4)$ nm, $c = 0.727629(4)$ nm and $V = 0.198641(2)$ nm^3. The initial structural model used for structure refinement was taken from that of glaserite ($K_3NaS_2O_8$) and modified by a split-atom model. In the split-atom model, one of the two types of Ba sites and SiO_4 tetrahedra were, respectively, positionally and orientationally disordered. The new crystal structure and structural disorder were refined by the Rietveld method. The maximum-entropy methods-based pattern fitting (MPF) method was used to confirm the validity of the split-atom model, in which conventional structure bias caused by assuming intensity partitioning was minimized. The final reliability indices calculated from MPF were $R_{wp} = 6.52\%$, $S = 1.36$, $R_p = 4.84\%$, $R_B = 0.97\%$ and $R_F = 0.52\%$. Details of the disorder structure of $Ba_3MgSi_2O_8$ are shown in the 3D and 2D electron-density distribution maps determined by MPF.

Keywords: barium magnesium silicate, X-ray powder diffraction, Rietveld method, maximum entropy method, electron density distribution, disordered structure

2.2.1 Introduction

Barium magnesium silicate ($Ba_3MgSi_2O_8$) is a promising host material for white light emitting phosphor, because, when co-doped with Eu^{2+} and Mn^{2+}, it efficiently emits the blue and green bands of Eu^{2+} transitions, and the red band of Mn^{2+} transition (Kim et al., 2007; Kim et al., 2005; Umetsu et al., 2008). Recently, Aitasalo et al. (2007) investigated the crystal structure of $Ba_3MgSi_2O_8$ using X-ray powder diffraction (XRPD) method. They proposed three structural models with space groups of $P\bar{3}$, $P321$ and $P\bar{3}m1$. Each model had two crystallographically independent Ba sites, one Mg site and one SiO_4 tetrahedron, one of the O atoms of which is positionally disordered. These three models are essentially isostructural to one another and homeotypic to glaserite, $K_3NaS_2O_8$ (space group $P\bar{3}m1$, lattice dimensions of $a = 0.56801$ nm and $c = 0.7309$ nm (Okada and Ossaka, 1980)). In order to clarify the highly efficient luminescence mechanism and further improve the performance of the phosphor, a more detailed structural study.

Recent advances in the field of crystal-structure analysis from XRPD data have enabled us to investigate complex structures, including positional disordering of atoms and orientational disordering of atomic groups. A combined use of the Rietveld method (Rietveld, 1967), the maximum-entropy method (MEM) (Takata et al., 2001) and the MEM-based pattern fitting (MPF) method (Izumi et al., 2001) has enabled us to disclose new structural details. The Rietveld method and MEM have a drawback in determining the electron density distributions because the observed structure factors, F_o(Rietveld), are biased toward the structural model assuming intensity partitioning. On the other hand, the MPF method can minimize the structural bias. Thus, the MEM and MPF analyses are alternately repeated (REMEDY cycle) until the reliability indices reach minima. Crystal structures can be seen clearly from electron-density distributions determined by MPF.

In the present study, we reinvestigated the structural disorder of $Ba_3MgSi_2O_8$ using the MPF method. The structural model used in the study was originated from that of glaserite and modified-by a split-atom model. Electron-density distributions (EDD) determined by MPF were used to verify the split-atom model.

2.2.2 Experimental

Ba₃MgSi₂O₈ was prepared from stoichiometric amounts of reagent-grade chemicals $BaCO_3$, MgO and SiO_2. Well-mixed chemicals were pressed into pellets (12-mm diameter and 3-mm thick), heated at 1523 K for 6 h, and followed by quenching in air. The sintered material-was finely ground to obtain a powder specimen. A very small amount of $BaMgSiO_4$ crystalline phase was also detected, and it was supposed to be formed by small deviation from stoichiometry in weighing chemicals.

A diffractometer (X'Pert PRO Alpha-1, PANalytical B.V., Almelo, the Netherlands), equipped with an incident-beam Ge(111) Johansson monochromator to obtain $CuK\alpha_1$ radiation and a high-speed detector, was used in the Bragg-Brentano geometry. The X-ray generator was operated at 45 kV and 40 mA. An automatic divergence slit was used to keep a constant illuminated length of 5 mm on the specimen surface. Other experimental conditions were: continuous scan, experimental 2θ range from 10.0051° to 147.9900° (the accuracy in 2θ of ±0.0001°), 8258 total data points and 5.5 h total experimental time. The entire experimental diffraction pattern was employed for the crystal-structure analysis. The structure data were standardized according to rules formulated by Gelato and Parthé (Gelato and Parthé, 1984) using the computer program STRUCTURE TIDY (Gelato and Parthé, 1987). The crystal-structure models and equidensity isosurfaces of EDD were visualized with the computer program VESTA (Momma and Izumi, 2008).

2.2.3 Results and Discussion
(1) Initial structural model

Peak positions of the experimental diffraction pattern were first determined by finding minimums in the second derivatives using the computer program PowderX (Dong, 1999). The 2θ values of 40 observed peak positions were then used as input data to the automatic indexing computer program TREOR90 (Werner et al., 1985). One hexagonal unit cell was found with satisfactory figures of merit: $M40/F40=482/490$ (0.001184, 69) (de Wolff, 1968; Smith and Snyder, 1979). The derived unit-cell parameters of $a = 0.561404(2)$ nm and $c = 0.727546(4)$ nm, which were approximately identical to those of glaserite (Okada and Ossaka, 1980), could index all the observed reflections in the experimental diffraction pattern. The observed diffraction peaks were examined to confirm the presence or absence of reflections. No systematic absence for $hkil$ reflections was found, and it was consistent with the space group $P\bar{3}m1$ of glaserite.

Structural parameters of all atoms were refined by the Rietveld method using the computer program RIETAN-FP (Izumi and Ikeda, 2000). Structural parameters of glaserite with two Ba sites at Wyckoff positions $1a$ (Ba1) and $2d$ (Ba2), one Mg site at $1b$, one Si site at $2d$ and two O sites at $2d$ (O1) and $6i$ (O2) were used as initial structural parameters. The structural model of $BaMgSiO_4$ (space group $P6_3$, $Z = 6$) was included in the refinement as a coexisting second phase (Liu and Barbier, 1993). A Legendre polynomial with twelve adjustable parameters was fitted to background intensities. The split pseudo-Voigt function (Toraya, 1990) was used to fit the peak profiles. The refinement results showed relatively large isotropic displacement parameters (B) for Ba1, O1 and O2 (B(Ba1) = $1.09(2)\times10^{-2}$ nm², B(O1) = $4.6(2)\times 10^{-2}$ nm² and B(O2) = $1.27(5)\times 10^{-2}$ nm²) with reliability (R) indices (Young, 1993) of $R_{wp} = 7.03\%$, $S = 1.47$ and $R_p = 5.27\%$ ($R_B = 2.11\%$ and $R_F = 1.23\%$ for Ba₃MgSi₂O₈). The Si–O1 bond length of 0.156(1) nm obtained by the refinement is significantly shorter than the predicted value of 0.164 nm calculated from the ionic radii of Si^{4+} in the four-fold coordination ($r(Si^{4+}) = 0.026$ nm and $r(O^{2-}) = 0.138$ nm (Shannon, 1976)). These findings prompted us to use a split-atom model for Ba1, O1 and O2.

15

(2) Split-atom model

In the split-atom model, the point symmetry for the Ba1 site was decreased from $\bar{3}m$ (Wyckoff position 1a) to 2 (6g), and the O1 site was displaced from its average 2d position (point symmetry 3m) to three 6i sites (m) around the triad axis by splitting one oxygen atom (O1) into three fractions. Because the number of positions was increased from 2 to 6, the site occupancy g(O1) was reduced to one-third of its initial value (=1/3). Four oxygen atoms were assumed to rigidly bond to a Si atom, forming a solid SiO_4 tetrahedron in the crystal structure. If the Si-O1 bond is tilted from the triad axis, one of the three basal oxygen atoms O2 will be lifted up and the remaining two O2 atoms will remain almost at the same positions. If the SiO_4 tetrahedra are equally tilted into three directions, one third of O2 atom will be lifted up and the remaining two thirds will remain almost at the same positions. Therefore, the O2 atom at 6i was split into two independent crystallographic sites (O2A and O2B) at two 6i sites. The site occupancies of O2A and O2B were refined under the constraint that the total number of O atoms on these sites were unchanged; g(O2A) + g(O2B) = 1. Because the g and corresponding B parameters were strongly correlated, they were refined alternately in least-squares cycles. The g(O2A) and g(O2B) values converged to 0.67 ($\approx$ 2/3) and 0.33 ($\approx$ 1/3), respectively. These refined occupancy parameter values were well in accordance with the orientationally disordered model of SiO_4 tetrahedra, which are related by the rotation triad axis passing through the Si atom. Accordingly, we have fixed these occupancies at g(O2A) =2/3 and g(O2B) = 1/3 in the subsequent least-squares cycles. The Rietveld refinement with this split-atom model resulted in the lower reliability indices of R_{wp} = 6.62%, S = 1.39, R_p = 4.89%, R_B = 1.83% and R_F = 1.05% as compared with the former Rietveld analysis. The crystal data are given in Table 2-6, and the final positional and B parameters of atoms are given in Table 2-7. Quantitative X-ray analysis with correction for microabsorption according to Brindley's procedure (Brindley, 1949) was implemented in the program RIETAN-FP. The phase composition was found to be 98.8 mass% $Ba_3MgSi_2O_8$ and 1.2 mass% $BaMgSiO_4$.

Figure 2-8 shows the refined structural model of $Ba_3MgSi_2O_8$. The Ba1 site is split into six positions, each of which is on the rotation diad axes parallel to <100> or <110>. The O1 site is divided into three sites around the triad axis passing through the Si site, and hence the Si-O1 directions make angles of 11.7(2)° with this axis (Fig. 2-9). This value is comparable to the O2A-Si-O2B angles of 7.4(9)°. In the refined crystal structure (Table 2-7), the O2B atom having the occupancy of 1/3 was observed to lift upward caused by the tilt of the Si-O1 bond. Accordingly, the disordered SiO_4 tetrahedra can be regarded as a statistical average of the three different orientational configurations. In Table 2-8, we reported only Si-O bonds and O-Si-O angles of SiO_4 tetrahedra belonging to one of the three orientations, excluding the bonds and angles between atoms of different orientation states. The average Si-O bond length agrees with the interatomic distance of 0.164 nm calculated from the ionic radii of Si^{4+} and O^{2-} in the four-fold coordination. The average value of the O-Si-O angles are 109.4°. These interatomic distances and bond angles are in good agreement with those found in other silicates (Baur, 1971).

The MPF method was subsequently used to confirm the validity of the split-atom model. After two REMEDY cycles, R_{wp}, S, R_p, R_B and R_F decreased to 6.52%, 1.36, 4.84%, 0.97% and 0.52%, respectively. Subtle EDD changes as revealed by MPF significantly improve the R_B and R_F indices. The decreases in R indices demonstrate that the present disordered structure can be seen more clearly from electron-density distributions instead of from the conventional structural parameters reported in Table 2-7. Observed, calculated, and difference XRPD patterns for the final MPF are plotted in Fig. 2-10. The EDD at the Ba1, O1, O2A and O2B sites shows broadening, the equidensity isosurfaces of which are in reasonably good agreement with the atom arrangements (Fig. 2-11). The two-dimensional

16

map on (001) at the height of O1 sites (Fig. 2-12) clearly demonstrates that the equidensity isosurface is related by the rotation triad axes.

We also tried to refine the disordered structural models with both space groups $P\bar{3}$ (centrosymmetric) and $P321$ (non-centrosymmetric), and found that the standard deviations of O-atom coordinates (general position $6g$ for both $P\bar{3}$ and $P321$) were unusually large. Therefore, the most conceivable space group for $Ba_3MgSi_2O_8$ is $P\bar{3}m1$. The highly efficient luminescence properties of $Ba_3MgSi_2O_8{:}Eu^{2+},Mn^{2+}$ may be related to the structural disorder of host material.

2.2.4 Conclusion

The highly disordered crystal structure of $Ba_3MgSi_2O_8$ was successfully determined from XRPD data. The structure was expressed by the split-atom model, in which one of the two types of Ba atoms and SiO_4 tetrahedra were, respectively, positionally and orientationally disordered. EDD was successfully determined by the MPF method. The results obtained in this study show that disordered structure of $Ba_3MgSi_2O_8$ can be best illustrated by 3D and 2D EDD maps given in Figs. 2-11 and 2-12, which is superior to that derived directly from conventional structure parameters listed in Table 2-7.

References

[1] Aitasalo, T., Hietikko, A., Hölsä, J., Lastusaari, M., Niittykoski, J., and Piispanen, T., *Z. Kristallogr. Suppl.* **26**, 461-466 (2007)..

[2] Baur, W. H, *Am. Mineral.* **56**, 1573–1599 (1971).

[3] Brindley, G. W., *Bulletin de la Societe Chimique de France* D59-63 (1949).

[4] Dong, C., *J. Appl. Crystallogr.* **32**, 838 (1999).

[5] Gelato L. M., and Parthé, E., *J. Appl. Crystallogr.* **20**, 139-143 (1987).

[6] Izumi, F., and Ikeda, T., *Mater. Sci. Forum* **321-324**, 198-203 (2000).

[7] Izumi, F., Kumazawa, S., Ikeda, T., Hu, W.-Z., Yamamoto, A., and Oikawa, K., *Mater. Sci. Forum* **378-381**, 59-64 (2001).

[8] Kim, J. S., Kwon, A. K., Park, Y. H., Choi, J. C., Park, H. L., and Kim, G. C., *J. Lumin.* **122-123**, 583-586 (2007).

[9] Kim, J. S., Lim, K. T., Jeong, Y. S., Jeon, P. E., Choi, J. C., and Park, H. L., *Solid State Commun.* **135**, 21-24 (2005).

[10] Liu, B., and Barbier, J., *J. Solid State Chem.* **102**, 115-125 (1993).

[11] Momma, K., and Izumi, F., *J. Appl. Crystallogr.* **41**, 653-658 (2008).

[12] Okada, K., and Ossaka, J., *Acta Crystallogr.* **B36**, 919-921 (1980).

[13] Parthé, E., and Gelato, L. M., **A10**, 169-183 (1984).

[14] Rietveld, H. M., *Acta Crystallogr.* **22**, 151-152 (1967).

[15] Shannon, R. D., *Acta Crystallogr.* **A32**, 751-767 (1976).

[16] Smith, G. S., and Snyder, R. L., *J. Appl. Crystallogr.* **12**, 60-65 (1979).

[17] Takata, M., Nishibori, E., and Sakata, M., *Z. Kristallogr.* **216**, 71-86 (2001).

[18] Toraya, H., *J. Appl. Crystallogr.* **23**, 485-491 (1990).

[19] Umetsu, Y., Okamoto, S., and Yamamoto, H., *J. Electrochem. Soc.* **155**, 193-197 (2008).

[20] Werner, P. E., Eriksson, L., and Westdahl, M., *J. Appl. Crystallogr.* **18**, 367-370 (1985).

[21] de Wolff, P. M., *J. Appl. Crystallogr.* **1**, 108-113 (1968).

[22] Young, R. A., *The Rietveld Method* (Oxford University Press, Oxford, U.K.), Edited by R. A. Young, pp. 1-38 (1993).

Table 2-6. Crystal data for $Ba_3MgSi_2O_8$.

Chemical composition	$Ba_3MgSi_2O_8$
Space group	$P\bar{3}m1$
a / nm	0.561453(4)
c / nm	0.727629(4)
V / nm^3	0.198641(2)
Z	1
D_x / Mgm^{-3}	5.19

Table 2-7. Structural parameters for $Ba_3MgSi_2O_8$.

Site	Wyckoff position	g	x	y	z	$100 \times B$ / nm^2
Ba1	$6g$	1/6	0.0219(6)	0	0	0.70(3)
Ba2	$2d$	1	1/3	2/3	0.6781(1)	0.70(1)
Mg	$1b$	1	0	0	1/2	0.89(8)
Si	$2d$	1	1/3	2/3	0.2402(4)	0.64(3)
O1	$6i$	1/3	0.367(1)	-x	0.020(1)	1.33(26)
O2A	$6i$	2/3	0.179(1)	-x	0.330(1)	0.86(10)
O2B	$6i$	1/3	0.171(2)	-x	0.302(2)	0.86

Table 2-8. Si-O bond lengths (nm) and O-Si-O angles (degrees) in $Ba_3MgSi_2O_8$.

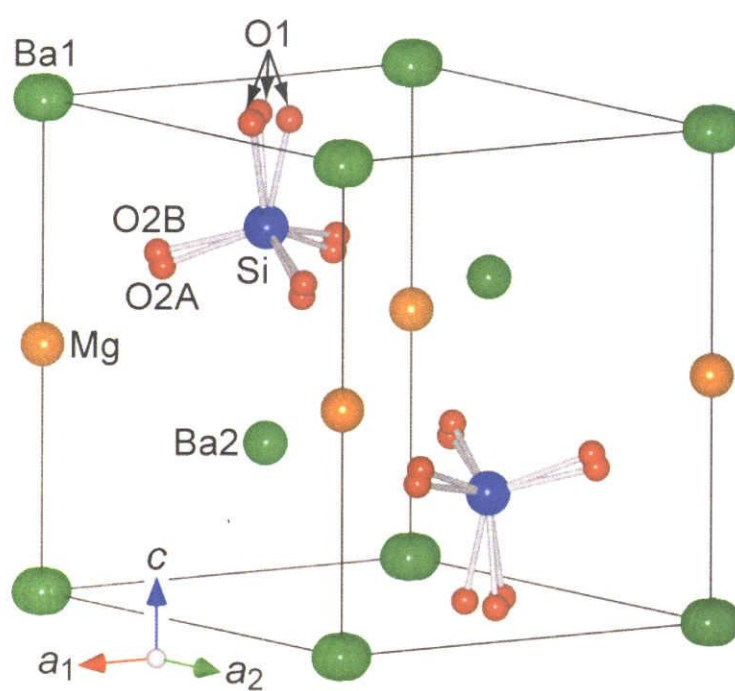|	
Si-O1	0.1637(8)
Si-O2A	0.164(1) × 2
Si-O2B	0.164(2)
<Si-O>	0.164
O1-Si-O2A	107.2(4) × 2
O1-Si-O2B	117.7(7)
O2A-Si-O2A	105.3(4)
O2A-Si-O2B	109.4(2) × 2
<O-Si-O>	109.4

Figure Captions
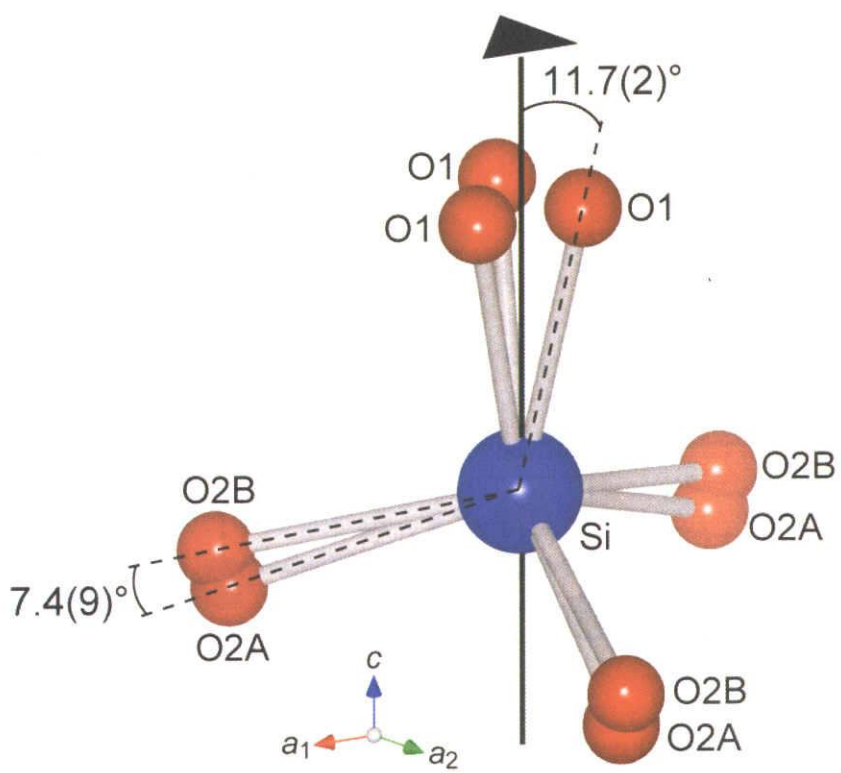

Fig. 2-8. Crystal structure of $Ba_3MgSi_2O_8$.

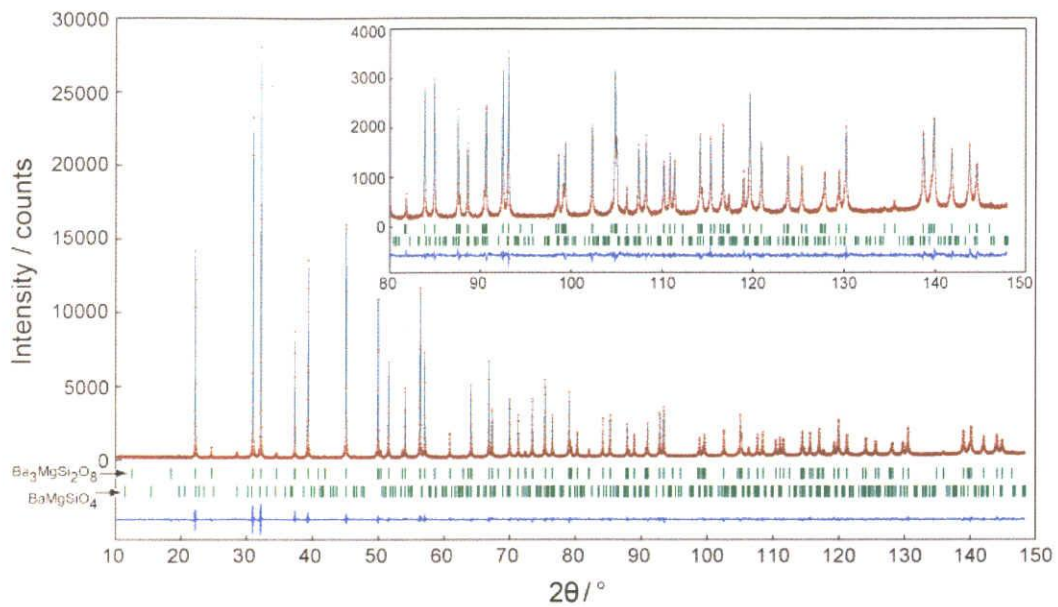Fig. 2-9. Coordination sphere of O atoms around a Si atom with the split-atom model.

Fig. 2-10. Comparison of the observed diffraction pattern of $Ba_3MgSi_2O_8$ and $BaMgSiO_4$ (symbol: +) with the corresponding calculated pattern (upper solid line). The difference curve is shown in the lower part of the diagram. Vertical bars indicate the positions of possible Bragg reflections.
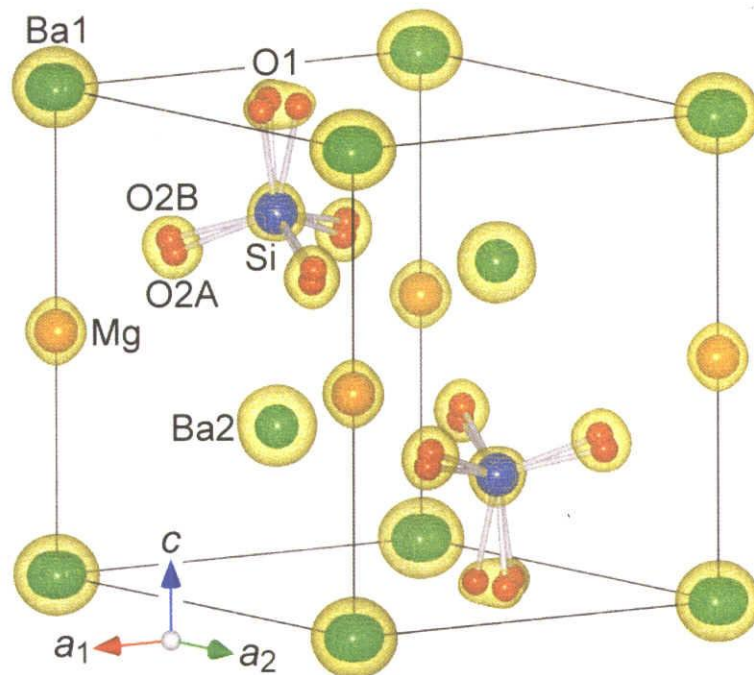
Fig. 2-11. Three-dimensional electron-density distributions determined by MPF with the split-atom model. Isosurfaces expressed in wireframe style for an equidensity level of 0.005 nm^{-3}.
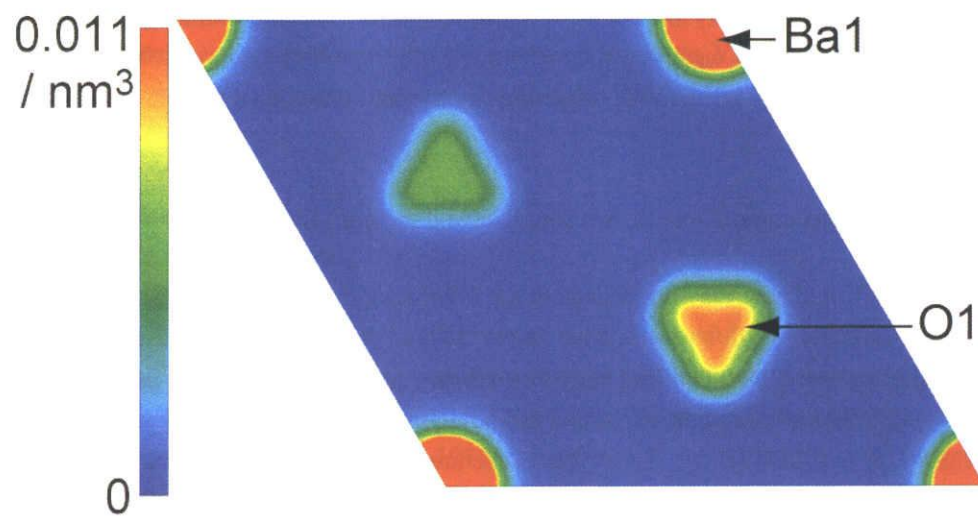
Fig. 2-12. Two-dimensional electron-density distribution map parallel to (001) at the height of the O1 sites, $z = 0.002$.

Chapter 3

Syntheses, crystal structures and thermoelectric properties of new layered carbides

3.1 Synthesis and crystal structure of a new layered carbide $ZrAl_4C_4$

Abstract

A new ternary layered carbide, $ZrAl_4C_4$, has been synthesized and characterized by X-ray powder diffraction. The crystal structure was successfully determined using direct methods, and further refined by the Rietveld method. The crystal is trigonal (space group $P3m1$, $Z = 2$) with lattice dimensions $a = 0.332471(3)$ nm, $c = 2.19717(2)$ nm and $V = 0.210330(3)$ nm^3. The final reliability indices calculated from the Rietveld refinement were $R_{wp} = 6.56\%$ ($S = 1.58$), $R_p = 4.92\%$, $R_B = 1.90\%$ and $R_F = 0.98\%$. The compound shows an intergrowth structure with NaCl-type [Zr_2C_3] thin slabs separated by Al_4C_3-type [Al_8C_7] layers.

Keywords: Crystal structure; X-ray diffraction; Rietveld method; Carbides

3.1.1 Introduction

In the system Zr-Al-C, there are two ternary carbides confirmed so far; $Zr_2Al_3C_4$ and $Zr_3Al_3C_5$ [1, 2]. These compounds form a homologous series, the general formula of which is $(ZrC)_mAl_3C_2$ ($m = 2$ and 3) [2]. The crystal structures, belonging to the same space group $P6_3mc$ (non-centrosymmetric), can be regarded as intergrowth structures where the Al_4C_3-type [Al_3C_3] layers are the same, while the NaCl-type [Zr_mC_{m+1}] layers increase in thickness with increasing m value. These two types of layers shear the carbon-atom network at their boundaries; the C-C distances are ~0.335 nm for both carbides with $m = 2$ and 3. On the other hand, the C-C distance of ZrC crystal is 0.330 nm (= $a(ZrC)/\sqrt{2}$) and that of Al_4C_3 is 0.334 nm (= $a(Al_4C_3)$), where $a(ZrC)$ and $a(Al_4C_3)$ represent the a-axis lengths of the ZrC and Al_4C_3 crystals, respectively. These distances are close to each other, and also to those of the carbon-atom networks in $(ZrC)_mAl_3C_2$. Fukuda et al [2]. have therefore concluded that the closeness of the C-C distances between the ZrC and Al_4C_3 crystals, being expressed by the equation $a(ZrC)/\sqrt{2} \approx a(Al_4C_3)$, is the principal reason for the formation of these layered carbides.

From analogy with the existence of the homologous carbides $(ZrC)_mAl_3C_2$, we have expected the formation of new ternary carbides for the reaction products ZrC and Al_4C_3. In the present study, we have experimentally confirmed the existence of a new layered carbide in the Zr-Al-C system. The crystal structure has been determined from XRPD data using direct methods, and described in relation to those of ZrC, Al_4C_3 and $(ZrC)_mAl_3C_2$. The intergrowth structure was composed of the NaCl-type [Zr_2C_3] slabs separated by the Al_4C_3-type [Al_8C_7] layers.

3.1.2 Experimental Procedure

The new quaternary carbide was initially recognized as unidentifiable diffraction lines in the XRPD patterns of the reacted ZrC-Al_4C_3 mixtures. We obtained the powder specimen that was mainly consisting of the new carbide together with a very small amount of $Zr_2Al_3C_4$ by the following procedure. The reagent-grade chemicals of ZrC (99.9%, KCL Co., Ltd, Saitama, Japan) and Al_4C_3

(KCL, 99. 9%) were mixed in molar ratios of ZrC : Al_4C_3 = 1 : 1, which is equivalent to Zr : Al : C = 1 : 4 : 4. The well-mixed chemicals were pressed into compacts (10 mm × 10 mm × 5 mm), heated at 2273 K for 1 h in inert gas atmosphere of Ar, followed by cooling to ambient temperature by cutting furnace power. The reaction product was a slightly sintered polycrystalline material. It was finely ground to obtain powder specimen. The density (D_o) was measured by the pyknometric method and found to be 3.78 Mgm^{-3}.

The XRPD intensities of the powder specimen were collected on a diffractometer (X'Pert PRO Alpha-1, PANalytical B.V., Almelo, the Netherlands) equipped with a high speed detector in Bragg-Brentano geometry using monochromatized $CuK\alpha_1$ radiation (45kV, 40mA) in a 2θ range from 2.0094° to 148.9014° (the accuracy in 2θ of ±0.0001°). The automatic divergence slit was employed to collect the quantitative profile intensities over the 2θ range of $2\theta \geq 5°$. Other experimental conditions were: continuous scan, total of 8791 datapoints and total experimental time of 16.1 h. The crystal-structure models were visualized with the computer program VESTA [3]. The structure data were standardized using the computer program STRUCTURE TIDY [4].

3.1.3 Results and Discussion
(1) Crystal structure determination

The XRPD pattern in Fig. 3-1 showed the presence of very weak diffraction intensities peculiar to $Zr_2Al_3C_4$. All of the other diffraction peaks were successfully indexed with a hexagonal unit cell. The unit-cell parameters and integrated intensities of the unknown phase were refined by the Le Bail method using the computer program RIETAN-FP [5]. The unit-cell dimensions determined by the method were a = 0.332473(3) nm, c = 2.19706(2) nm and V = 0.210323(6) nm^3, which will be further refined by the subsequent Rietveld method. The integrated intensities were examined to confirm the presence or absence of reflections. There were no systematic absences, implying that the possible space groups are $P3$, $P\bar{3}$, $P321$, $P3m1$, $P\bar{3}m1$, $P312$, $P31m$, $P\bar{3}1m$, $P6$, $P\bar{6}$, $P6/m$, $P622$, $P6mm$, $P\bar{6}2m$, $P\bar{6}m2$ and $P6/mmm$.

In general, the number of formula units in the unit cell (Z) is determined from the unit-cell volume V (nm^3), true density D_t (Mgm^{-3}) and molecular weight M (g) as follows:

$$Z = VD_t/(M \times 1.660 \times 10^{-3}).\qquad(1)$$

Because the most probable molar ratios of Zr : Al : C are 1 : 4 : 4 for the unknown phase, the chemical formula would be $ZrAl_4C_3$ (M = 247.19 g). Substituting 247.19 g, 0.21032 nm^3 and 3.78 $Mg \cdot m^{-3}$ (= D_o) for, respectively, M-, V- and D_t-values in equation (1) yields 1.94 for an approximate value of Z. Thus, the Z-value must be equal to 2, which indicates that the unit cell content is [2Zr 8Al 8C].

All of the possible space groups were tested using the EXPO2004 package [6] for crystal structure determination. Although the profile intensities in the range $2\theta < 5°$ were not quantitatively accurate, the strong reflection at $2\theta \approx 4.00°$ was essential for deriving the proper structural model. A promising structural model with the reliability index R_F [7] of 7.20% was successfully obtained for the space group $P3m1$ (non-centrosymmetric). There were 18 independent atoms in the unit cell; two Zr atoms, eight Al atoms and eight C atoms.

The structural parameters as well as the unit-cell dimensions were refined by the Rietveld method using the computer program RIETAN-FP [5] in a 2θ range of 5.00° to 148.90° (Fig. 3-1). A Legendre polynomial was fitted to background intensities with twelve adjustable parameters. The pseudo-Voigt function [8] was used to fit the peak profile. The isotropic atomic displacement

parameters (B) of the C sites were constrained to have the same value. The preferred orientation parameter of March-Dollase function [9], r, was refined to be $r = 0.8928(8)$ with the preferred-orientation vector [001], suggesting that the crystal was fractured along the cleavage planes parallel to (001). Reliability indices[7] for a final result were $R_{wp} = 6.56\%$ ($S = 1.58$), $R_p = 4.92\%$, $R_B = 1.90\%$ and $R_F = 0.98\%$. Crystal data are given in Table 3-1, and the final atomic positional and B parameters are given in Table 3-2. The selected interatomic distances, together with their standard deviations, are given in Table 3-3. Quantitative X-ray analysis with correction for microabsorption according to Brindley's procedure [10] was implemented in the program RIETAN-FP. The phase composition of the sample was found to be 96.9 mass% $ZrAl_4C_4$ and 3.1 mass% $Zr_2Al_3C_4$.

We also carried out the refinement in the space group $P3m1$ (centrosymmetric). In the structural model, there are 10 independent atoms in the unit cell; one Zr atom (Wyckoff position $2d$), four Al atoms (Al(1) and Al(2) on $2c$, Al(3) and Al(4) on $2d$) and five C atoms (C(1) on $1a$, C(2) on $1b$, C(3) on $2c$, and C(4) and C(5) on $2d$). The refinement resulted in a large B parameter (= $1.42(3) \times 10^{-2}$ nm^2) for the Al(4) position (1/3, 2/3, 0.23502(6)) with the less satisfactory reliability indices of $R_{wp} = 6.74\%$ ($S = 1.62$), $R_p = 5.10\%$, $R_B = 2.16\%$ and $R_F = 1.08\%$. Since such a large B parameter was considered unrealistic, we split this atom into two fractions as (1/3, 2/3, 0.2327(5)) and (1/3, 2/3, 0.2379(5)). This refinement resulted in the lower reliability indices of $R_{wp} = 6.70\%$ ($S = 1.61$), $R_p = 5.05\%$, $R_B = 2.09\%$ and $R_F = 1.05\%$. This structure is describable in the lower symmetry space group $P3m1$, where the Al atoms of the split positions fully occupy the positions $1c$ and $1b$, assuming that the crystal is composed of two twin domains related by the inversion symmetry. Thus we concluded that the structural model with the space group $P3m1$ would be adequate for the new carbide.

(2) Structure description

The crystal structure of $ZrAl_4C_4$ can be regarded as intergrowth structure, which consists of the [Zr_2C_3] layers with thickness of ~0.557 nm separated by the [Al_8C_7] layers of ~1.640 nm thickness (Fig. 3-2). The mean interatomic distances in $ZrAl_4C_4$ compare well with those of ZrC, Al_4C_3, $Zr_2Al_3C_4$ and $Zr_3Al_3C_5$. The Zr atoms are octahedrally coordinated by C atoms with the mean Zr-C distance of 0.237 nm (Table 3-3), which is comparable to those of the [ZrC_6] polyhedra in NaCl-type ZrC (0.235 nm), $Zr_2Al_3C_4$ (0.241 nm) [2] and $Zr_3Al_3C_5$ (0.239 nm) [1]. The Zr-Zr distance of 0.3325 nm in $ZrAl_4C_4$ is comparable to those of ZrC (0.332 nm), $Zr_2Al_3C_4$ (0.335 nm) and $Zr_3Al_3C_4$ (0.331 nm). The Al atoms are tetrahedrally coordinated with the mean distances of 0.199 nm for Al(1)-C, 0.209 nm for Al(2)-C, 0.209 nm for Al(3)-C, 0.206 nm for Al(4)-C, 0.199 nm for Al(5)-C, 0.204 nm for Al(6)-C, 0.205 nm for Al(7)-C and 0.205 nm for Al(8)-C. Accordingly, the Al-C distances are comparable to the Al-C distances of the [AlC_4] tetrahedra in Al_4C_3, ranging from 0.199 to 0.209 nm (the mean = 0.205 nm) [11]. In Fig. 3-3, the atomic configurations are shown for $ZrAl_4C_4$ and Al_4C_3. The [Al_8C_7] layer of the former is clearly demonstrated to be structurally comparable to the latter, with the atom arrangement in the [Zr_2C_3] layer being very similar to that of the NaCl structure.

3.1.4. Conclusion

In the Zr-Al-C system, we have successfully synthesized the new carbide $ZrAl_4C_4$. The crystal structure was determined from XRPD data and described in relation to those of ZrC, Al_4C_3, $Zr_2Al_3C_4$ and $Zr_3Al_3C_5$. The crystal structure was considered to be composed of the NaCl-type [Zr_2C_3] slabs separated by the Al_4C_3-type [Al_8C_7] layers.

References

[1] Th. M. Gesing and W. Jeitschko, *J. Solid State Chem.,* **140,** 396-401 (1998).

[2] K. Fukuda, S. Mori, and S. Hashimoto, *J. Am. Ceram. Soc.,* **88,** 3528-30 (2005).

[3] F. Izumi and K. Momma, **130,** 15-20 (2007).

[4] L. M. Gelato and E. Parthé, *J. Appl. Crystallogr.,* **20,** 139-43 (1987).

[5] F. Izumi and T. Ikeda, "A Rietveld-Analysis Program RIETAN-98 and Its Applications to Zeolites," *Mater. Sci. Forum,* **321-324,** 198-203 (2000).

[6] A. Altomare, M. C. Burla, M. Camalli, B. Carrozzini, G. L. Cascarano, C. Giacovazzo, A. Guagliardi, A. G. G. Moliterni, G. Polidori, and R. Rizzi, *J. Appl. Crystallogr.,* **32,** 339-40 (1999).

[7] R. A. Young, in: R. A. Young (Ed.), *The Rietveld Method,* Oxford University Press, Oxford, U.K., 1993, pp. 1-38.

[8] H. Toraya, *J. Appl. Crystallogr.,* **23,** 485-91 (1990).

[9] W. A. Dollase, *J. Appl. Crystallogr.,* **19,** 267-72 (1986).

[10] G. W. Brindley, *Bulletin de la Societe Chimique de France,* D59-63 (1949).

[11] Th. M. Gesing and W. Jeitschko, *Z. Naturforsch.,* **50b,** 196-200 (1995).

Table 3-1. Crystal data for $ZrAl_4C_4$

Chemical composition	$ZrAl_4C_4$
Space group	$P3m1$
a/nm	0.332471(3)
c/nm	2.19717(2)
V/nm^3	0.210330(3)
Z	2
D_x/Mgm^{-3}	3.90

Table 3-2. Structural parameters for $ZrAl_4C_4$

Site	Wyckoff position	x	y	z	$100 \times B$/nm^2
Zr(1)	1c	2/3	1/3	0.6823(6)	0.43(5)
Zr(2)	1b	1/3	2/3	0.8027(6)	0.46(5)
Al(1)	1c	2/3	1/3	0.0138(6)	0.70(9)
Al(2)	1c	2/3	1/3	0.1988(7)	0.78(23)
Al(3)	1b	1/3	2/3	0.2882(7)	0.74(24)
Al(4)	1b	1/3	2/3	0.4838(6)	0.79(9)
Al(5)	1a	0	0	0.0953(6)	0.77(23)
Al(6)	1a	0	0	0.3935(6)	0.73(24)
Al(7)	1a	0	0	0.5814(8)	0.73(16)
Al(8)	1a	0	0	0.9099(8)	0.69(15)
C(1)	1c	2/3	1/3	0.1114(13)	0.30(4)
C(2)	1c	2/3	1/3	0.8737(7)	0.30
C(3)	1b	1/3	2/3	0.3731(13)	0.30
C(4)	1b	1/3	2/3	0.6203(6)	0.30
C(5)*	1a	0	0	0	0.30
C(6)	1a	0	0	0.2432(18)	0.30
C(7)	1a	0	0	0.4954(5)	0.30
C(8)	1a	0	0	0.7404(11)	0.30

$^*z$ of C(5) atom is fixed.

28

Table 3-3. Interatomic distances (nm) in $ZrAl_4C_4$[*]

Zr(1)-C(8)	0.231(1) × 3
Zr(1)-C(4)	0.235(2) × 3
Zr(1)-Al(7)	0.293(2) × 3
Zr(1)-Zr(2)	0.327(1) × 3
Zr(2)-C(8)	0.236(2) × 3
Zr(2)-C(2)	0.247(1) × 3
Zr(2)-Al(8)	0.304(2) × 3
Al(1)-C(5)	0.1943(2) × 3
Al(1)-C(1)	0.214(3)
Al(1)-Al(5)	0.262(1) × 3
Al(1)-Al(8)	0.298(2) × 3
Al(2)-C(1)	0.192(3)
Al(2)-C(6)	0.215(2) × 3
Al(2)-Al(3)	0.275(2) × 3
Al(2)-Al(5)	0.298(2) × 3
Al(3)-C(3)	0.187(3)
Al(3)-C(6)	0.216(2) × 3
Al(3)-Al(6)	0.301(2) × 3
Al(4)-C(7)	0.1936(2) × 3
Al(4)-C(3)	0.243(3)
Al(4)-Al(6)	0.276(1) × 3
Al(4)-Al(7)	0.288(2) × 3
Al(5)-C(1)	0.1952(6) × 3
Al(5)-C(5)	0.209(1)
Al(6)-C(3)	0.1971(7) × 3
Al(6)-C(7)	0.224(2)
Al(7)-C(7)	0.189(2)
Al(7)-C(4)	0.2101(9) × 3
Al(8)-C(5)	0.198(2)
Al(8)-C(2)	0.2078(9) × 3

[*]All distances shorter than 0.33 nm (metal-metal) and 0.25 nm (metal-carbon) are given.
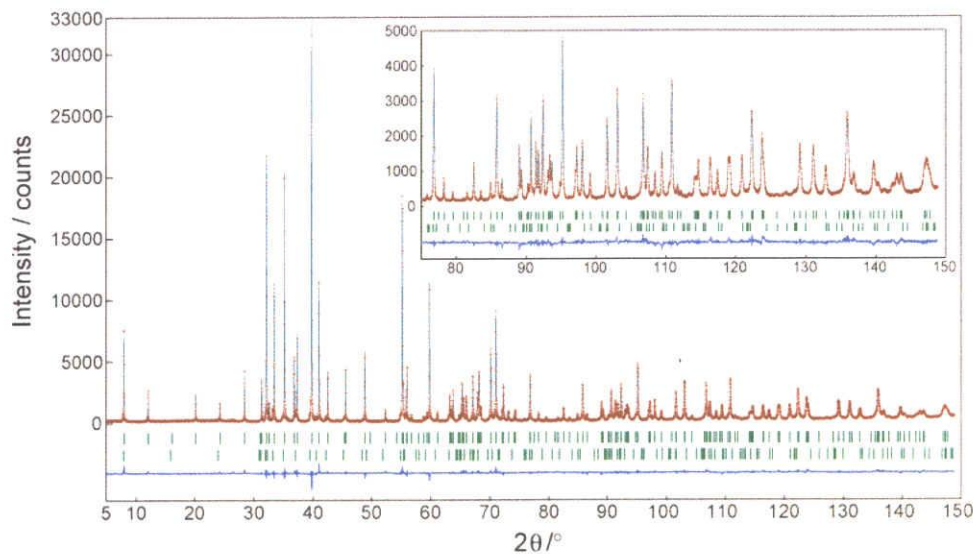
Fig.3-1. Comparison of observed diffraction pattern of ZrAl$_4$C$_4$ and Zr$_2$Al$_3$C$_4$ (symbol: +) with the corresponding calculated pattern (upper solid line). The difference curve is shown in the lower part of the diagram. Upper vertical bars indicate the positions of possible Bragg reflections for ZrAl$_4$C$_4$ and those of the lower for Zr$_2$Al$_3$C$_4$.
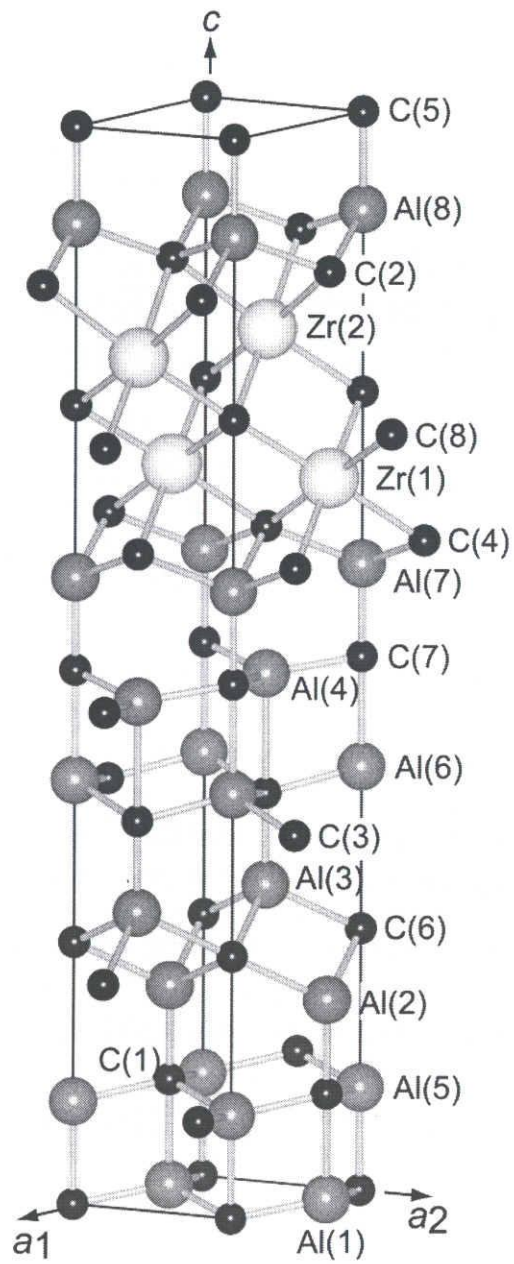
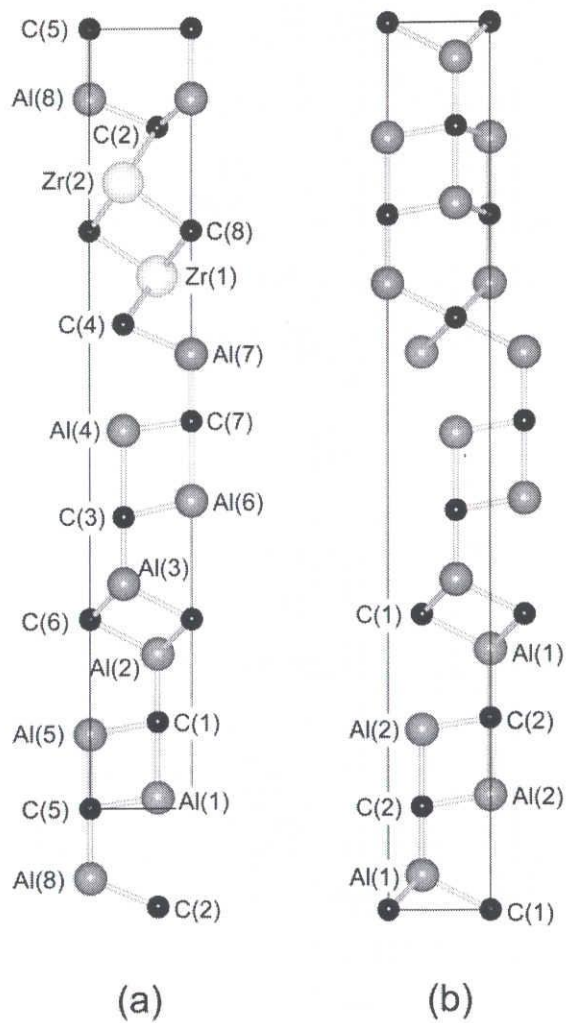Fig.3-2. Crystal structure of $ZrAl_4C_4$.

Fig.3-3. Atomic configurations in (a) $ZrAl_4C_4$ and (b) Al_4C_3. The unit cells are represented by solid lines. The atom numbering in (b) referred to the original manuscript.[11]

3.2 Synthesis and crystal structure of a new layered carbide $ZrAl_8C_7$

Abstract

A new ternary layered carbide, $ZrAl_8C_7$, has been synthesized and characterized by X-ray powder diffraction. The crystal structure was determined using direct methods, and further refined by the Rietveld method. The crystal is trigonal (space group $R\bar{3}m$, $Z = 3$) with lattice dimensions $a = 0.332842(2)$ nm, $c = 5.78221(2)$ nm and $V = 0.554754(4)$ nm^3. The sample prepared was composed mainly of $ZrAl_8C_7$ with a small amount of $ZrAl_4C_4$. These two types of carbides have been found to form a homologous series with the general formula $(ZrC)_mAl_8C_6$, where $m = 1$ and 2. They show comparable intergrowth structures consisting of $[Zr_mC_{m+1}]$ layers separated by $[Al_8C_7]$ layers.

3.2.1 Introduction

In the system Zr-Al-C, there are three ternary carbides established so far; $Zr_2Al_3C_4$, $Zr_3Al_3C_5$ and $ZrAl_4C_4$ [1-3]. The former two compounds form a homologous series, the general formula of which is $(ZrC)_mAl_3C_2$ ($m = 2$ and 3) [2]. The crystal structures, belonging to the same space group $P6_3mc$, can be regarded as intergrowth structures where the Al_4C_3-type $[Al_3C_3]$ layers are the same, while the NaCl-type $[Zr_mC_{m+1}]$ layers increase in thickness with increasing m value. The compound $ZrAl_4C_4$ (space group $P3m1$) also shows the intergrowth structure with the NaCl-type $[Zr_2C_3]$ ($m = 2$) thin slabs separated by the Al_4C_3-type $[Al_8C_7]$ layers [3].

The $[Zr_mC_{m+1}]$ and $[Al_3C_3]$ layers in $(ZrC)_mAl_3C_2$ share the two-dimensional networks of carbon atoms at their boundaries [2]. The distances (0.3347 nm for $m = 2$ and 0.3346 nm for $m = 3$) are comparable to each other, and also to the C-C distances of the ZrC and Al_4C_3 crystals; the former distance is 0.330 nm (= $a(ZrC)/\sqrt{2}$) and that of the latter is 0.334 nm (= $a(Al_4C_3)$), where $a(ZrC)$ and $a(Al_4C_3)$ represent the a-axis lengths. In our previous study, we have proposed that the closeness of the C-C distances between ZrC and Al_4C_3 crystals, being repressed by the equation $a(ZrC)/\sqrt{2} \sim a(Al_4C_3)$, is the principal reason for the formation of the homologous series $(ZrC)_mAl_3C_2$ [2]. This principle is applicable also to $ZrAl_4C_4$ since the C-C distance at the layer boundary is 0.3325 nm.

In the present study, we have expected the further application of the principle to the Zr-Al-C system and actually confirmed the existence of a new layered carbide. The crystal structure has been determined from X-ray powder diffraction (XRPD) data using direct methods, and described in relation to that of $ZrAl_4C_4$.

3.2.2 Experimental Procedure

The new ternary carbide was initially recognized as unidentifiable diffraction lines in the XRPD patterns of the reacted ZrC-Al_4C_3 mixtures. We obtained the powder specimen that was mainly consisting of the new carbide together with a small amount of $ZrAl_4C_4$ by the following procedure. The reagent-grade chemicals of ZrC (99.9%, KCL Co., Ltd, Saitama, Japan) and Al_4C_3 (KCL, 99. 9%) were mixed in molar ratios of $ZrC : Al_4C_3 = 1 : 2$, which is equivalent to $[Zr : Al : C] = [1 : 8 : 7]$. The well-mixed chemicals were pressed into compacts (10 mm × 10 mm × 5 mm), heated at 2273 K for 3 h in inert gas atmosphere of Ar, followed by cooling to ambient temperature by cutting furnace power. The reaction product was a slightly sintered polycrystalline material. It was finely ground to obtain powder specimen.

The XRPD intensities of the powder specimen were collected on a diffractometer (X'Pert PRO Alpha-1, PANalytical B.V., Almelo, the Netherlands) equipped with a high speed detector in Bragg-Brentano geometry using monochromatized $CuK\alpha_1$ radiation (45kV, 40mA) in a 2θ range from $2.0052°$ to $148.9056°$ (the accuracy in 2θ of $\pm0.0001°$). The automatic divergence slit was employed to collect the quantitative profile intensities over the 2θ range of $2\theta \geq 5°$. Other experimental conditions were: continuous scan, total of 17582 datapoints and total experimental time of 11.7 h. The structure data were standardized using the computer program STRUCTURE TIDY [4]. The crystal-structure models were visualized with the computer program VESTA [5].

3.2.3 Results and Discussion

(1) Crystal structure determination

The XRPD pattern in Fig. 3-4 showed the presence of weak diffraction intensities peculiar to $ZrAl_4C_4$. All of the other diffraction peaks were successfully indexed with a hexagonal unit cell. The unit-cell parameters and integrated intensities of the unknown phase were exclusively refined by the Le Bail method [6] using the computer program RIETAN-FP [7]. The refined unit-cell dimensions were $a = 0.332854$ nm and $c = 5.78215$ nm. The integrated intensities were examined to confirm the presence or absence of reflections. There were systematic absences $h - k + l \neq 3n$ for $hkil$, $-h + l \neq 3n$ for $hh0l$, $l \neq 3n$ for $hh2hl$ and $l \neq 3n$ for $000l$, implying that the possible space groups are $R3$, $R\bar{3}$, $R32$, $R3m$ and $R\bar{3}m$.

In general, the number of formula units in the unit cell (Z) is determined from the unit-cell volume V (nm^3), true density D_t (Mgm^{-3}) and molecular weight M (g) as follows:

$$Z = VD_t/(M \times 1.660 \times 10^{-3}). \tag{1}$$

The most probable molar ratios of [Zr : Al : C] are [1 : 8 : 7] for the unknown phase, and hence the chemical formula would be $ZrAl_8C_7$ $(M = 391.15$ g). Because the densities (Mgm^{-3}) are 2.98 [8] for Al_4C_3 and 3.90 [3] for $ZrAl_4C_4$, the D_t-value of $ZrAl_8C_7$ must be around 3.4 (= (2.98 + 3.90)/2). Substituting 391.15 g, 0.55479 nm^3 and 3.4 $Mg \cdot m^{-3}$ for, respectively, M-, V- and D_t-values in equation (1) yields 2.9 for an approximate value of Z. Thus, the Z-value must be equal to 3, which indicates that the unit cell content is [3Zr 24Al 21C].

All of the possible space groups were tested using the EXPO2004 package [9] for crystal structure determination. The individual integrated intensities that were refined by the Le Bail method were used for the direct methods. A promising structural model was successfully obtained for the space group $R3m$ (centrosymmetric). There are 9 independent atoms in the unit cell; one Zr atoms (Zr site located on Wyckoff position $3b$), four Al atoms (Al(1), Al(2), Al(3) and Al(4) sites on $6c$) and four C atoms (C(1) site on $3a$ and C(2), C(3) and C(4) sites on $6c$).

Structural parameters were refined by the Rietveld method [10] using the computer program RIETAN-FP [7] in a 2θ range of $5.00°$ to $148.90°$ (Fig. 3-4). A Legendre polynomial was fitted to background intensities with twelve adjustable parameters. The split Pearson VII function [11] was used to fit the peak profile. The isotropic atomic displacement parameters (B) of the C sites were constrained to have the same value. Reliability indices [12] for a final result were $R_{wp} = 7.42\%$ ($S = 1.34$), $R_p = 5.59\%$, $R_B = 1.93\%$ and $R_F = 1.23\%$. Crystal data are given in Table 3-4, and the final atomic positional and B parameters are given in Table 3-5. The selected interatomic distances, together with their standard deviations, are given in Table 3-6. Quantitative X-ray analysis with correction for microabsorption according to Brindley's procedure [13] was implemented in the program RIETAN-FP.

The phase composition of the sample was found to be 83.0 mass% $ZrAl_8C_7$ and 17.0 mass% $ZrAl_4C_4$. The latter carbide was most probably formed by the deficiency of Al_4C_3 component, which was caused by the evaporation of Al_4C_3 compound during heating.

(2) Structure description

The crystal structure of $ZrAl_8C_7$ can be regarded as intergrowth structure, which consists of the $[ZrC_2]$ ($m = 1$ for $[Zr_mC_{m+1}]$) layers with thickness of ~0.279 nm separated by the $[Al_8C_7]$ layers of ~1.648 nm thickness (Fig. 3-5). The mean interatomic distances in $ZrAl_8C_7$ compare well with those of ZrC, Al_4C_3, $Zr_2Al_3C_4$, $Zr_3Al_3C_5$ and $ZrAl_4C_4$. The Zr atoms are octahedrally coordinated by C atoms with the Zr-C distance of 0.238 nm (Table 3-6), which is comparable to those of the $[ZrC_6]$ polyhedra in NaCl-type ZrC (0.235 nm), $Zr_2Al_3C_4$ (0.241 nm) [2], $Zr_3Al_3C_5$ (0.239 nm) [1] and $ZrAl_4C_4$ (0.237 nm) [3]. The Zr-Zr distance of 0.3328 nm in $ZrAl_8C_7$ is comparable to those of ZrC (0.332 nm), $Zr_2Al_3C_4$ (0.335 nm), $Zr_3Al_3C_4$ (0.331 nm) and $ZrAl_4C_4$ (0.3325 nm). The Al atoms are tetrahedrally coordinated with the mean distances of 0.201 nm for Al(1)-C, 0.207 nm for Al(2)-C, 0.202 nm for Al(3)-C and 0.210 nm for Al(4)-C. Accordingly, the Al-C distances are comparable to the Al-C distances of the $[AlC_4]$ tetrahedra in Al_4C_3, ranging from 0.199 to 0.209 nm (the mean = 0.205 nm) [8]. In Fig. 3-6, the atomic configurations are shown for $ZrAl_8C_7$, $ZrAl_4C_4$ and Al_4C_3. The $[Al_8C_7]$ layer of the former is clearly demonstrated to be structurally comparable to those of the latter two carbides.

The crystal structures of $ZrAl_8C_7$ (space group $R3m$ and $Z = 3$) and $ZrAl_4C_4$ ($P3m1$ and $Z = 2$) can be regarded as intergrowth structures consisting of the two types of layers; one is composed of $[Zr_mC_{m+1}]$ and the other consists of $[Al_8C_7]$. The atom arrangements in the $[Al_8C_7]$ layers of $ZrAl_8C_7$ and $ZrAl_4C_4$ are, regardless of the difference in space group for the crystal structures, isomorphous with each other, while the $[Zr_mC_{m+1}]$ slabs are thicker for the latter than for the former. Accordingly, these two compounds form a homologous series with the general formula $(ZrC)_mAl_8C_6$, where $m = 1$ $(ZrAl_8C_7)$ and 2 $(ZrAl_4C_4)$. The C-C distances at the layer boundaries are nearly equal to each other (0.3328 nm for $m = 1$ and 0.3325 nm for $m = 2$) and also comparable to those of the ZrC and Al_4C_3 crystals, in accord with the principle of the formation of layered carbides in the Zr-Al-C system [2]. The principle could be also applicable to the recently reported layered carbides $Zr_4Al_3C_6$, $Zr_5Al_6C_9$, and $Zr_7Al_6C_{11}$ [14]. However, these materials were only recognized under TEM, hence the precise structural characterization would be needed for further discussion.

3.2.4 Conclusion

In the Zr-Al-C system, we have successfully synthesized the new carbide $ZrAl_8C_7$. The crystal structure was determined from XRPD data and described in relation to that of $ZrAl_4C_4$. These two crystal structures were considered to be composed of the $[Zr_mC_{m+1}]$ slabs separated by the Al_4C_3-type $[Al_8C_7]$ layers. The two carbides form a homologous series, the general formula of which is represented by $(ZrC)_mAl_8C_6$, where $m = 1$ and 2.

References

[1] Th. M. Gesing and W. Jeitschko, *J. Solid State Chem.*, **140**, 396-401 (1998).

[2] K. Fukuda, S. Mori, and S. Hashimoto , *J. Am. Ceram. Soc.*, **88**, 3528-30 (2005).

[3] T. Iwata, E. Hattori, S. Hashimoto, and K. Fukuda, *J. Am. Ceram. Soc.*, **91**, 2713–2715 (2008).

[4] L. M. Gelato and E. Parthé, *J. Appl. Crystallogr.*, **20**, 139-43 (1987).

[5] K. Momma and F. Izumi, *J. Appl. Cryst.*, **41**, 653-58 (2008).

[6] A. Le Bail, H. Duroy, and J. L. Fourquet, *Mater. Res. Bull.*, **23**, 447-52 (1988).

[7] F. Izumi and T. Ikeda, *Mater. Sci. Forum,* **321-324**, 198-203 (2000).

[8] Th. M. Gesing and W. Jeitschko, *Z. Naturforsch.*, **50b**, 196-200 (1995).

[9] A. Altomare, M. C. Burla, M. Camalli, B. Carrozzini, G. L. Cascarano, C. Giacovazzo, A. Guagliardi, A. G. G. Moliterni, G. Polidori, and R. Rizzi, *J. Appl. Crystallogr.*, **32**, 339-40 (1999).

[10] H. M. Rietveld, *Acta Crystallogr.*, **22**, 151-52 (1967).

[11] H. Toraya, *J. Appl. Crystallogr.*, **23**, 485-91 (1990).

[12] R. A. Young, in: R. A. Young (Ed.), The Rietveld Method, Oxford University Press, Oxford, U.K., 1993, pp. 1-38.

[13] G. W. Brindley, *Bulletin de la Societe Chimique de France*, D59-63 (1949).

[14] Z. J. Lin, L. F. He, M. S. Li, J. Y. Wang, and Y. C. Zhou, *J. Mat. Res.*, **22**, 3058-66 (2007).

Table 3-4. Crystal data for $ZrAl_8C_7$

Chemical composition	$ZrAl_8C_7$
Space group	$R\bar{3}m$
a/nm	0.332842(2)
c/nm	5.78221(2)
V/nm^3	0.554754(4)
Z	3
D_x/Mgm^{-3}	3.51

Table 3-5. Structural parameters for $ZrAl_8C_7$

Site	Wyckoff position	x	y	z	$100 \times B$/nm^2
Zr	$3b$	0	0	0.5	0.90(3)
Al(1)	$6c$	0	0	0.05638(2)	0.65(3)
Al(2)	$6c$	0	0	0.12736(3)	0.62(3)
Al(3)	$6c$	0	0	0.24463(2)	0.65(3)
Al(4)	$6c$	0	0	0.31615(2)	0.63(3)
C(1)	$3a$	0	0	0	0.27(5)
C(2)	$6c$	0	0	0.09380(6)	0.27
C(3)	$6c$	0	0	0.19080(6)	0.27
C(4)	$6c$	0	0	0.28328(6)	0.27

Table 3-6. Interatomic distances (nm) in $ZrAl_8C_7$*

*All distances shorter than 0.30 nm (metal-metal) and 0.33 nm (metal-carbon) are given

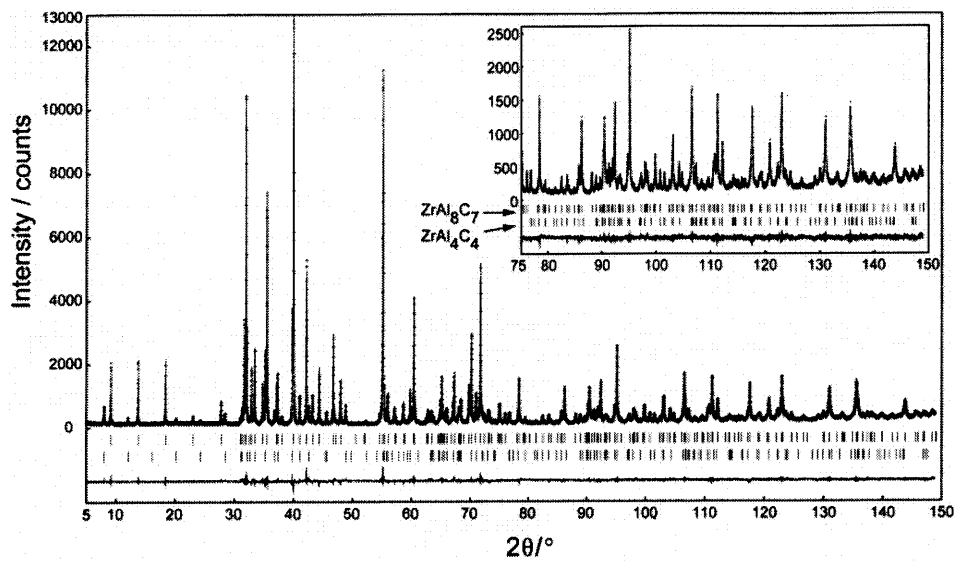|	
Zr-C(3)	0.2375(2) × 6
Zr-Al(2)	0.2976(1) × 6
Al(1)-C(4)	0.19561(7) × 3
Al(1)-C(2)	0.2164(3)
Al(1)-Al(3)	0.2681(2) × 3
Al(1)-Al(4)	0.2972(2) × 3
Al(1)-C(1)	0.3260(1)
Al(2)-C(2)	0.1941(3)
Al(2)-C(3)	0.2112(2) × 3
Al(2)-Al(3)	0.2948(2) × 3
Al(2)-Zr	0.2976(1) × 3
Al(3)-C(2)	0.19441(5) × 3
Al(3)-C(4)	0.2235(4)
Al(3)-Al(1)	0.2681(2) × 3
Al(3)-Al(2)	0.2948(2) × 3
Al(3)-C(3)	0.3113(4)
Al(4)-C(4)	0.1901(4)
Al(4)-C(1)	0.21632(6) × 3
Al(4)-Al(4)	0.2764(2) × 3
Al(4)-Al(1)	0.2972(2) × 3

Fig.3-4. Comparison of observed diffraction pattern of $ZrAl_8C_7$ and $ZrAl_4C_4$ (symbol: +) with the corresponding calculated pattern (upper solid line). The difference curve is shown in the lower part of the diagram. Upper vertical bars indicate the positions of possible Bragg reflections for $ZrAl_8C_7$ and those of the lower for $ZrAl_4C_4$.
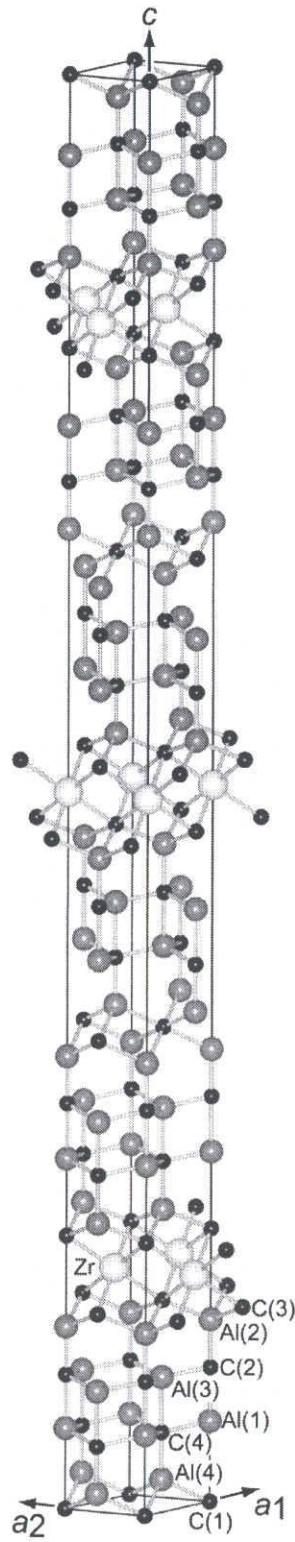
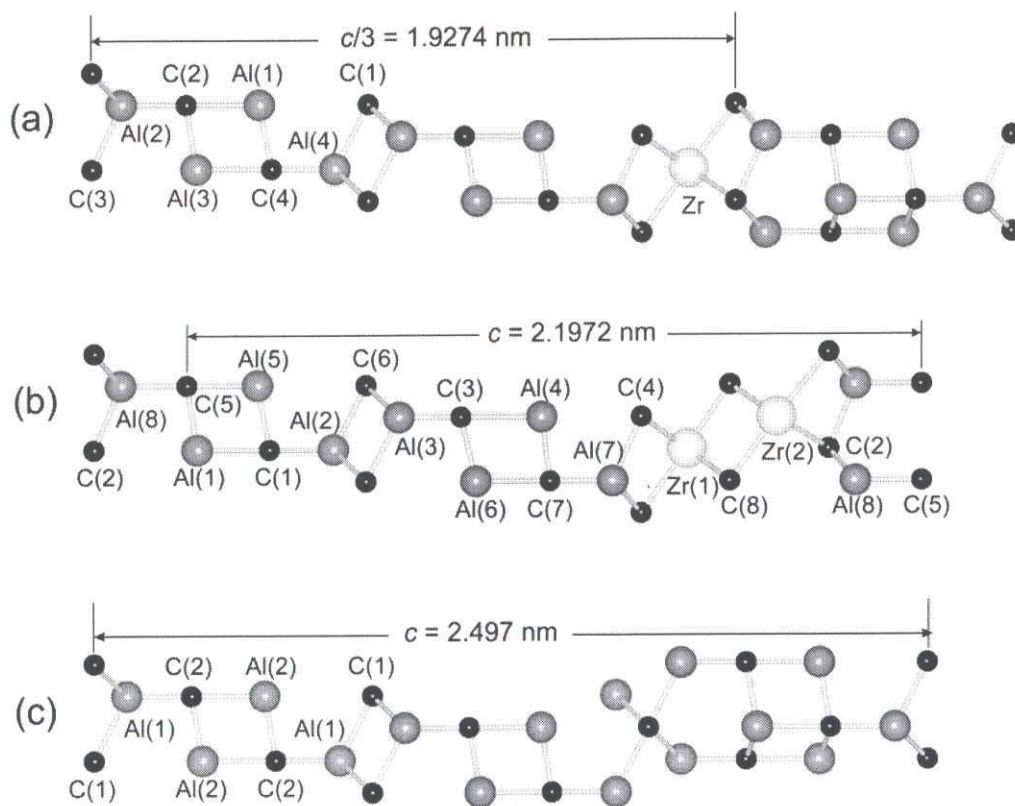Fig.3-5. Crystal structure of $ZrAl_8C_7$.

Fig.3-6. Atomic configurations in (a) $ZrAl_8C_7$, (b) $ZrAl_4C_4$ and (c) Al_4C_3. The unit cells are represented by solid lines. The atom numbering in (b) and (c) referred to the original manuscripts.[3,8]

3.3 Syntheses and crystal structures of Si-bearing layered carbides $ZrAl_8C_7$ and $ZrAl_4C_4$

Abstract

Two types of new quaternary carbide solid solutions, $(ZrC)[Al_{1-x}Si_x]_8C_6$ with $x = 0.06$ and $(ZrC)[Al_{1-y}Si_y]_4C_3$ with $y = 0.04$, have been synthesized and characterized using a laboratory X-ray powder diffraction ($CuK\alpha_1$), transmission electron microscopy and energy dispersive X-ray spectroscopy (EDX). The average atom ratios [Al : Si] of both carbides were determined by EDX, and the crystal structures were refined using the Rietveld method. These carbides have been found to form a homologous series with the general formula $(ZrC)_m[Al_{1-z}Si_z]_8C_6$ ($0 \leq z \leq 0.07$), where $m = 1$ and 2. The crystal structures can be regarded as intergrowth structures, consisting of the NaCl-type $[Zr_mC_{m+1}]$ slabs separated by the Al_4C_3-type $[(Al_{1-z}Si_z)_8C_7]$ layers.

Keywords: Layered carbides, Solid solutions, Crystal structures, Powder diffraction, Rietveld refinement

3.3.1 Introduction

In the system Zr-Al-C, two types of new ternary carbides, $(ZrC)Al_8C_6$ [1] and $(ZrC)Al_4C_3$ [2], have been synthesized at 2273 K and structurally characterized by X-ray powder diffraction (XRPD) method. These carbides form a homologous series with the general formula $(ZrC)_mAl_8C_6$ ($m = 1$ and 2) [1]. Both crystal structures, although belonging to the different space groups $R3m$ for $m = 1$ and $P3m1$ for $m = 2$, can be regarded as intergrowth structures where the Al_4C_3-type $[Al_8C_7]$ layers are the same, while the NaCl-type $[Zr_mC_{m+1}]$ layers increase in thickness with increasing m value. In the ternary system, the other carbides reported so far are $(ZrC)_2Al_4C_3$, $(ZrC)_3Al_4C_3$, $(ZrC)_2Al_3C_2$ and $(ZrC)_3Al_3C_2$ [3-5]. The former two carbides, which have been synthesized at 2073 K, also form a homologous series with the general formula of $(ZrC)_mAl_4C_3$ ($m = 2$ and 3) [3]. The considerable amounts of Si component have been found to dissolve into the $[Al_4C_4]$ layers of $(ZrC)_mAl_4C_3$ at the lower temperatures than 2073 K (*i.e.*, 1873 – 1973 K) to stabilize the crystal structures [3, 6, 7]. Thus, the ternary carbides $(ZrC)_mAl_4C_3$ are considered to be the end members of the solid solutions. Because the atomic scattering factors for Al and Si are almost the same, these atoms were assumed to be randomly distributed over the same sites in the Al_4C_3-type layers, although there might be the site preference of these atoms.

Thermoelectric materials with high efficiency of energy conversion are of interest for applications as heat pumps and power generators. Low-dimensional materials that consist of, for example, conducting two-dimensional (2D) layers are promising for thermoelectric energy conversion [8-11]. The advantage of the low dimensionality can be interpreted in terms of the carrier confinement effect in the 2D layers, which leads to an enlarged absolute value of the Seebeck coefficient compared to the materials with three-dimensional conducting paths. The crystal structures of the layered carbides in the Zr-Al-C and/or Zr-Al-Si-C systems are composed of the electroconductive $[Zr_mC_{m+1}]$ layers separated by the less conductive [(Al,Si)C] layers. Hence, the homologous carbides demonstrated good performance of thermoelectricity, and regarded as the promising thermoelectric materials [6, 7].

In the present study, we have successfully dissolved the Si component into the $[Al_8C_7]$ layers of $(ZrC)_mAl_8C_6$ ($m = 1$ and 2) to stabilize the crystal structures at 2073 K, which is 200 K lower than the formation temperature of the end members.

3.3.2 Experimental procedure

(1) Materials

In the reacted ZrC-Al_4C_3-SiC mixtures, two types of new quaternary carbides were initially recognized by their very similar diffraction patterns to those of $(ZrC)_mAl_8C_6$ with m =1 and 2 [1,2]. Since the present specimens contain Si component, the new carbides are most probably of Si-dissolved $(ZrC)_mAl_8C_6$ solid solutions. We obtained, by the following procedures, the two types of powder samples; one consisted mainly of $(ZrC)[Al,Si]_8C_6$ (sample S-A) and the other was mainly composed of $(ZrC)[Al,Si]_4C_3$ (S-B).

The reagent-grade chemicals of ZrC (99.9%, KCL Co., Ltd, Saitama, Japan), Al_4C_3 (KCL, 99.9%) and SiC (KCL, 99.9%) were mixed in two different molar ratios of [ZrC : Al_4C_3 : SiC] = [1 : 3 : 1] for S-A and [4 : 6 : 1] for S-B. Each of the well-mixed chemicals was pressed into pellets (ϕ 13 mm × 10 mm), heated at 2073 K for 1 h in vacuum, followed by cooling to ambient temperature by cutting furnace power. Both reaction products were slightly sintered polycrystalline materials. They were finely ground to obtain powder specimens. Small amounts of Al_4C_3 crystallites coexisted in both samples. These crystals in S-B were completely removed by dissolution with acid solution. On the other hand, the crystals of $(ZrC)[Al,Si]_8C_6$ also dissolved in the acid solution. Hence, the acid treatment of selectively dissolving the Al_4C_3 compound was inapplicable to the sample S-A.

(2) Characterization

XRPD intensities were collected on a diffractometer (X'Pert PRO Alpha-1, PANalytical B.V., Almelo, The Netherlands) equipped with a high speed detector in Bragg-Brentano geometry using monochromatized $CuK\alpha_1$ radiation (45kV, 40mA) in a 2θ range from 2.0052° to 148.9056° (the accuracy in 2θ of ±0.0001°). The divergence slit of 0.25° and the automatic divergence slit were employed, respectively, for samples S-A and S-B to collect the quantitative profile intensities over the whole 2θ range. Other experimental conditions were: continuous scan, total of 17582 datapoints and total experimental time of 5.0 h. The crystal-structure models were visualized with the computer program VESTA [12].

The powder specimens were examined using transmission electron microscopes (JEM 3000F and JEM 2010, JEOL ltd., Tokyo, Japan) and equipped with an energy dispersive X-ray analyzer (EDX; VOYAGER III, NORAN Instruments, Middleton, WI, USA). The powder particles were deposited with ethyl alcohol on a copper grid. Selected area electron diffraction (SAED) patterns and corresponding lattice images were obtained. Chemical analyses were made for eight crystal fragments of $(ZrC)[Al,Si]_8C_6$ in S-A and seven fragments of $(ZrC)[Al,Si]_4C_3$ in S-B to determine the individual atom ratios [Al : Si]. The corrections were made by the ZAF routines.

3.3.3 Results and Discussion

(1) Structure refinement

The SAED pattern [Fig. 3-7(a)] of $(ZrC)[Al,Si]_4C_3$ in S-B was successfully indexed with a hexagonal unit cell with dimensions of $a \approx 0.33$ nm and $c \approx 2.2$ nm. The corresponding lattice image [Fig. 3-7(b)] strongly suggests that the crystal structure is built up from stacking combinations of two basic sheets. The presence of Si atoms within both carbides has been well confirmed by the EDX analysis. In S-A, the average atom ratios [Zr : Al : Si] were found to be [10.9(1.3) : 83.9(1.8) : 5.3(1.2)], where the figures in parentheses indicate standard deviations. The atom ratios are almost equivalent to [Zr : Al+Si] = [1 : 8], with the [Al : Si] ratios being [0.94(1) : 0.06(1)] on the basis of Al + Si = 1. The [Al : Si] ratios of the carbide in S-B were determined to be [0.96(1) : 0.04(1)] based on

the average atom ratios of [Zr : Al : Si] = [20.2(1.5) : 76.7(2.2) : 3.1(0.8)], which are nearly equivalent to [Zr : Al+Si] = [1 : 4]. Accordingly, the chemical formulas would be satisfactorily represented by $(ZrC)[Al_{0.94(1)}Si_{0.06(1)}]_8C_6$ in S-A and $(ZrC)[Al_{0.96(1)}Si_{0.04(1)}]_4C_3$ in S-B.

Initial structural parameters of $(ZrC)[Al_{0.94}Si_{0.06}]_8C_6$ and $(ZrC)[Al_{0.96}Si_{0.04}]_4C_3$ were taken from those determined by Iwata *et al.* for $(ZrC)Al_8C_6$ and $(ZrC)Al_4C_3$, respectively [1, 2]. The structural parameters were individually refined by the Rietveld method using the computer program RIETAN-FP [13]. The structure models of Al_4C_3 [14], Al_4SiC_4 [15], $(ZrC)Al_4C_3$ [2] and $(ZrC)_2Al_4C_3$ [3] were added into the refinement as additional phases. A Legendre polynomial was fitted to background intensities with twelve adjustable parameters. The split Pearson VII function [16] was used to fit the peak profile. The Al and Si atoms were assumed to be randomly distributed over the same sites (denoted by T sites) in the crystal structures without any constrains on occupancies, although there might be the site preference of these atoms. All of the isotropic atomic displacement parameters (B) of carbon atoms were constrained to have the same value. The reliability indices [17] for the final result of S-A were $R_{wp} = 8.03\%$, $S = 1.24$ and $R_p = 6.01\%$ ($R_B = 2.33\%$ and $R_F = 1.18\%$ for $(ZrC)[Al_{0.94}Si_{0.06}]_8C_6$) [Fig. 3-8(a)] and those of S-B were $R_{wp} = 6.93\%$, $S = 1.30$ and $R_p = 5.31\%$ ($R_B = 1.94\%$ and $R_F = 1.07\%$ for $(ZrC)[Al_{0.96}Si_{0.04}]_4C_3$) [Fig. 3-8(b)]. Crystal data are given in Tables 3-7 and 3-8, and the final atomic positional and B parameters are given in Tables 3-9 and 3-10. Quantitative X-ray analysis with correction for microabsorption according to Brindley's procedure [18] was implemented in the program RIETAN-FP. The phase compositions were determined to be 76.4 mass% $(ZrC)[Al_{0.94}Si_{0.06}]_8C_6$, 13.1 mass% Al_4SiC_4, 5.4 mass% Al_4C_3 and 5.1 mass% $(ZrC)Al_4C_3$ for S-A and 92.6 mass% $(ZrC)[Al_{0.96}Si_{0.04}]_4C_3$ and 7.4 mass% $(ZrC)_2Al_4C_3$ for S-B.

The EDX analysis showed that the atom ratios of both quaternary carbides varied slightly but certainly from crystal fragment to fragment, indicating that these carbides are not compounds but solid solutions. The atom ratios [Al : Si] in S-A almost varied from [0.95 : 0.05] to [0.93 : 0.07], indicating that the maximum Si/(Al+Si)-value is most probably 0.07. Thus, the carbide solid solution would be satisfactorily represented by the general formula $(ZrC)[Al_{1-x}Si_x]_8C_6$ with $0 \leq x \leq 0.07$. In the same manner, the chemical variation in S-B was within the solid-solution range of $0 \leq y \leq 0.05$ for $(ZrC)[Al_{1-y}Si_y]_4C_3$, because the [Al : Si] ratios almost ranged from [0.97 : 0.03] to [0.95 : 0.05].

(2) Structure description

The crystal structures may be regarded as intergrowth structures (Fig. 3-9), which consist of the NaCl-type $[Zr_mC_{m+1}]$ layers (thickness of ~0.28 nm for $m = 1$ and ~0.56 nm for $m = 2$) separated by the Al_4C_3-type $[(Al_{1-z}Si_z)_8C_7]$ layers with ~1.64 nm thickness ($0 \leq z \leq 0.07$). The selected interatomic distances, together with their standard deviations, are given in Tables 3-11 and 3-12. The mean interatomic distances in $(ZrC)[Al_{0.94}Si_{0.06}]_8C_6$ and $(ZrC)[Al_{0.96}Si_{0.04}]_4C_3$ compare well with those of ZrC, Al_4C_3, $(ZrC)Al_8C_6$ and $(ZrC)Al_4C_3$. The Zr sites are octahedrally coordinated by C atoms with the mean distances of 0.238 nm for $m = 1$ and 0.237 nm for $m = 2$, which are comparable to those of the ZrC_8 polyhedra in ZrC (0.235 nm), $(ZrC)Al_8C_6$ (0.238 nm) and $(ZrC)Al_4C_3$ (0.237 nm) [1, 4, 5]. The mean Zr-T distances of 0.296 nm for $m = 1$ and 0.298 nm for $m = 2$ are comparable to the Zr-Al distances of $(ZrC)Al_8C_6$ (0.298 nm) and $(ZrC)Al_4C_3$ (0.299 nm). The T sites are tetrahedrally coordinated with the mean distances of 0.204 nm for both $m = 1$ and $m = 2$. These T-C distances are comparable to the Al-C distances of the AlC_4 tetrahedra in Al_4C_3 ranging from 0.194 to 0.218 nm (the mean = 0.206 nm) [10], which implies that the $[(Al_{1-z}Si_z)_8C_7]$ layers of both $m = 1$ and $m = 2$ are structurally comparable to the compound Al_4C_3. Accordingly, these carbide solid solutions form a homologous series with the general formula of $(ZrC)_m[Al_{1-z}Si_z]_8C_6$ ($m = 1$ and 2) with $0 \leq z \leq 0.07$.

3.3.4 Conclusions

In the Zr-Al-Si-C system, we have successfully synthesized the two types of new carbide solid solutions $(ZrC)[Al_{1-x}Si_x]_8C_6$ ($x = 0.06$) and $(ZrC)[Al_{1-y}Si_y]_4C_3$ ($y = 0.04$), the end members of which were, respectively, $(ZrC)Al_8C_6$ and $(ZrC)Al_4C_3$. The crystal structures were considered to be composed of the NaCl-type $[Zr_mC_{m+1}]$ slabs separated by the Al_4C_3-type $[(Al_{1-z}Si_z)_8C_7]$ layers, and hence they formed a homologous series with the general formula of $(ZrC)_m[Al_{1-z}Si_z]_8C_6$ ($m = 1$ and 2) with $0 \le z \le 0.07$.

Acknowledgments

References

[1] T. Iwata, K. Sugiura, S. Hashimoto and K. Fukuda, *J. Am. Ceram. Soc.*, **91**, 3758-3761 (2008)

[2] T. Iwata, E. Hattori, S. Hashimoto and K. Fukuda, *J. Am. Ceram. Soc.*, **91**, 2713–2715 (2008)

[3] K. Sugiura, T. Iwata, H. Yoshida, S. Hashimoto and K. Fukuda, *J. Solid State Chem.*, in press.

[4] K. Fukuda, S. Mori and S. Hashimoto, *J. Am. Ceram. Soc.*, **88**, 3528-3530 (2005).

[5] Th. M. Gesing and W. Jeitschko, *J. Solid State Chem.*, **140**, 396-401 (1998).

[6] K. Fukuda, M. Hisamura, T. Iwata, N. Tera and K. Sato, *J. Solid State Chem.*, **180**, 1809-1815 (2007).

[7] K. Fukuda, M. Hisamura, Y. Kawamoto and T. Iwata, *J. Mater. Res.*, **22**, 2888-2894 (2007).

[8] L.D. Hicks and M.S. Dresselhaus, *Phys. Rev.*, **B47**, 12727-31 (1993).

[9] L.D. Hicks and M.S. Dresselhaus, *Phys. Rev.*, **B47**, 16631-34 (1993).

[10] L.D. Hicks, T. C. Harman, and M.S. Dresselhaus, *Appl. Phys. Lett.*, **63**, 3230-32 (1993).

[11] K. Koumoto, H. Koduka, and W.-S. Seo, *J. Mater. Chem.*, **11**, 251-52 (2001).

[12] F. Izumi and K. Momma, *Solid State Phenom.*, **130**, 15-20 (2007).

[13] F. Izumi and T. Ikeda, *Mater. Sci. Forum*, **321-324**, 198-203 (2000).

[14] Th. M. Gesing and W. Jeitschko, *Z. Naturforsch.*, **50b**, 196-200 (1995).

[15] Z. Inoue, Y. Inomata, H. Tanaka and H. Kawabata, *J. Mat. Sci.*, **15**, 575-580 (1980).

[16] H. Toraya, *J. Appl. Crystallogr.*, **23**, 485-491 (1990).

[17] R. A. Young, "The Rietveld Method", Ed. by R. A. Young, Oxford University Press, Oxford, U.K., 1993, pp. 1-38.

[18] G. W. Brindley, *Bulletin de la Societe Chimique de France*, D59-63 (1949).
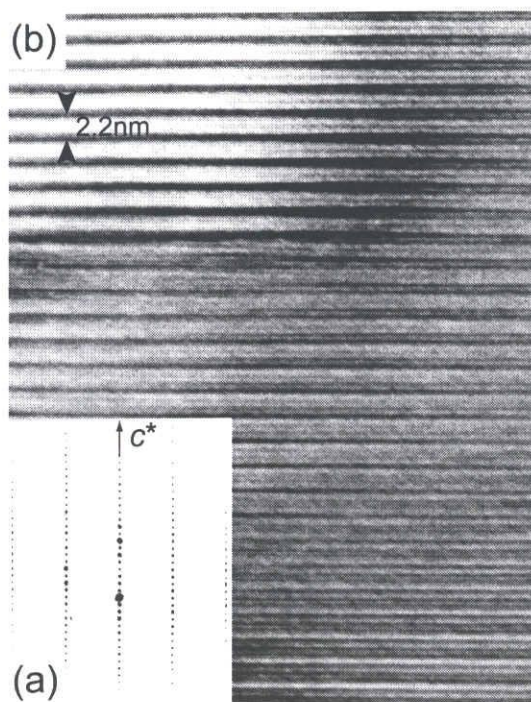
Fig.3-7. (a) Selected-area electron diffraction pattern and (b) corresponding lattice fringe image showing periodicity of about 2.2 nm (= c). Incident beam perpendicular to the c-axis. Sample $(ZrC)[Al_{0.96}Si_{0.04}]_4C_3$ in S-B.
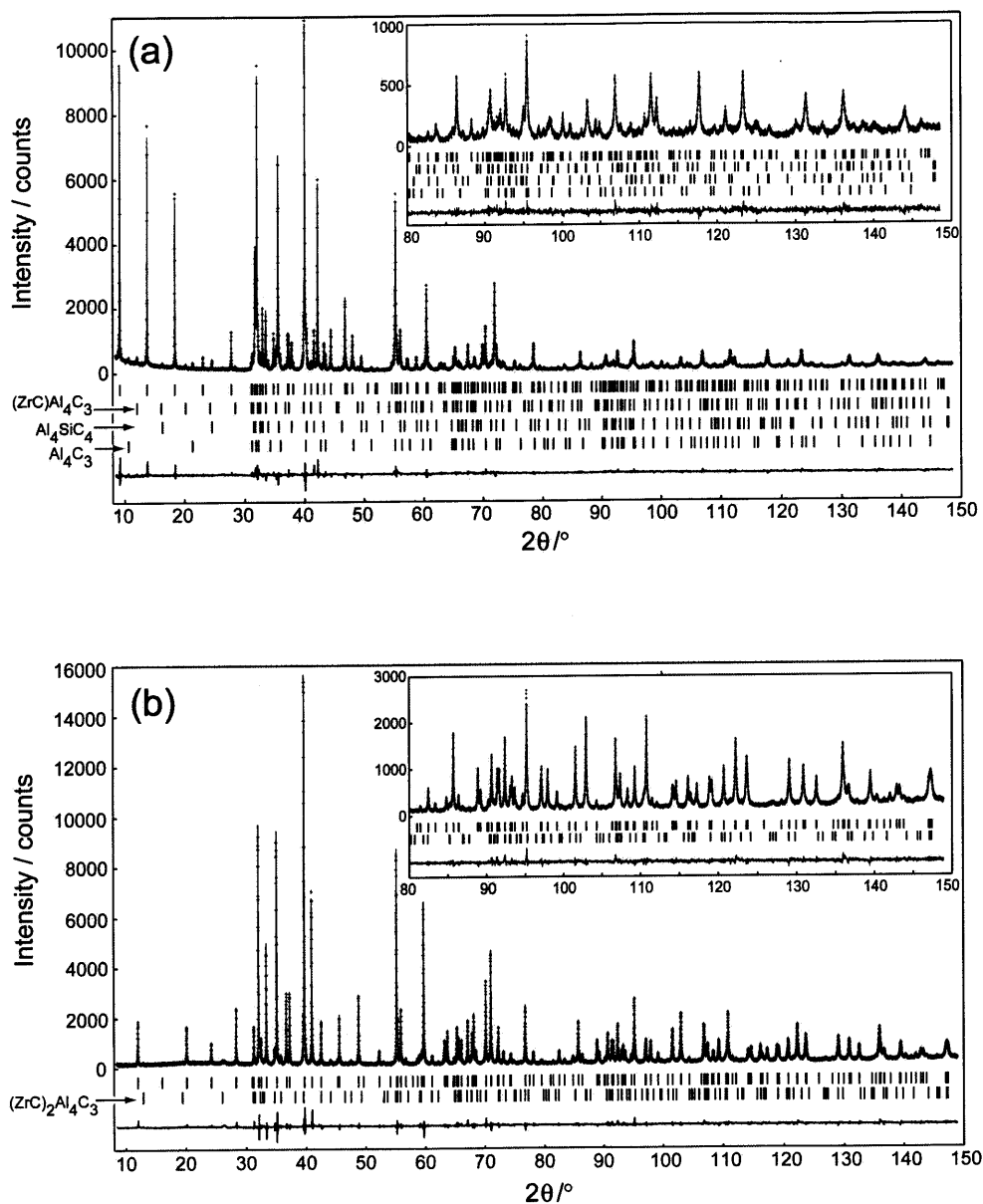
Fig.3-8. Comparison of the observed diffraction patterns (symbol: +) with the corresponding calculated patterns (upper solid lines). The difference curves are shown in the lower part of the diagrams. Upper vertical bars in each diagram indicate the positions of possible Bragg reflections. The profile intensities for (a) $(ZrC)[Al_{0.94}Si_{0.06}]_8C_6$, $(ZrC)Al_4C_3$, Al_4SiC_4 and Al_4C_3 in S-A and (b) $(ZrC)[Al_{0.96}Si_{0.04}]_4C_3$ and $(ZrC)_2Al_4C_3$ in S-B.

46
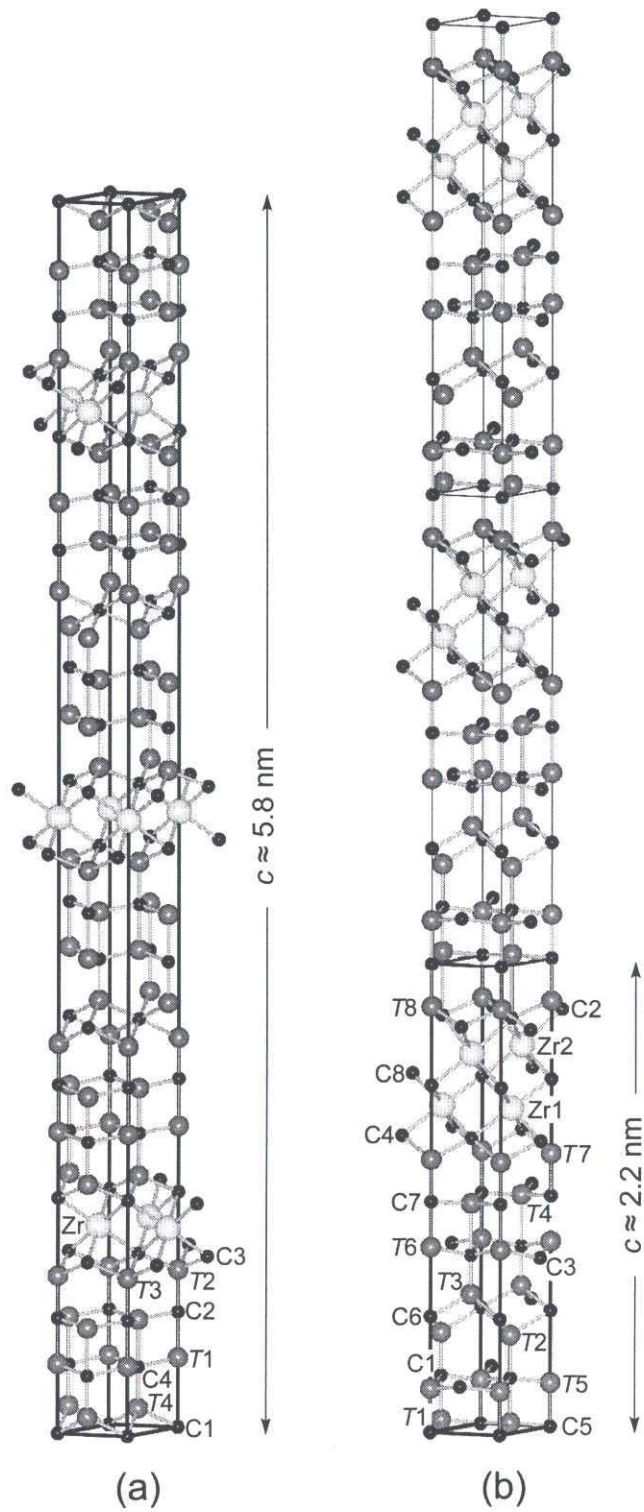
Fig. 3-9. Crystal structures of $(ZrC)[Al_{0.94}Si_{0.06}]_8C_6$ in (a) and $(ZrC)[Al_{0.96}Si_{0.04}]_4C_3$ in (b). The Al and Si atoms are assumed to be randomly distributed on the T sites for both crystal structures.

Table 3-7. Crystal data for $(ZrC)[Al_{0.94}Si_{0.06}]_8C_6$

Chemical composition	$Zr Al_{7.52}Si_{0.48}C_7$
Space group	$R3m$
a/nm	0.332214 (3)
c/nm	5.78236 (5)
V/nm^3	0.552678(8)
Z	3
D_x/Mgm^{-3}	3.53

Table 3-8. Crystal data for $(ZrC)[Al_{0.96}Si_{0.04}]_4C_3$

Chemical composition	$ZrAl_{3.84}Si_{0.16}C_4$
Space group	$P3m1$
a/nm	0.332349 (1)
c/nm	2.199241 (7)
V/nm^3	0.210375 (1)
Z	2
D_x/Mgm^{-3}	3.91

Table 3-9. Structural parameters for $(ZrC)[Al_{0.94}Si_{0.06}]_8C_6$
*z of C1 atom is fixed.

Site	Wyckoff position	x	y	z	$100 \times B$/nm^2
Zr	$3b$	0	0	1/2	0.63(3)
T1	$6c$	0	0	0.05647(3)	0.46(4)
T2	$6c$	0	0	0.12772(4)	0.41(3)
T3	$6c$	0	0	0.24448(3)	0.54(4)
T4	$6c$	0	0	0.31628(3)	0.50(5)
C1*	$3a$	0	0	0	0.50(6)
C2	$6c$	0	0	0.0933(1)	0.50
C3	$6c$	0	0	0.19092(9)	0.50
C4	$6c$	0	0	0.28286(9)	0.50

Table 3-10. Structural parameters for $(ZrC)[Al_{0.96}Si_{0.04}]_4C_3$

Site	Wyckoff position	x	y	z	$100 \times B/nm^2$
Zr1	1c	2/3	1/3	0.6824(9)	0.61(6)
Zr2	1b	1/3	2/3	0.8031(9)	0.61(6)
T1	1c	2/3	1/3	0.0122(10)	0.9(1)
T2	1c	2/3	1/3	0.1976(12)	0.9(3)
T3	1b	1/3	2/3	0.2889(12)	0.6(3)
T4	1b	1/3	2/3	0.4829(10)	1.0(1)
T5	1a	0	0	0.0930(11)	0.9(3)
T6	1a	0	0	0.3938(11)	0.8(3)
T7	1a	0	0	0.5812(10)	0.7(2)
T8	1a	0	0	0.9089(11)	0.7(2)
C1	1c	2/3	1/3	0.1069(12)	0.67(7)
C2	1c	2/3	1/3	0.8754(10)	0.67
C3	1b	1/3	2/3	0.3729(13)	0.67
C4	1b	1/3	2/3	0.6223(9)	0.67
C5*	1a	0	0	0	0.67
C6	1a	0	0	0.2458(15)	0.67
C7	1a	0	0	0.4911(4)	0.67
C8	1a	0	0	0.7404(16)	0.67

*z of C5 atom is fixed.

Table 3-11. Interatomic distances (nm) in $(ZrC)[Al_{0.94}Si_{0.06}]_8C_6$*
*All distances shorter than 0.30 nm (metal-metal) and 0.24 nm (metal-carbon) are given.

Zr-C3	0.2376(3) × 6
Zr-T2	0.2959(2) × 6
T1-C4	0.1949(1) × 3
T1-C2	0.2127(6)
T1-T3	0.2681(2) × 3
T1-T4	0.2979(2) × 3
T2-C2	0.1992(6)
T2-C3	0.2098(2) × 3
T2-T3	0.2954(2) × 3
T3-C2	0.19349(8) × 3
T3-C4	0.2219(5)
T4-C4	0.1933(5)
T4-C1	0.21566(9) × 3
T4-T4	0.2751(3) × 3

Table 3-12. Interatomic distances (nm) in $(ZrC)[Al_{0.96}Si_{0.04}]_4C_3$[*]

Zr1-C8	0.230(1) × 3
Zr1-C4	0.2331(7) × 3
Zr1-*T7*	0.294(1) × 3
Zr2-C8	0.236(2) × 3
Zr2-C2	0.249(1) × 3
Zr2-*T8*	0.3016(9) × 3
T1-C5	0.1937(3) × 3
T1-C1	0.208(1)
T1-*T5*	0.2616(9) × 3
T1-*T8*	0.2974(9) × 3
T2-C1	0.199(2)
T2-C6	0.219(1) × 3
T2-*T3*	0.2778(2) × 3
T2-*T5*	0.299(1) × 3
T3-C3	0.185(2)
T3-C6	0.214(1) × 3
T3-*T6*	0.300(1) × 3
T4-C7	0.1927(2) × 3
T4-C3	0.242(2)
T4-*T6*	0.274(1) × 3
T4-*T7*	0.289(1) × 3
T5-C1	0.1943(3) × 3
T5-C5	0.205(2)
T6-C3	0.1973(4) × 3
T6-C7	0.214(2)
T7-C7	0.198(2)
T7-C4	0.2121(7) × 3
T8-C5	0.200(2)
T8-C2	0.2055(8) × 3

[*]All distances shorter than 0.31 nm (metal-metal) and 0.25 nm (metal-carbon) are given.

3.4 First discovery and structural characterization of a new compound in Al-Si-O-C system

Abstract

A quaternary oxycarbide, $[Al_{16.77(5)}Si_{1.23(5)}]_{\Sigma 18}[O_{3.04(9)}C_{10.96(9)}]_{\Sigma 14}$, has been for the first time discovered in the Al-Si-O-C system. The crystal structure was characterized by X-ray powder diffraction, transmission electron microscopy and energy dispersive X-ray spectroscopy (EDX). The atom ratios [Al : Si] were determined by EDX, and the initial structural model was derived by the direct methods. The structural parameters as well as the atom ratios [O : C] were determined by the Rietveld method. The crystal is monoclinic (space group $C2/m$, $Z = 1$) with lattice dimensions $a = 0.57404(1)$ nm, $b = 0.331435(5)$ nm, $c = 1.92410(2)$ nm, $\beta = 90.036(1)°$ and $V = 0.366076(9)$ nm^3. The final structural model showed the positional disordering of Al/Si sites. The validity of the split-atom model was verified by the three-dimensional electron density distribution, the structural bias of which was reduced as much as possible using the maximum-entropy methods-based pattern fitting (MPF). The reliability indices calculated from the MPF were $R_{wp} = 4.20\%$ ($S = 1.14$), $R_p = 3.09\%$, $R_B = 0.92\%$ and $R_F = 1.05\%$. The crystal was an inversion twin with nearly the same twin fraction.

Keywords: Crystal structure; Powder diffraction; Rietveld method; New material; Oxycarbide.

3.4.1 Introduction

The binary and ternary carbides in the Al-Si-C system have the characteristics of layered structures [1-7]. The crystal structure of Al_4C_3 (space group $R\bar{3}m$, $Z = 3$) is composed of an $[Al_2C_2]$ double layer of AlC_4 tetrahedra surrounded by two $[AlC_2]$ single layers of AlC_4 tetrahedra [2,3]. These three layers form an $[Al_4C_4]$ unit layer (A). The complete structure is the superposition of three A layers along the c axis, in which the layer stacking sequence is described by $<AAA>$. There are five types of ternary carbides reported so far: Al_4SiC_4, $Al_4Si_2C_5$, $Al_4Si_3C_6$, $Al_4Si_4C_7$ and Al_8SiC_7 [1,4-7]. The crystal structures of the former two carbides have been determined by single crystal X-ray diffraction method [5]. The structure of Al_4SiC_4 ($P6_3mc$, $Z = 2$) requires an additional $[(Al,Si)C_2]$ single layer (B) of $(Al,Si)C_4$ tetrahedra in the hexagonal lattice to be alternately inserted between the A-type $[(Al,Si)_4C_4]$ unit layers with stacking sequence of $<BABA>$. With the rhombohedral lattice of $Al_4Si_2C_5$ ($R\bar{3}m$, $Z = 3$), the stacking sequence is $<BABBABBAB>$. Although crystal structures of $Al_4Si_3C_6$, $Al_4Si_4C_7$ and Al_8SiC_7 are still not elucidated, they could be made up of the combinations of A and B layers. Oscroft et al. have proposed the most probable stacking sequences in $Al_4Si_3C_6$ and $Al_4Si_4C_7$ [1]. Kidwell et al. have determined the hexagonal unit cell of $a = 0.33127(7)$ nm and $c = 1.9242(4)$ nm for Al_8SiC_7 [7].

In the Al-O-C system, two types of ternary oxycarbide compounds are known: Al_2OC [2,8-10] and Al_4O_4C [11,12]. The crystal structure of the former consists of mixed blocks described as $[AlO]_n[Al_2C_2]_n[AlO]_n$ with the C atoms in a similar environment to those in Al_4C_3 [2]. The structure of the latter can be described in terms of a three-dimensional network of $Al(O_3C)$ tetrahedra, which are associated by sharing edges and corners [12]. These crystal structures are distinct from those of the layered carbides in the Al-Si-C system. In the Al-Si-O-C system, quaternary compounds have never been recognized previously.

Recent advances in the field of crystal-structure analysis from X-ray powder diffraction (XRPD) data have enabled us to investigate unknown structures as well as disordered structures. To begin with initial structural models are required, which may be determined by, for example, direct

methods [13]. The structural parameters are subsequently refined using the Rietveld method [14]. In order to disclose the structural details that had not been introduced into the structural models, the combined use of a maximum-entropy method (MEM) [15] and a MEM-based pattern fitting (MPF) method [16] is employed. MEM is capable of estimating structure factors of unobserved reflections and improving those of overlapped reflections, which give MEM advantages over the classical Fourier method. However, the Rietveld and MEM analyses are insufficient to readily determine charge densities because the observed structure factors, F_O(Rietveld), are biased toward the structural model assuming intensity partitioning. The subsequent MPF method can minimize the structural bias. Thus, the MEM and MPF analyses are alternately repeated (REMEDY cycle) until the reliability indices reach minima. Crystal structures are represented not by structural parameters but by electron densities in MPF.

In the present study, we have for the first time discovered a new quaternary compound in the Al-Si-O-C system. We determined the initial structural model from XRPD data using direct methods and further modified it into a split-atom model, in which two of the five types of Al/Si sites were positionally disordered. The crystal is most probably an inversion twin with nearly the same twin fraction.

3.4.2 Experimental

(1) Synthesis

The reagent-grade chemicals of Al (99.9%, KCL Co., Ltd, Saitama, Japan), Si (KCL, 99.99%) and C (graphite, KCL, 99.7%) were mixed in molar ratios of Al : Si : C = 11.2 : 1 : 7. The well-mixed chemicals were pressed into pellets (ϕ 15 mm × 10 mm), heated at 2273 K for 2 h in inert gas atmosphere of Ar, followed by cooling to ambient temperature by cutting furnace power. The reaction product was an aggregate of transparent platelet crystals with size up to 100 μm × 100 μm × 5 μm. The vaporization of Al and Si would significantly occur when melting at 2273 K, hence the crystals were most probably formed by a vapor-phase growth process.

(2) Characterization

The crystals were finely ground to obtain powder specimen and subsequently introduced into a 0.5 mm diameter glass capillary tube of internal diameter approximately 0.3 mm. The XRPD intensities were collected on a diffractometer (X'Pert PRO MPD, PANalytical B.V., Almelo, The Netherlands) equipped with a high speed detector in Debye-Scherrer geometry using CuKα radiation (45kV, 40mA) in a 2θ range from 1.9962° to 131.9931° (the accuracy in 2θ of ±0.0001°). Other experimental conditions were: continuous scan, total of 15559 datapoints and total experimental time of 13.8 h. No preferred orientation could be seen in the diffraction pattern which was collected with the specimen rotating. We corrected the X-ray absorption using the μr value (μ: linear absorption coefficient; r: sample radius) of the sample and capillary tube, which was determined by the transmittance of direct incident beam. The structure data were standardized using the computer program STRUCTURE TIDY [17]. The crystal-structure models were visualized with the computer program VESTA [18].

The crushed fracture fragments were dispersed with air and deposited on a holey carbon film attached to a copper grid. They were examined using a transmission electron microscope (JEM 3000F, JEOL ltd., Tokyo, Japan) operated at 300 kV and equipped with an energy dispersive X-ray analyzer (EDX; VOYAGER III, NORAN Instruments, Middleton, WI, USA). Selected area electron diffraction (SAED) patterns and corresponding lattice images were obtained. A chemical analysis was made for

nine crystal fragments to confirm the existence of O atoms within the crystal lattice as well as to quantitatively determine the atom ratios Al : Si. The correction was made by the ZAF routines.

3.4.3 Results and Discussion

(1) Crystal system, unit cell and chemical composition

Peak positions of the powder diffraction pattern were first determined using the computer program PowderX [19]. The 2θ values of 20 observed peak positions within $2.0° \leq 2\theta \leq 65.1°$ were then used as input data to the automatic indexing computer program TREOR90 [20]. A hexagonal unit cell was found with satisfactory figures of merit $M_{20}/F_{20} = 54/37(0.016042, 34)$ [21,22]. The derived unit-cell dimensions of $a = 0.33180(3)$ nm and $c = 1.9270(3)$ nm were subsequently used as initial parameters for the Le Bail method [23] using the computer program RIETAN-FP [24] in a wider 2θ range from $2.0°$ to $131.9°$. However, the refinement was unsuccessful with relatively large reliability indices [25] of $R_{wp} = 5.97\%$ ($S = R_{wp}/R_e = 1.60$) and $R_p = 4.20\%$.

In subsequent Le Bail analysis, we assumed the crystal system to be monoclinic. The orthorhombic system is hardly expected for the crystal structure because it requires twofold axes in three mutually perpendicular directions. The initial unit-cell dimensions used were $a = 0.57469$ nm, b ($= a/\sqrt{3}$) $= 0.33180$ nm, $c = 1.9270$ nm and $\beta = 90.0°$, which are comparable to those of the C-lattice orthohexagonal cell of the former hexagonal cell. The Le Bail analysis yielded much lower reliability indices of $R_{wp} = 4.17\%$ ($S = 1.13$) and $R_p = 3.06\%$. The refined unit-cell dimensions of $a = 0.57404(1)$ nm, $b = 0.331459(5)$ nm, $c = 1.92415(1)$ nm and $\beta = 90.033(1)°$ could successfully index all the observed reflections in the experimental diffraction pattern. The observed diffraction peaks were examined to determine the presence or absence of reflections. Systematic absences $h + k \neq 2n$ for hkl, $h \neq 2n$ for $h0l$ and $k \neq 2n$ for $0k0$ reflections were found, which implies that possible space groups are $C2$, Cm and $C2/m$.

The SAED pattern and corresponding lattice image (Fig. 3-10) indicate that the crystal is characterized by a layered structure with the periodicity of about 2 nm along the c axis. The EDX spectrum showed the existence of a small amount of O atoms within the crystal lattice (Fig. 3-11). The O atoms might be originated from the impurities of Ar gas and introduced into the sample during the crystal growth process. The atom ratios Al : Si were determined to be $0.932(3) : 0.068(3)$, where the numbers in parentheses indicate standard deviations. Accordingly, the present specimen must be a new compound which has been discovered for the first time in the Al-Si-O-C system. The unit cell was pseudohexagonal and compatible with that of Al_8SiC_7 ($V = 0.18287$ nm^3 and $Z = 1$) [7]. Because the unit-cell content of this compound is [8Al 1Si 7C] (Al + Si = 9), that of the new one ($V = 0.36611$ nm^3) must be [16.77Al 1.23Si 14(O+C)] (Al : Si = 0.932 : 0.068, Al + Si = 18), assuming that the O atoms exclusively occupy the C sites.

(2) Initial structural model

Because the atomic scattering factors for Al and Si are almost the same and the oxygen concentration is relatively low, we used a unit-cell content with [18Al 14C] as input data for the search of a crystal-structure model. All of the possible space groups were tested using the EXPO2004 package [13] for crystal structure determination. A promising structural model with a minimum reliability index R_F of 7.88% was found with the space group $C2/m$ (centrosymmetric) in a default run of the program. There were nine independent sites in the unit cell; five Al/Si sites (Al/Si1, Al/Si2, Al/Si3, Al/Si4 and Al/Si5) and three O/C sites (O/C1, O/C2 and O/C3) were located at the Wyckoff position $4i$, and one O/C site (O/C4) was located at $2b$. The unit-cell content of this structural model

was found to be [20Al 14C], suggesting that one of the site occupancies (g) of Al/Si sites should be reduced to one-half its initial value. The Al/Si1 sites were unusually close to each other with the distance of 0.189 nm, hence the g(Al/Si1)-value was reduced to 1/2. This implies that the crystal is twinned, the twin domains of which are related by a pseudo-symmetry inversion. The twinning structure of this compound will be discussed in more detail for the final structural model.

The structural parameters and unit-cell dimensions were refined by the Rietveld method using the computer program RIETAN-FP [24]. The chemical species (oxidation states) of Al, Si, O and C were adopted in the Rietveld analysis. A Legendre polynomial was fitted to background intensities with twelve adjustable parameters. The pseudo-Voigt function [26] was used to fit the peak profile. The occupancies of O and C atoms in each O/C site were refined without any constraints. The isotropic displacement (B) parameters for O and C atoms were constrained to be equal. Because the g and corresponding B parameters were strongly correlated, they were refined alternately in successive least-squares cycles. The O atoms preferentially occupied the O/C1 and O/C2 sites, the g(O)-values of which were 0.52(2) and 0.30(1), respectively. Because of the absence of O atoms at both O/C3 and O/C4 sites, they were relabeled C2 and C1, respectively. The refinement, however, resulted in unsatisfactory large R indices of R_{wp} = 4.86% (S = 1.32), R_p = 3.53%, R_B = 4.21% and R_F = 3.13%.

We expected MPF to enable us to extract structural details that had not been introduced into the initial structural model. After three REMEDY cycles, R_{wp}, S, R_p, R_B and R_F significantly decreased to 4.44%, 1.20, 3.23%, 0.94% and 1.07%, respectively. The decreases in R indices demonstrate that the crystal structure can be seen more clearly from EDD instead of from the conventional structural parameters. In order to disclose the subtle EDD changes induced by MPF, we obtained the difference in EDD before and after the REMEDY cycles. The two-dimensional difference map at y = 0 showed two positive peaks with the heights of 0.006 nm^{-3} and 0.0045 nm^{-3} [Fig. 3-12(a)]. These peaks were located at 0.003 nm apart from the Al/Si2 site for the former and 0.002 nm apart from the Al/Si5 site for the latter. On the other hand, the residual electron densities were negligibly low at the O/C1 and O/C2 sites, indicating that the O and C atoms definitely occupy the same sites in the crystal structure. These findings promoted us to build split-atom models for Al/Si2 and Al/Si5.

(3) Split-atom model

In the split-atom model, each of the Al/Si2 and Al/Si5 sites at 4i was split into two independent crystallographic sites MA and MB (M = Al/Si2 and Al/Si5). We first refined the occupancies under the linear constrains of g(MA)+g(MB) = 1 to find that all of the g parameters eventually converged to values very close to 0.5. Thus, we have fixed these parameters equal to 0.5 in successive least-squares cycles. The parameters B(MA) and B(MB) were constrained to be equal to each other. The final Rietveld refinement resulted in satisfactory R indices of R_{wp} = 4.45% (S = 1.21), R_p = 3.30%, R_B = 3.47% and R_F = 2.53%, indicating that the disordered arrangements of Al/Si2 and Al/Si5 sites can be represented adequately with the split-atom model in Fig. 3-13. The individual separation distances are 0.035(1) nm for (Al/Si2A)-(Al/Si2B) and 0.022(1) nm for (Al/Si5A)-(Al/Si5B). Crystal data are given in Table 3-13, and the final atomic positional and B parameters are given in Table 3-14. The chemical composition was found to be $Al_{16.77(5)}Si_{1.23(5)}O_{3.04(9)}C_{10.96(9)}$, with the chemical formula of $[Al_{16.8}Si_{1.2}]_{\Sigma18}[O_{3.0}C_{11.0}]_{\Sigma14}$ (space group $C2/m$, Z = 1).

We used the MPF method again and subsequently obtained the difference in EDD before and after the REMEDY cycles to confirm the validity of the split-atom model. After two REMEDY cycles, R_{wp}, S, R_p, R_B and R_F further decreased to 4.20%, 1.14, 3.09%, 0.92% and 1.05%, respectively. The decreases in R indices indicate that the present disordered structure is better expressed with electron

densities than with the structural parameters in Table 3-14. Observed, calculated, and difference XRPD patterns for the final MPF are plotted in Fig. 3-14. The two-dimensional difference map at $y = 0$ [Fig. 3-12(b)] gave much lower residual electron densities, indicating that the EDD determined by the final MPF is explained sufficiently by the present split-atom model. For example, the three-dimensional electron-density images at the Al/Si2 and Al/Si5 sites (Fig. 3-15) show broadening, the equidensity isosurfaces of which are in reasonably good agreement with the atom arrangements. We therefore concluded that, as long as the crystal structure was expressed by a structural model, the present split-atom model would be satisfactory.

(4) Structure description

The disordered structure can be regarded as a statistical average of the two twin-related structural configurations with the low-symmetry subgroup Cm (Fig. 3-16). When the twofold axes parallel to [010] are removed from the space group $C2/m$, the resulting space group is Cm, with a center of symmetry being lost concomitantly. The two structural configurations as shown in Fig. 3-16 are therefore related not only by a pseudo-symmetry twofold rotation but also by a pseudo-symmetry inversion. Thus, the crystal must be an inversion twin. Actually, we observed using TEM the lattice defects parallel to (001), which must correspond to the inversion twin boundaries (Fig. 3-17). The distance between the adjacent boundaries (*i.e.*, twin width) ranged from 36 nm to 49 nm with the average distance of 42.7 nm [(43+36+49)/3 = L]. Accordingly, the individual twin domains contained on the average about 22 (= $L/d_{(001)}$) unit cell along the direction perpendicular to (001). The dimensions of twin domains would be within the coherence range of X-rays, and hence the crystal structure has been satisfactorily represented by the split-atom model. One of the two orientational twin domain contained the Al/Si2A and Al/Si5B sites, and the other involved the Al/Si2B and Al/Si5A sites (Fig. 3-16). Because the occupancies of these sites as well as that of Al/Si1 site were all equal to 0.5, the actual domain ratio should be almost 0.5 : 0.5. This twin structure is most probably originated during crystal growth.

The atomic configurations are shown for $[Al_{16.8}Si_{1.2}][O_{3.0}C_{11.0}]$, Al_4C_3, Al_4SiC_4 and $Al_4Si_2C_5$ (Fig. 3-18). The crystal structure of $[Al_{16.8}Si_{1.2}][O_{3.0}C_{11.0}]$ can be regarded as a layered structure, which consists of A-type $[(Al,Si)_4(O,C)_4]$ unit layer and B-type $[(Al,Si)(O,C)_2]$ single layer with stacking sequence of <*ABA*> along the c axis. In Table 3-15, only (Al,Si)–(O,C) bonds belonging to one of the two twin-related orientations are reported, excluding possible bonds between atoms of different orientation states. The Al and Si atoms are tetrahedrally coordinated by O and/or C atoms with the mean (Al,Si)-(O,C) distance of 0.205 nm, which is comparable to the mean (Al,Si)-C distances of the $[(Al,Si)C_4]$ polyhedra in Al_4C_3 (0.206 nm), Al_4SiC_4 (0.202 nm) and $Al_4Si_2C_5$ (0.201 nm). Because the mean interatomic distance of $[Al_{16.8}Si_{1.2}][O_{3.0}C_{11.0}]$ compares well with those of Al_4C_3, Al_4SiC_4 and $Al_4Si_2C_5$, and also these structures are closely related to one another as shown in Fig. 3-18, $[Al_{16.8}Si_{1.2}][O_{3.0}C_{11.0}]$ can be regarded as, from a structural point of view, a carbide solid solution in which a relatively small amount of O atoms was dissolved into the C sites rather than an oxycarbide compound. The general formula of the solid solution is expressed by $[Al_{18-x}Si_x][O_yC_{14-y}]$, where x- and y-values are, respectively, 1.2 and 3.0 for the sample. One of the possible end member is Al_8SiC_7 ($x = 2$ and $y = 0$), which could be composed of a hexagonal layered structure with stacking sequence of <*ABA*>.

A series of carbides in the Al_4C_3-SiC system can be represented by a general formula $Al_4C_3(SiC)_X$, where $X = 0$ (Al_4C_3), 1/2 (Al_8SiC_7), 1 (Al_4SiC_4), 2 ($Al_4Si_2C_5$), 3 ($Al_4Si_3C_6$) and 4 ($Al_4Si_4C_7$). With $0 \le X \le 2$, the fraction of A layer (f_A) with respect to the B layer in the crystal structure steadily decreased with increasing X-value; the f_A and X values are well correlated by the

equation $f_A = 1/(1+X)$. The f_A-values as predicted by this relationship are 0.25 for $Al_4Si_3C_6$ ($X = 3$) and 0.2 for $Al_4Si_4C_7$ ($X = 4$). Assuming that these crystal structures were also made up of the two types of layers A and B, the minimum stacking sequence would be $BABB$ for $Al_4Si_3C_6$ and $BBABB$ for $Al_4Si_4C_7$. These structures are comparable to those proposed by Oscroft $et\ al.$ [1].

3.4.4 Conclusion

We have for the first time discovered a quaternary compound in the Al-Si-O-C system. The crystal structure was successfully determined from XRPD data and described in relation to those of the layered carbides Al_4C_3, Al_4SiC_4 and $Al_4Si_2C_5$. The compound was, from a structural point of view, regarded as a carbide solid solution rather than an oxycarbide compound. The crystal was most probably an inversion twin with an almost 0.5 : 0.5 domain ratio.

References

[1] R. J. Oscroft, P. Korgul, D. P. Thompson, *British Ceramic Proceedings* **42**, 33-47 (1989).

[2] G. A. Jefeerey, V. Y. Wu, *Acta Crystallogr.* **20**, 538-547 (1966).

[3] Th. M. Gesing and W. Jeitschko, *Z. Naturforsch.* **50b**, 196-200 (1995).

[4] V. J. Barczak, *J. Am. Ceram. Soc.* **44**, 299 (1961).

[5] Z. Inoue, Y. Inomata, H. Tanaka, H. Kawabata, *J. Mater. Sci.* **15**, 575-580 (1980).

[6] J. Schoennahl, B. Willer, M. J. Daire, *Solid State Chem.* **52**, 163-173 (1984).

[7] B. L. Kidwell, L. L. Oden, R. A. McCune, *J. Appl. Crystallogr.* **17**, 481-482 (1984).

[8] L. M. Foster, G. Long, M. S. Hunter, *J. Am. Ceram. Soc.* **39**, 1-11 (1956).

[9] E. L. Amma, G. A. Jeffrey, *J. Chem. Phy.* **34**, 252-259 (1961).

[10] V. E. Grass, Yu. I. Ryabkov, B. A. Goldin, P. A. Sitnikov, *J. Struct. Chem.* **45**, 100-106 (2004).

[11] L. M. Foster, G. Long, M. S. Hunter, *J. Am. Ceram. Soc.* **39**, 1-11 (1956).

[12] G. A. Jefeerey, M. Slaughter, *Acta Crystallogr.* **16**, 177-184 (1963).

[13] A. Altomare, M. C. Burla, M. Camalli, B. Carrozzini, G. L. Cascarano, C. Giacovazzo, A. Guagliardi, A. G. G. Moliterni, G. Polidori, R. Rizzi, *J. Appl. Crystallogr.* **32**, 339-340 (1999).

[14] H. M. Rietveld, *J. Appl. Crystallogr.* **2**, 65-71 (1969).

[15] M. Takata, E. Nishibori, M. Sakata, *Z. Kristallogr.* **216**, 71-86 (2001).

[16] F. Izumi, S. Kumazawa, T. Ikeda, W.-Z. Hu, A. Yamamoto, K. Oikawa, *Mater. Sci. Forum* **378-381**, 59-64 (2001).

[17] L. M. Gelato, E. Parthé, *J. Appl. Crystallogr.* **20**, 139-143 (1987).

[18] K. Momma, F. Izumi, *J. Appl. Crystallogr.* **41**, 653-658 (2008).

[19] C. Dong, *J. Appl. Crystallogr.* **32**, 838 (1999).

[20] P. E. Werner, L. Eriksson, M. Westdahl, *J. Appl. Crystallogr.* **18**, 367-370 (1985).

[21] P. M. de Wolff, *J. Appl. Crystallogr.* **1**, 108-113 (1968).

[22] G. S. Smith, R. L. Snyder, *J. Appl. Crystallogr.* **12**, 60-65 (1979).

[23] A. Le Bail, H. Duroy, J. L. Fourquet, *Mater. Res. Bull.* **23**, 447-452 (1988).

[24] F. Izumi and T. Ikeda, *Mater. Sci. Forum* **321-324**, 198-203 (2000).

[25] R. A. Young, in: R. A. Young (Ed.), The Rietveld Method, Oxford University Press, Oxford, U.K., 1993, pp. 1-38.

[26] H. Toraya, *J. Appl. Crystallogr.* **23**, 485-491 (1990).

Table 3-13. Crystal data for $[Al_{16.8}Si_{1.2}][O_{3.0}C_{11.0}]$

Chemical composition	$Al_{16.77(5)}Si_{1.23(5)}O_{3.04(9)}C_{10.96(9)}$
Space group	$C2/m$
a/nm	0.57404(1)
b/nm	0.331435(5)
c/nm	1.92410(2)
β/°	90.036(1)
V/nm³	0.366076(9)
Z	1
D_x/Mgm⁻³	3.027

Table 3-14. Structural Parameters for $[Al_{16.8}Si_{1.2}][O_{3.0}C_{11.0}]^{a}$

Site	Wyckoff position	g	x	y	z	$100 \times B$/nm²
Al/Si1	$4i$	0.5	0.153(1)	0	0.5193(1)	0.13(7)
Al/Si2A	$4i$	0.5	0.157(2)	0	0.2768(2)	0.25(6)
Al/Si2B	$4i$	0.5	0.172(2)	0	0.2591(1)	0.25
Al/Si3	$4i$	1	0.168(1)	0	0.0512(1)	0.86(4)
Al/Si4	$4i$	1	0.5018(8)	0	0.17189(6)	0.80(3)
Al/Si5A	$4i$	0.5	0.502(2)	0	0.3784(2)	0.46(4)
Al/Si5B	$4i$	0.5	0.504(3)	0	0.3897(2)	0.46
C1	$2b$	1	0	1/2	0	0.72(7)
C2	$4i$	1	0.188(2)	0	0.1506(2)	0.72
O/C1	$4i$	1	0.127(1)	0	0.4215(1)	0.72
O/C2	$4i$	1	0.525(1)	0	0.2842(1)	0.72

^{a} Site occupancies: O/C1: 48.6(14)% C and 51.4(14)% O; O/C2: 75.3(9)% C and 24.7(9)% O

Table 3-15. Interatomic Distances (nm) in $[Al_{16.8}Si_{1.2}][O_{3.0}C_{11.0}]$

```
--------------------------------------------------
```

Al/Si1-O/C1	0.1889(4)
Al/Si1-O/C1	0.1973(8)
Al/Si1-O/C1	0.2373(5)×2
<Al/Si1-O/C>	0.215
Al/Si2A-O/C2	0.1828(9)×2
Al/Si2A-O/C2	0.212(2)
Al/Si2A-C2	0.2435(6)
<Al/Si2A-O/C>	0.205
Al/Si2B-O/C2	0.1921(7)×2
Al/Si2B-O/C2	0.208(1)
Al/Si2B-C2	0.2091(7)
<Al/Si2B-O/C>	0.200
Al/Si3-C2	0.1914(5)
Al/Si3-C1	0.2147(5)
Al/Si3-C1	0.2155(3)×2
<Al/Si3-C>	0.209
Al/Si4-C2	0.185(1)
Al/Si4-C2	0.2015(8)×2
Al/Si4-O/C2	0.2165(4)
<Al/Si4-O/C>	0.201
Al/Si5A-O/C2	0.1817(6)
Al/Si5A-O/C1	0.1988(7)×2
Al/Si5A-O/C1	0.230(2)
<Al/Si5A-O/C>	0.202
Al/Si5B-O/C1	0.1902(8)×2
Al/Si5B-O/C2	0.2033(7)
Al/Si5B-O/C1	0.225(2)
<Al/Si5B-O/C>	0.202

```
--------------------------------------------------
```
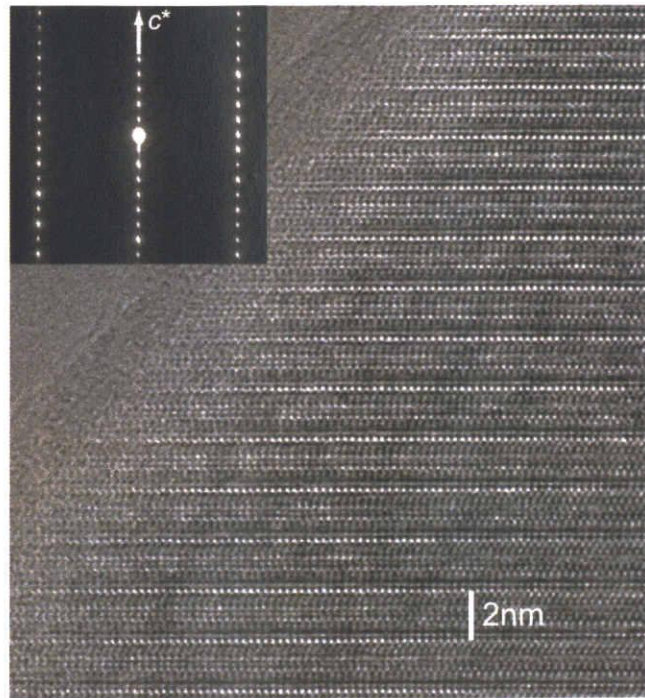
Fig.3-10. Selected-area electron diffraction pattern and corresponding lattice image. Incident beam parallel to (001) plane.
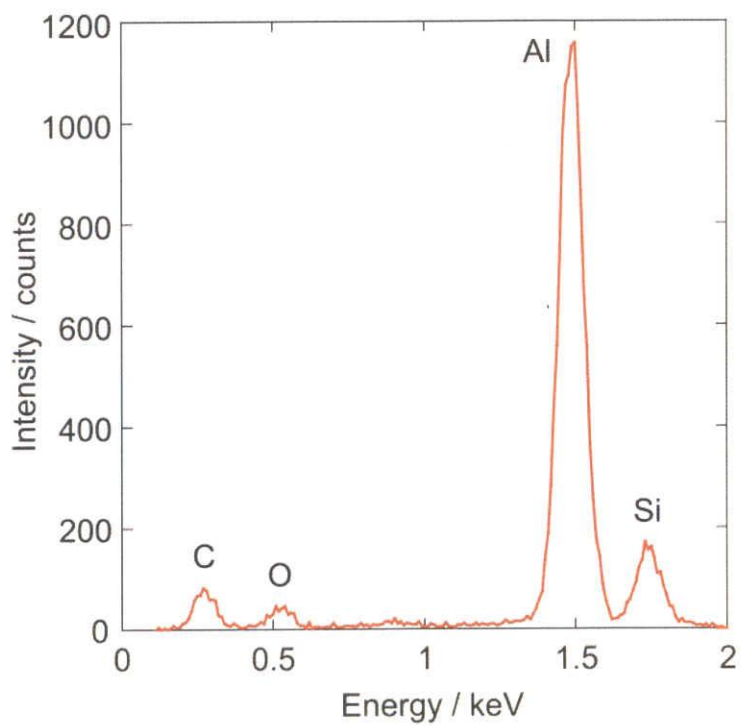
Fig.3-11. Identification of the presence of Al, Si, O and C in the compound. EDX spectrum.
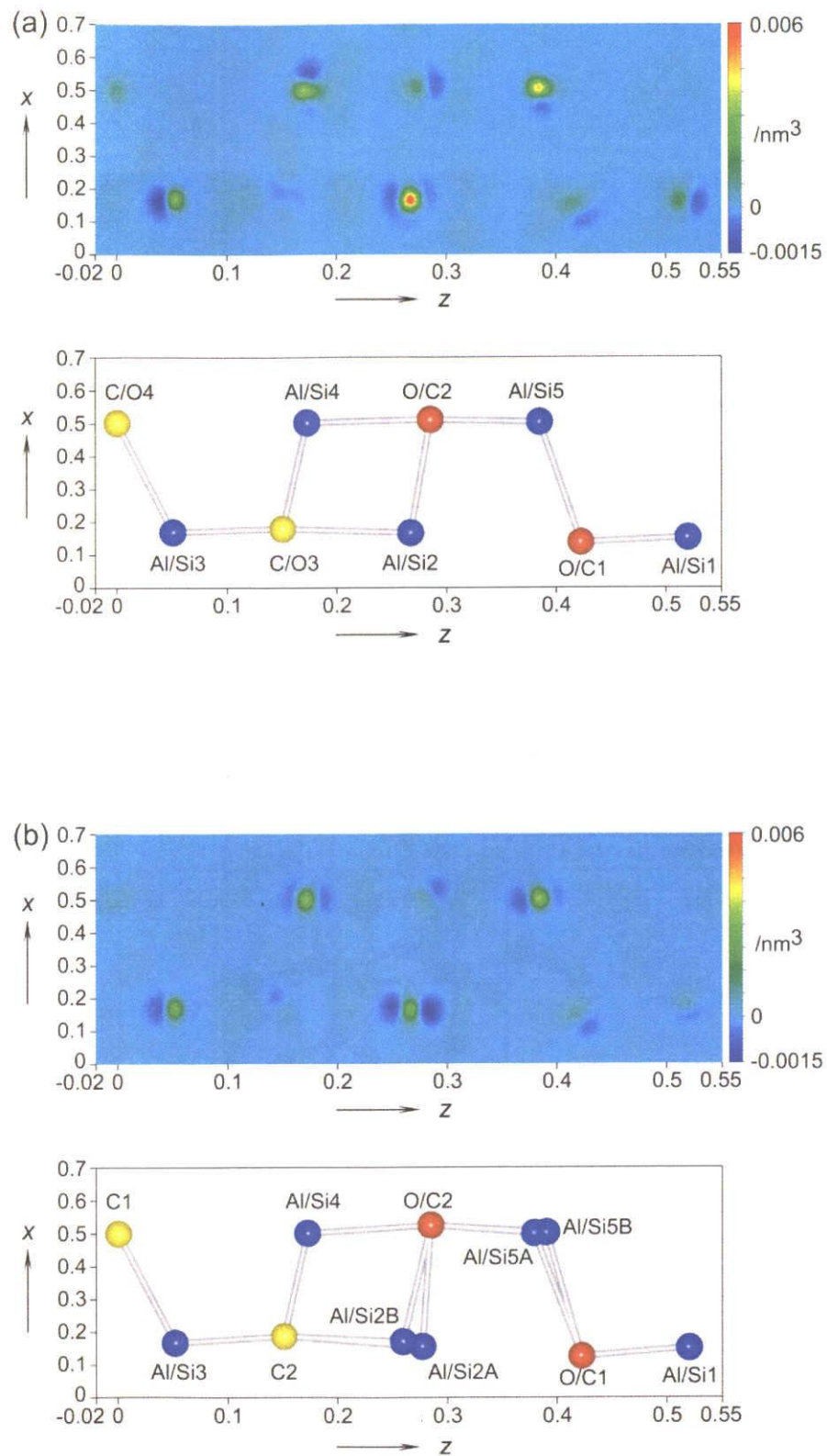
Fig.3-12. Sections of electron-density-distribution difference with the plane $0 \leq x \leq 0.7$, $y = 0$, $-0.02 \leq z \leq 0.55$ (upper part), and the corresponding atomic configurations (lower part). (a) The initial model and (b) the split-atom model.
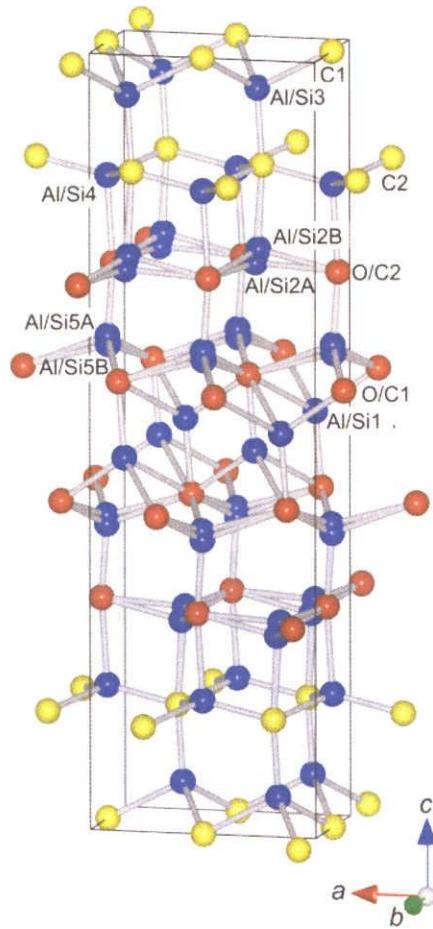
Fig.3-13. Crystal structure of $[Al_{16.8}Si_{1.2}][O_{3.0}C_{11.0}]$. Space group $C2/m$.
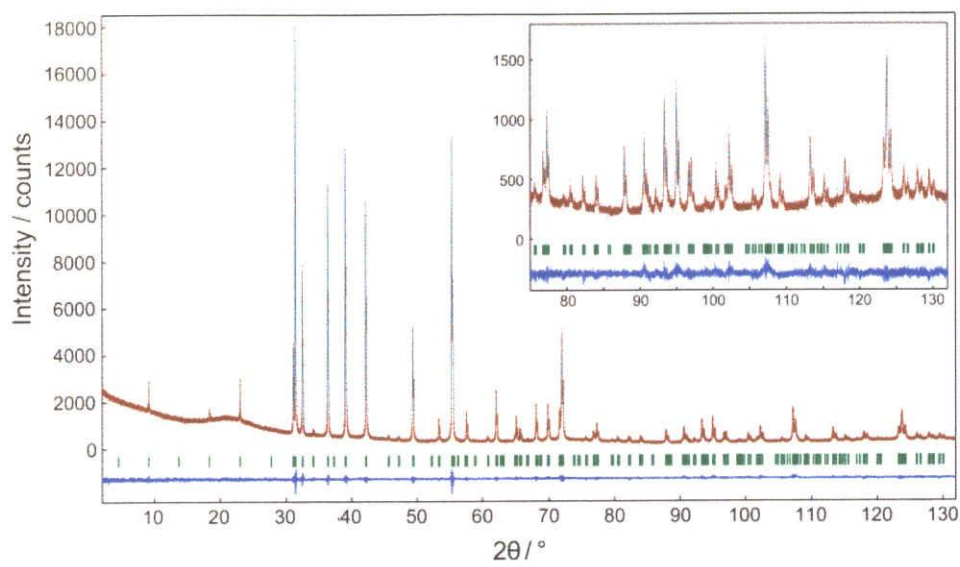
Fig. 3-14. Comparison of the observed diffraction pattern of $[Al_{16.8}Si_{1.2}][O_{3.0}C_{11.0}]$ (symbol: +) with the corresponding calculated pattern (upper solid line). The difference curve is shown in the lower part of the diagram. Vertical bars indicate the positions of Bragg reflections.
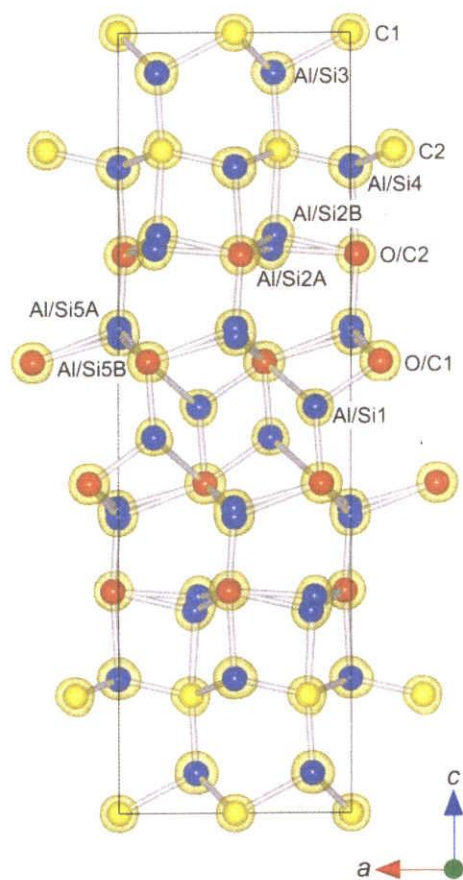
Fig. 3-15. Three-dimensional electron density distribution determined by MPF with the split-atom model viewed along the b axis. Isosurfaces expressed in wireframe style for an equidensity level of 0.002 nm^{-3}.
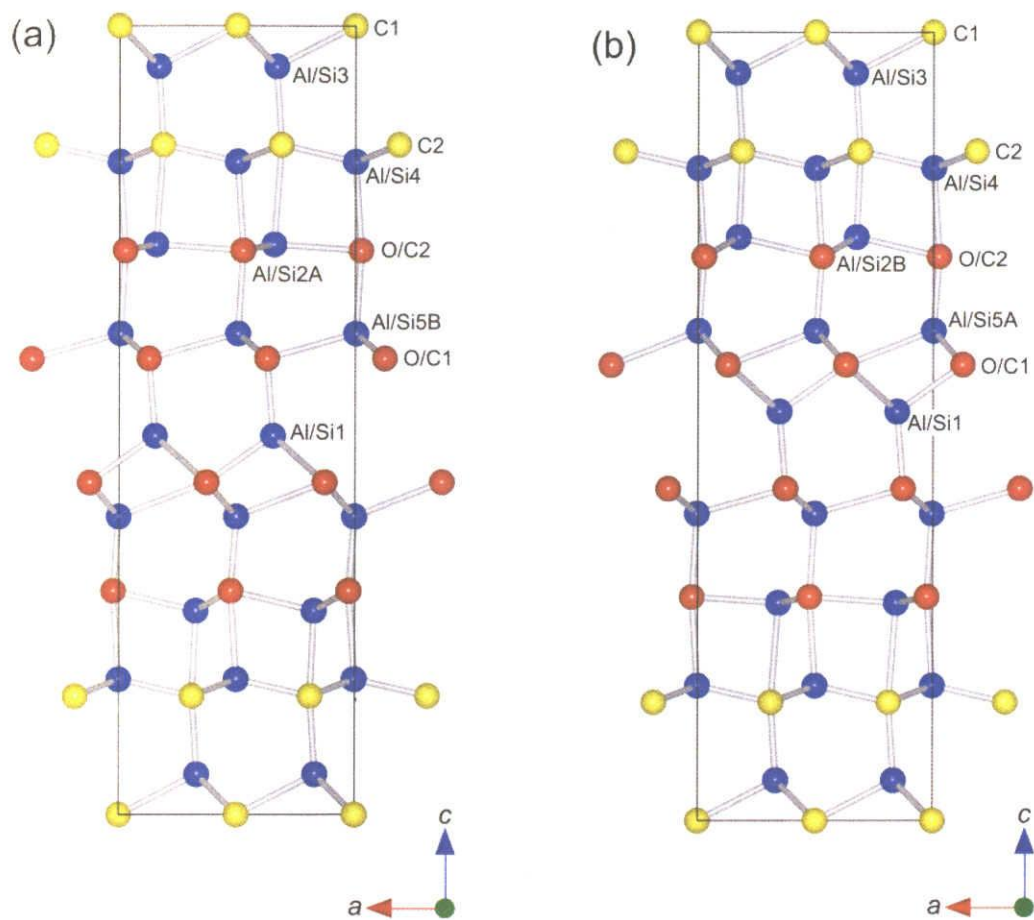
Fig. 3-16. Crystal structures of the two orientation states of $[Al_{16.8}Si_{1.2}][O_{3.0}C_{11.0}]$ viewed along the b axes. Space group Cm. The two structural configurations (a) and (b) are related by the pseudo-symmetry inversion.
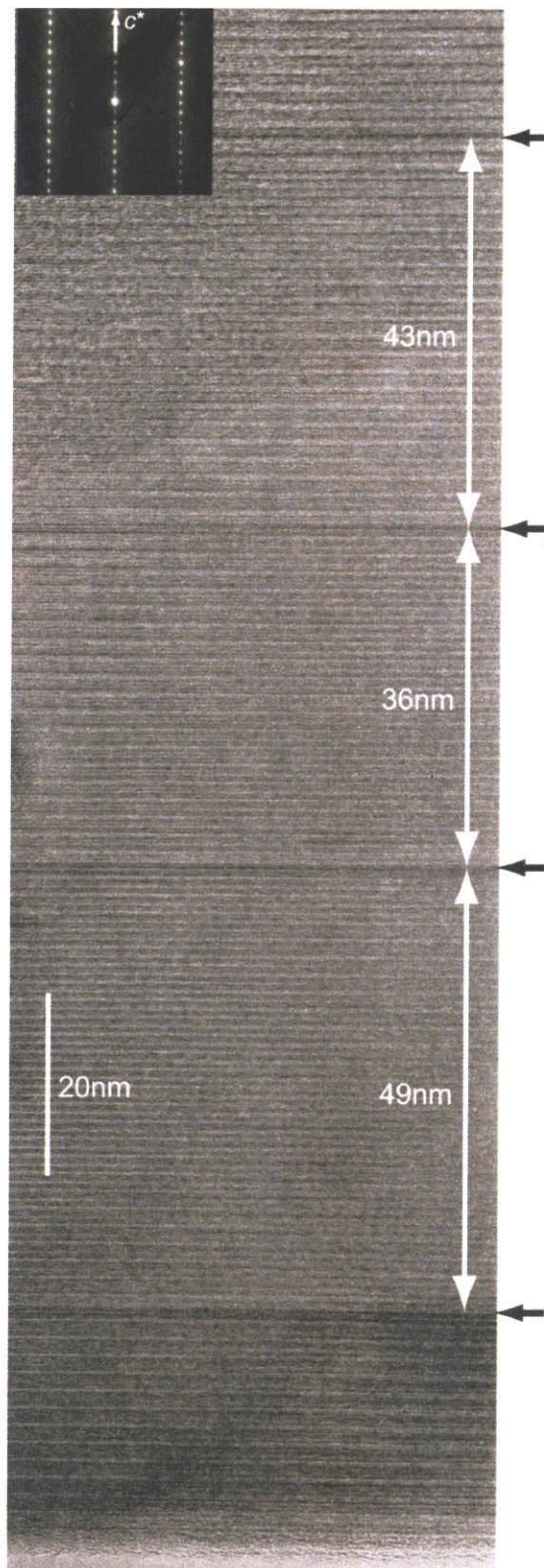
Fig. 3-17. Lattice image showing plane defects (indicated by arrows) perpendicular to [001]. The defects most probably correspond to the inversion twin boundaries.
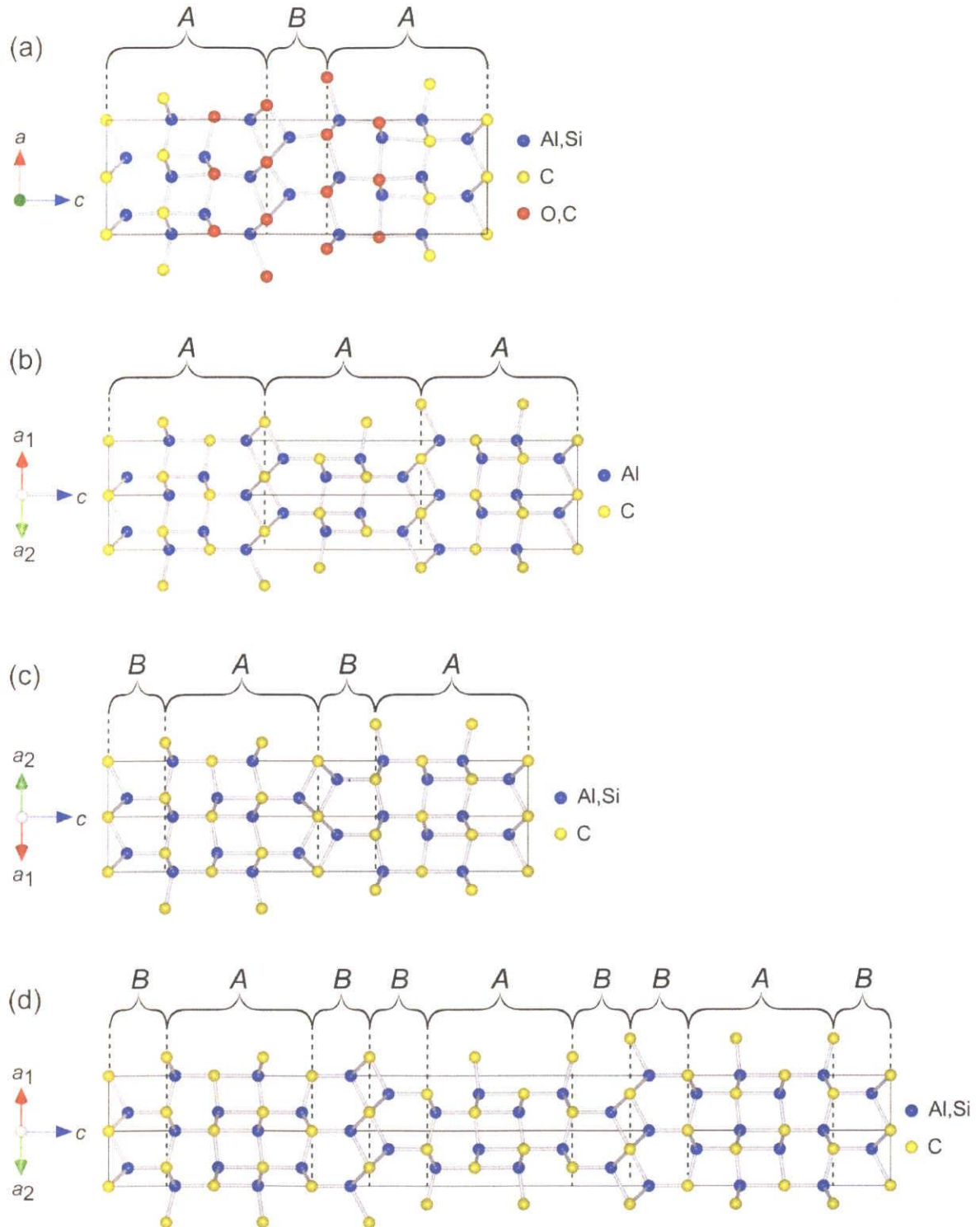
Fig. 3-18. Atomic configurations in (a) $[Al_{16.8}Si_{1.2}][O_{3.0}C_{11.0}]$, (b) Al_4C_3, (c) Al_4SiC_4 and (d) $Al_4Si_2C_5$, showing the crystal structures being made up of two types of layers A and B. The unit cells are represented by solid lines.

3.5 Thermoelectric properties of the layered carbides

3.5.1 Introduction

Thermoelectric materials with high efficiency of energy conversion are of interest for applications as heat pumps and power generators. Low-dimensional materials that consist of, for example, conducting two-dimensional (2D) layers are promising for thermoelectric energy conversion [1−6]. The advantage of the low dimensionality can be interpreted in terms of the carrier confinement effect in the 2D layers, which leads to an enlarged absolute value of the Seebeck coefficient (S) compared to the materials with threedimensional conducting paths. In addition, the 2D layered materials are expected to have relatively low thermal conductivity (κ) due to phonon scattering at layer interfaces. Hence, materials with layered nanostructures could show high performance of thermoelectricity, which is quantified by a figure of merit $S^2\sigma/\kappa$, where s is electrical conductivity. Since the crystal structure of the layered carbides, $(ZrC)_l Al_3 C_2$ (l = 2 and 3) and $(ZrC)_m[Al_{0.89}Si_{0.11}]_4 C_2$ (m = 2 and 3), are composed of the electroconductive NaCl-type layers separated by the less electroconductive $Al_4 C_3$-type layers [7-10], it was expected to show good thermoelectric properties.

In the present study, we have characterized thermoelectric properties of $(ZrC)_l Al_3 C_2$ (l = 2 and 3) and $(ZrC)_m[Al_{0.89}Si_{0.11}]_4 C_2$ (m = 2 and 3).

3.5.2 Syntheses of the layered carbides

Two types of sintered specimens of $(ZrC)_2 Al_3 C_2$ (sample S-A) and $(ZrC)_3 Al_3 C_2$ (S-B) were individually prepared from the reagent-grade chemicals of ZrC (99.9%, KCL Co., Ltd., Saitama, Japan), Al (KCL, 99.9%) and C (graphite, KCL, 99.9%). Each of the stoichiometric mixtures was first heated in vacuum at 1653K for 1 h to obtain polycrystalline materials. The sintering conditions to prepare the dense bodies were identical to those described above. Their closed porosities were found to be about 99% for both samples.

The reagent-grade chemicals of ZrC, $Al_4 C_3$ and SiC were mixed in two different molar ratios of $[ZrC:Al_4 C_3:SiC]$ = [9:4:2] for $(ZrC)_2[Al_{0.89}Si_{0.11}]_4 C_3$ (S-C) and [7:2:1] for $(ZrC)_3[Al_{0.89}Si_{0.11}]_4 C_3$ (S-D). Each of the well-mixed chemicals was pressed into pellets (ø 13 mm × 10 mm), heated at 1973 K for S-C and 1873 K for S-D in vacuum, followed by cooling to ambient temperature by cutting the furnace power. Reaction products were slightly sintered polycrystalline materials. They were finely ground to obtain powder specimens.

In order to obtain a dense sample, the powder specimen was subsequently sintered by a pulse electric current sintering method (SPS-1030, Sumitomo Coal Mining). The sintering was conducted at a uniaxial pressure of about 40MPa and at 1973K for 5 min in vacuum. Dense sintered bodies in the form of discs (15mm diameter and 5mm long) were thus obtained. Its closed porosity was found to be about 99%.

3.5.3 Characterization

Samples in the form of rectangular bars (13 mm × 4 mm × 3 mm) were cut from the discs using a diamond saw for thermoelectric measurements. The X-ray diffraction intensities from the cut surface have revealed that the sintered samples, consisting exclusively of the desired phases, were free from preferred orientation of the crystal grains. The thermoelectric properties were evaluated by the power factor, which is determined from electrical conductivity (σ) and Seebeck coefficient (S) as $S^2\sigma$. The svalues and thermoelectromotive force (TF) were simultaneously measured between 373 and 1273K in vacuum using a thermoelectric property measurement system (RZ2001i, Ozawa Science). It generated a temperature gradient in the specimen by passing cool air in a silica glass tube that is placed

near one end of the specimen. The TF-values were measured as a function of temperature difference (ΔT) between the two ends. The S-values were calculated from the slopes of the linear plots of TF against ΔT.

3.5.4 Thermoelectric properties

The temperature dependences of σ, S, and power-factor values of the sintered specimen, together with those of $(ZrC)_2[Al_{0.89}Si_{0.11}]_4C_3$, $(ZrC)_2Al_3C_2$ and $(ZrC)_3Al_3C_2$, are shown in Fig. 3-19. Because the sample S-D was composed mainly of $(ZrC)_3[Al_{0.89}Si_{0.11}]_4C_3$ with a small amount of ZrC (9.3 mol%), the continuous conduction pass in the sintered specimen would be exclusively formed by the former. The material in the sample that shows thermoelectricity is $(ZrC)_3[Al_{0.89}Si_{0.11}]_4C_3$. Accordingly, the electric and thermoelectric properties of the sintered specimen (S-D) are principally attributable to the constituent $(ZrC)_3[Al_{0.89}Si_{0.11}]_4C_3$ compound.

The σ values of the four types of layered carbides steadily decreased with increasing temperature, representing a conductor-type behabior (Fig. 3-19(a)). When the carbides were compared at the same temperature, $(ZrC)_3Al_3C_2$ ($l = 3$) always showed the largest σ value, followed by $(ZrC)_3[Al_{0.89}Si_{0.11}]_4C_3$ ($m = 3$). These values were necessarily larger than those of both carbides with $l = 2$ and $m = 2$, and hence the intergrowth structure with the thicker ZrC layer seems to be more advantageous for conduction of electricity.

The signs of S were always negative for all the samples, indicating a predominance of negative mobile charge carriers (Fig. 3-19(b)). With $(ZrC)_2[Al_{0.89}Si_{0.11}]_4C_3$, the absolute value of S was the largest among the four materials, regardless of temperature, and steadily increased with increasing temperature from 373 to 1073 K. A comparison of the S values between $(ZrC)_m[Al_{0.89}Si_{0.11}]_4C_3$ ($m = 2$ and 3) and $(ZrC)_lAl_3C_2$ ($l = 2$ and 3) suggest that the intergrowth structure with the thicker Al_4C_3-type layer would be more favorable for thermoelectric power generation.

The power-factor value of $(ZrC)_2[Al_{0.89}Si_{0.11}]_4C_3$ was the largest among the four materials, throughout the temperature region measured, with the maximal power-factor value of 7.6×10^{-5} W $m^{-1}K^{-2}$ at 373 K (Fig. 3-19(c)). The power-factor values of the homologous compounds $(ZrC)_m[Al_{0.89}Si_{0.11}]_4C_3$ ($m = 2$ and 3) were almost constant between 373 and 1073 K, while those of $(ZrC)_lAl_3C_2$ ($l = 2$ and 3) steadily decreased with increasing temperature. Since all the present sintered specimens were composed of randomly oriented polycrystals, the improvement of preferred orientation using the technique of ceramic processing or thin film preparation could further increase the electrical conductivity and consequently the power factor.

References

[1] L.D. Hicks, M.S. Dresselhaus, *Phys. Rev. B* **47** (1993) 12727–12731.

[2] L.D. Hicks, M.S. Dresselhaus, *Phys. Rev. B* **47** (1993) 16631–16634.

[3] L.D. Hicks, T.C. Harman, M.S. Dresselhaus, *Appl. Phys. Lett.* **63** (1993) 3230–3232.

[4] K. Koumoto, H. Koduka, W.-S. Seo, *J. Mater. Chem.* **11** (2001) 251–252.

[5] M. Yasukawa, K. Ikeuchi, T. Kono, K. Ueda, H. Hosono, *J. Appl. Phys.* **98** (2005) 013706/1–013706/4.

[6] T. Mori, T. Nishimura, *J. Solid State Chem.* **179** (2006) 2908–2915.

[7] K. Fukuda, S. Mori, S. Hashimoto, *J. Am. Ceram. Soc.* **88** (2005) 3528–3530.

[8] Th.M. Gesing, W. Jeitschko, *Z. Naturforsch.*, **50b** (1995) 196-200.

[9] K. Fukuda, M. Hisamura, T. Iwata, N. Tera and K. Sato, *J. Solid State Chem.*, **180** (2007) 1809-1815.

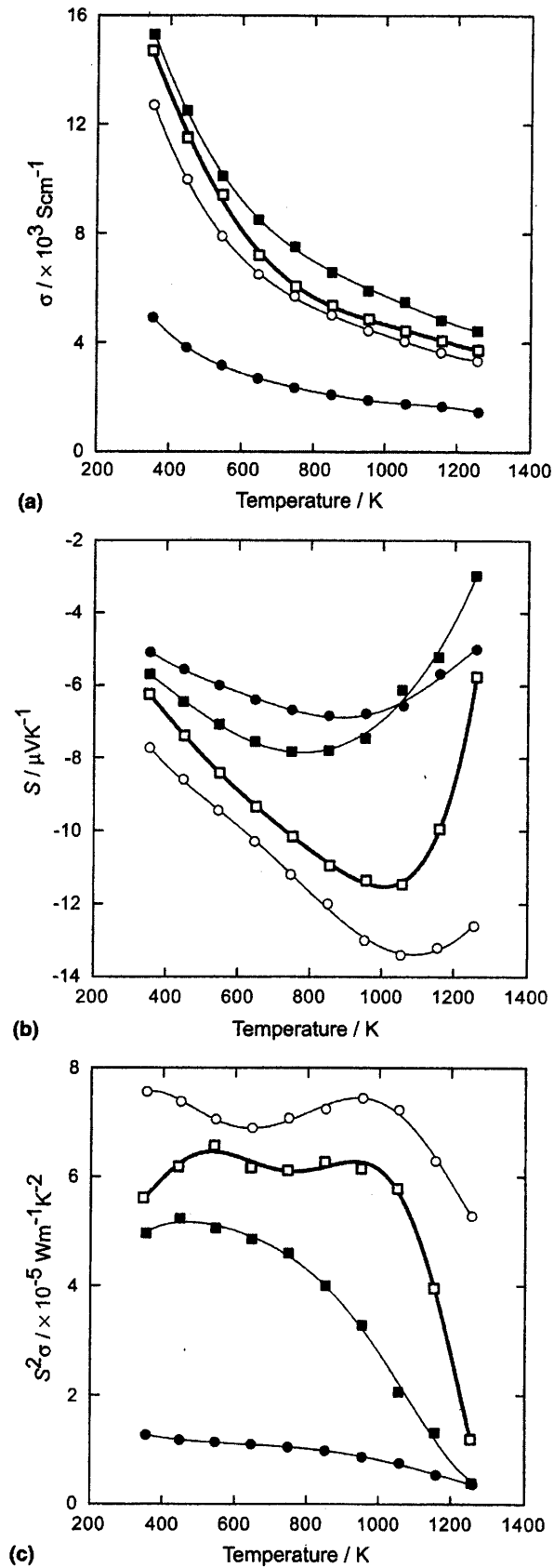[10] K. Fukuda, M. Hisamura, Y. Kawamoto and T. Iwata, *J. Mater. Res.*, **22** (2007) 2888-2894.

Fig. 3-19. Temperature dependences of (a) electirical conductivity σ, (b) Seebeck coefficient S, and (c) thermoelectric power factor $S^2\sigma$ for (○) $(ZrC)_2[Al_{3.56}Si_{0.44}]C_3$, (□) $(ZrC)_3[Al_{3.56}Si_{0.44}]C_3$, (●) $(ZrC)_2Al_3C_2$ and (■) $(ZrC)_3Al_3C_2$.

Chapter 4

Structural characterization of oxide-ion-conducting lanthanum silicates

4.1 Structural change of oxide-ion-conducting lanthanum silicate on heating from 295 to 1073 K

Abstract

Structural change of $La_{9.33}(SiO_4)_6O_2$ on heating from 295 to 1073 K was investigated by means of high-temperature laboratory X-ray powder diffraction ($CuK\alpha_1$). The apatite-type crystal structures (space group $P6_3/m$) were refined by the Rietveld method, with the anisotropic displacement parameters being assigned for all atoms. The validity of the structural models was verified by the three-dimensional electron density distribution, the structural bias of which was reduced as much as possible using the maximum-entropy methods-based pattern fitting method. Each crystal structure was composed of the three types of polyhedra, LaO_9, LaO_7 and SiO_4. With increasing temperature the $La_{9.33}(SiO_4)_6O_2$ crystal, together with the isotypic crystal of $Nd_{9.33}(SiO_4)_6O_2$, harmoniously and steadily expanded, with the mean linear thermal expansion coefficient of $9.4(1)\times10^{-6}$ K^{-1}. On the other hand, the thermal expansion behaviors of the coordination polyhedra are different, in particular, between LaO_9 and NdO_9. The thermal motions of O2 atoms at high temperatures showed significant difference between the two materials, which would lead to the different thermal motions of the rigid SiO_4 groups. This could correlate with the high oxide-ion conductivity of $La_{9.33}(SiO_4)_6O_2$.

Keywords: Lanthanum silicate; Oxide-ion conductor; Apatite-type structure; High-temperature X-ray powder diffraction; Rietveld method; Maximum entropy method; Electron density distribution.

4.1.1 Introduction

Apatite-type rare-earth (*RE*) silicates, $RE_{9.33}(SiO_4)_6O_2$, are promising materials for gas-sensing devices and electrolyte materials because of the relatively high oxide-ion conductivity at moderate temperatures as well as at low oxygen partial pressures [1,2]. The lanthanum silicate $La_{9.33}(SiO_4)_6O_2$ has exhibited much higher conductivity than the other *RE* silicates. The conductivity of the former at 1073 K was ~13.5×10^{-4} Scm^{-1}, which is one order of magnitude larger than that of, for example, neodymium silicate $Nd_{9.33}(SiO_4)_6O_2$ (~2.6×10^{-4} Scm^{-1} at 1073 K) [3]. Okudera *et al.* have investigated the temperature dependence of structural parameters in neodymium silicate up to 900 K using a single-crystal X-ray diffraction method [4]. Masubuchi *et al.* confirmed, using neutron powder diffraction method, that the crystal structures of both lanthanum and neodymium silicates were isotypic at ambient temperature, belonging to the space group $P6_3/m$ [3]. These two structural studies are reconciled with each other on the basis of the absence of interstitial oxygen sites in the crystal lattices. The interstitial oxide ions are considered to mediate the fast oxide-ion conductivity in *RE* silicates and/or oxygen-excess ones [5-9] such as $La_{8.65}Sr_{1.35}(SiO_4)_6O_{2.32}$ [10].

Recent advances in the field of crystal-structure analysis from X-ray powder diffraction (XRPD) data have enabled us to investigate the structural details that had not been introduced into the structural models. In order to disclose the structural details, the combined use of a maximum-entropy method (MEM) [11] and a MEM-based pattern fitting (MPF) method [12] is employed. The Rietveld [13] and MEM analyses are insufficient to readily determine charge densities because the observed

structure factors, F_o(Rietveld), are biased toward the structural models. The subsequent MPF method reduces the bias as much as possible. Thus, the MEM and MPF analyses are alternately repeated (REMEDY cycle) until the reliability indices no longer decrease. Crystal structures are represented not by structural parameters but by electron densities in MPF.

In the present study, we have, for the first time, investigated the crystal structure of lanthanum silicate at high temperature (*i.e.*, 1073 K). The structural change with increasing temperature has been compared with that of neodymium silicate with a view to clarifying the structural details that should be peculiar to the highly oxide-ion conducting apatite-type *RE* silicates.

4.1.2 Experimental
(1) Synthesis

A powder specimen of $La_{9.33}(SiO_4)_6O_2$ was prepared from stoichiometric amounts of reagent-grade chemicals La_2O_3 (Aldrich, 99.9%) and SiO_2 (Prolabo, 99%). Hygroscopic lanthanum oxide was pre-calcined at 1073 K for 30 min in order to remove lanthanum hydroxide and/or oxycarbonate phases to obtain the appropriate amount of La_2O_3. Well-mixed chemicals were heated at 1773 K for 4 h, and followed by quenching in air. The reaction product was a slightly sintered polycrystalline material. It was finely ground to obtain powder specimen.

(2) Characterization

The XRPD intensities were collected at 295 K on a PANalytical X'Pert PRO Alpha-1 diffractometer in Bragg-Brentano geometry using monochromatized $CuK\alpha_1$ radiation (45kV, 40mA) and a continuous-scan technique in a 2θ range from 17.0042° to 148.9647° (total of 15794 datapoints). The divergence slit of 0.5° was employed to collect the quantitative profile intensities over the whole 2θ range. The profile intensities were also collected at 1073 K on the diffractometer equipped with a heating stage (HTK-1200N, Anton Paar Co.) in a 2θ range from 24.0097° to 148.4920° (total of 7449 datapoints and divergence slit of 0.25°). The structural models were visualized with the computer program ORTEP-3 [14]. The three-dimensional electron density distribution (EDD) was visualized with the computer program VESTA [15]. The polyhedral parameters (*i.e.*, volumes and sphericity) were determined from calculation using the computer program IVTON [16].

4.1.3 Results and discussion
(1) Refinement and description of the crystal structure at 295K

The XRPD pattern of 295 K showed that the specimen was composed mainly of lanthanum silicate with a small amount of La_2SiO_5. The peak positions of the former material were determined using the computer program PowderX [17]. The 2θ values of 40 observed peak positions were then used as input data to the automatic indexing program TREOR90 [18]. One hexagonal cell was found with satisfactory figures of merit $M20/F20$ = 96/122(0.005673,29) and $M40/F40$ = 84/116(0.004498,77) [19,20]. The derived unit-cell parameters of a = 9.7152(2) nm and c = 7.1848(2) nm were subsequently used as starting parameters in the next stage of the analysis.

Initial structural parameters were taken from Okudera *et al.* [21] for lanthanum silicate, in which the occupancies (g) of 4*f* (La1) and 6*h* (La2) sites were 0.858 and 0.983, respectively. The structural parameters were refined by the Rietveld method using the program RIETAN-FP [22]. The structural model of La_2SiO_5 [23] was added into the refinement as additional phase. A Legendre polynomial was fitted to background intensities with twelve adjustable parameters. The pseudo-Voigt function [24] was used to fit the experimental peak profiles. Attempt was made to independently refine

72

the occupancies of La1 and La2 sites. However, each occupancy as well as the total number of La atoms in the unit cell remained almost unchanged, which implies that the chemical formula of the present specimen is $La_{9.33}(SiO_4)_6O_2$. Thus we imposed the linear constrains on occupancies of $4 \times g(La1) + 6 \times g(La2) = 9.33$ in successive least-squares cycles. Isotropic atomic displacement parameters were initially assigned to all atoms. The refinement resulted in the reliability (R) indices of $R_{wp} = 7.10\%$ ($S = R_{wp}/R_e = 1.30$), $R_p = 5.52\%$, $R_B = 2.49\%$ and $R_F = 1.23\%$ [25]. We subsequently assigned anisotropic atomic displacement (U) parameters to obtain the lower R indices of $R_{wp} = 6.76\%$ ($S = 1.24$), $R_p = 5.22\%$, $R_B = 2.39\%$ and $R_F = 1.02\%$. The refined cell dimensions and the final positional and U parameters of atoms are given in Table 4-1. The refined structural model was comparable to the initial model, which is free from interstitial oxygen sites, determined by Okudera et al. [21]. Quantitative X-ray analysis with correction for microabsorption according to Brindley's procedure [26] was implemented in the program RIETAN-FP. The sample was found to be composed of 96.6 mass% $La_{9.33}(SiO_4)_6O_2$ and 3.4 mass% La_2SiO_5.

The MPF method was subsequently applied, so as to extract structural details and consequently improve the EDD. After two REMEDY cycles, R_B and R_F decreased to 1.25% and 0.75%, respectively. Subtle changes in EDD arose out of MPF, which effectively improved F_o(MPF) data and consequently the R factors. The decreases in R_B and R_F demonstrate that the crystal structure is better expressed with electron densities than with the structural parameters in Table 4-1. Observed, calculated, and difference XRPD patterns for the final MPF are plotted in Fig. 4-1(a). We expected MPF to disclose the structural details, such as interstitial oxygen sites, that had not been introduced into the structural model. However, the EDD determined by MPF (Fig. 4-2(b)) was explained satisfactorily by the final structural model (Fig. 4-2(a)). This implies that the existence of the interstitial oxygen sites is improbable, in accord with previous studies [3, 4, 21].

Selected interatomic distances and bond angles, together with their standard deviations, are given in Table 4-2. The mean Si-O bond length of 0.162 nm in the SiO_4 tetrahedra is in good agreement with that expected from the bond valence sum (0.162nm). The La1 atom is coordinated to nine oxygen atoms, forming a tricapped trigonal prism with bond lengths ranging from 0.2496 to 0.2878 nm (the mean = 0.264 nm). A similar geometry around the La atom has been described in La_2SiO_5 (the mean = 0.260 nm) [23] and $NaLaP_2O_4$ (0.260 nm) [27]. The La2 atom is sevenfold coordinated with a mean La2-O distance of 0.253 nm, which is comparable to those of the LaO_7 polyhedra in La_2SiO_5 (the mean = 0.251 nm) [23] and $La_4Au_2O_9$ (the mean = 0.250 nm) [28]. The ratio of the volume of the circumscribed sphere to that of the polyhedron (V_S/V_P) for $La2O_7$ is 2.76. Because the V_S/V_P values of the ideal pentagonal bipyramid and the ideal capped octahedron are 2.643 and 3.049, respectively [29], the present $La2O_7$ polyhedron can be described as a distorted pentagonal bipyramid.

(2) Refinement of the crystal structure at 1073K and structural change upon heating

The refinement process for the crystal structure of 1073 K was very similar to that described above. The final reliability indices calculated from the Rietveld refinement were $R_{wp} = 11.01\%$ ($S = 1.11$), $R_p = 8.24\%$, $R_B = 2.72\%$ and $R_F = 2.95\%$ [25]. The positional and U parameters of atoms are given in Table 4-1. The MPF method was eventually applied, which decreased the R_B and R_F indices to 2.49% and 1.86%, respectively. Observed, calculated, and difference XRPD patterns for the final MPF are plotted in Fig. 4-1(b). The decreases in R_B and R_F indicate that the crystal structure is represented more adequately with electron densities than with structural parameters. However, the EDD was very slightly modified by the MPF, and hence we concluded that the refined structural model is satisfactory. Selected interatomic distances and bond angles, together with their standard deviations, are given in Table 4-2.

The normalized cell dimensions (x/x_{295K}) of lanthanum silicate at 1073 K and those of neodymium silicate up to 900 K [4] are plotted together in Fig. 4-3, where x is the cell dimensions at T (K) and x_{295K} the cell dimensions at 295 K. The x/x_{295K}–values of the two different compounds increased harmoniously and steadily with increasing temperature up to 1073 K. The variations were well fitted to the second order polynomial as follows:

$$x/x_{295K} = 1 + A\Delta T, + B(\Delta T)^2$$

where $\Delta T = T - 295$. The constants A (K^{-1}) and B (K^{-2}) are $A = 9.6 \times 10^{-6}$ and $B = 7.4 \times 10^{-10}$ for the a axis and $A = 9.4 \times 10^{-7}$ and $B = 8.5 \times 10^{-9}$ for the c axis. The magnitude of expansion along the a axis was ~1.8 times that along the c axis at 1073 K. The crystal as a whole showed the thermal expansion of ~2.2 % in volume during heating from 295 to 1073 K. The thermal expansion is usually represented by linear thermal expansion coefficients, α_x, which are derived from the linear strains (x/x_{295K} - 1) as follows:

$$\alpha_x = (x/x_{295K} - 1)/\Delta T \quad [K^{-1}].$$

The mean linear expansion coefficient, which is equivalent to $[2 \times \alpha_a + \alpha_c]/3$, was $9.4(1) \times 10^{-6}$ K^{-1} in the temperature range of 295 to 1073 K.

The thermal expansion of lanthanum silicate is accompanied by the polyhedral deformation of both $La2O_7$ and $La1O_9$; the amount of volumetric expansion is larger for the former polyhedron (3.3%) than for the latter (1.8%) (Fig. 4-4). The sphericity (σ) of $La2O_7$ decreased on heating from 295 to 1073 K, while that of $La1O_9$ slightly increased as shown in Fig. 4-5, with the slopes (= $\Delta\sigma/\Delta T$) for the two sets of data being $-7.7 \times 10^{-6} K^{-1}$ and $2.6 \times 10^{-6} K^{-1}$, respectively. Neither the deformation nor volumetric change is recognized for SiO_4 tetrahedron. Thus, the thermal expansion of lanthanum silicate would be principally induced by the anisotropic expansion of $La2O_7$ polyhedra. On the other hand, the volumetric increases of $Nd1O_9$ and $Nd2O_7$ polyhedra on heating from 295 to 900 K were nearly identical to each other (Fig. 4-4). The sphericity of $Nd2O_7$ tends to decrease with increasing temperature, while that of $Nd1O_9$ remains nearly constant (Fig. 4-5), in analogy with the changes in sphericity of the coordination polyhedra in lanthanum silicate. Accordingly, in contrast to the harmonious behaviors in bulk thermal expansion of the two materials, the thermal expansion behaviors of the coordination polyhedra are different, in particular, between the volumetric expansion behaviors of $La1O_9$ and $Nd1O_9$ (Fig. 4-4).

In the present refinements of the structural models of 295 and 1073 K, we have succeeded in assigning the U parameters, which reflect the time- and space-averaged distribution of atoms around their mean positions in the crystal lattice. The U parameters are usually found to be composite quantities with contributions from motions (libration, translation, internal vibrations), static or dynamic disorder and systematic error. At high temperatures, the parameters can be regarded mostly as quantities with contributions from thermal motions. At 1073 K, the thermal motion of Si atom was nearly isotropic, while those of the ligand O atoms (O1, O2 and O3) were highly anisotropic with the smallest displacement in almost the Si-O bond directions (Fig. 4-6(a)). When compared the corresponding thermal vibration ellipsoids of lanthanum silicate at 1073 K with those of neodymium silicate at 900 K (Fig. 4-6(b)), a significant difference has been found for the O2 atoms. With the O2 ellipsoid in the former silicate, the largest magnitude of thermal motion was aligned nearly along <100>, followed by the thermal vibration along <001> (Fig. 4-6(a)). On the other hand, there was a dominant thermal motion along <001> for the latter silicate (Fig. 4-6(b)). Since the SiO_4 groups may be considered as rigid bodies in the crystals, we tried the **TLS** analysis [30-32] using the thermal motion analysis program *THMA*11 [33] to describe the overall motions of the tetrahedra by a translation tensor **T**, a libration tensor **L** and a coupling tensor **S**. However, we failed in deriving the information on rigid-body libration and translation, probably because the tetrahedra are librating in highly restricted space. Actually, the SiO_4 tetrahedron shares the O2-O3 edges with two $La1O_9$ polyhedra and the O3-O3

74

edge with one La2O$_7$ polyhedron. The oxygen atoms other than O4 are covalently bonded to Si atoms. Hence, the conduction species in the present lanthanum and neodymium silicates must be O4 atoms. The different thermal vibrations of the O2 atoms would lead to the different motions of the rigid SiO$_4$ groups, which could correlate with the higher mobility of O4 atoms in the lanthanum silicate. Details of this mechanism still remain equivocal, and should be investigated further.

4.1.4 Conclusions

We successfully refined the crystal structures of La$_{9.33}$(SiO$_4$)$_6$O$_2$ at 295 and 1073 K, being hexagonal with space group $P6_3/m$. The isotypic crystals of La$_{9.33}$(SiO$_4$)$_6$O$_2$ and Nd$_{9.33}$(SiO$_4$)$_6$O$_2$, harmoniously and steadily expanded with increasing temperature, with the mean linear thermal expansion coefficient of $9.4(1) \times 10^{-6}$ K^{-1}. On the other hand, the thermal expansion behaviors of the coordination polyhedra are different, in particular, between La1O$_9$ and Nd1O$_9$. The thermal motions of O2 atoms at high temperatures showed significant difference between the two materials, which would lead to the different thermal motions of the rigid SiO$_4$ groups. This could correlate with the high oxide-ion conductivity of La$_{9.33}$(SiO$_4$)$_6$O$_2$.

Acknowledgment

References

[1] S. Nakayama, T. Kageyama, H. Aono, Y. Sadaoka, *J. Mater. Chem.* **5** (1995) 1801.

[2] S. Nakayama, M. Sakamoto, *J. Eur. Ceram. Soc.* **18** (1998) 1413.

[3] Y. Masubuchi, M. Higuchi, T. Takeda, S. Kikkawa, *Solid State Ionics* **177** (2006) 263.

[4] H. Okudera, A. Yoshiasa, Y. Masubuchi, M. Higuchi, S. Kikkawa, *J. Solid State Chem.* **177** (2004) 4451.

[5] J. E. J Sansom, D. Richings, P.R. Slater, *Solid State Ionics* **139** (2001) 205.

[6] J. R. Tolchard, M. S. Islam, P. R. Slater, *J. Mater. Chem.* **13** (2003) 1956.

[7] L. León-Reina, E. R. Losilla, M. Martínez-Lara, S. Bruque, M. A. G. Aranda, *J. Mater. Chem.* **14** (2004) 1142.

[8] L. León-Reina, E. R. Losilla, M. Martínez-Lara, S. Bruque, A. Lolbet, D. V. Sheptyakow, M. A. G. Aranda, *J. Mater. Chem.* **15** (2005) 2489.

[9] J. E. H. Sansom, J. R. Tolchard, M. S. Islam, D. Apperley, P. R. Slater, *J. Mater. Chem.* **16** (2006) 1410.

[10] L. León-Reina, J. M. Porras-Vázquez, E. R. Losilla, M. A. G. Aranda, *Solid State Ionics* **177** (2006) 1307.

[11] M. Takata, E. Nishibori, M. Sakata, *Z. Kristallogr.* **216** (2001) 71.

[12] F. Izumi, S. Kumazawa, T. Ikeda, W.-Z. Hu, A. Yamamoto, K.Oikawa, *Mater. Sci. Forum* **378–381** (2001) 59.

[13] H. M. Rietveld. *J. Appl. Crystallogr.* **2** (1969) 65.

[14] L. J. Farrugia, *J. Appl. Crystallogr.* **30** (1997) 565.

[15] K. Momma, F. Izumi, *IUCr Newslett.* **7** (2006) 106.

[16] T. Balic-Zunic, I. Vickovic, *Acta Crystallogr.* **A29** (1996) 305.

[17] C. Dong, *J. Appl. Crystallogr.* **32** (1999) 838.

[18] P. E. Werner, L. Eriksson, M. Westdahl, *J. Appl. Crystallogr.* **18** (1985) 367.

[19] P. M. de Wolff, *J. Appl. Crystallogr.* **1** (1968) 108.

[20] G. S. Smith, R. L. Snyder, *J. Appl. Crystallogr.* **12** (1979) 60.

[21] H. Okudera, Y. Masubuchi, S. Kikkawa, A. Yoshiasa, *Solid State Ionics* **176** (2005) 1473.

[22] F. Izumi, T. Ikeda, *Mater. Sci. Forum* **321–324** (2000) 198.

[23] K. Fukuda, T. Iwata, E. Champion, *Powder Diffr.* **21** (2006) 300.

[24] H. Toraya, *J. Appl. Crystallogr.* **23** (1990) 485.

[25] R. A. Young, in: R. A. Young (Ed.), The Rietveld Method, Oxford University Press, Oxford, UK, 1993, pp.1–38.

[26] G. W. Brindley, *Bulletin de la Societe Chimique de France*, (1949) D59.

[27] M. Ferid, K. Horchani-Naifer, *Mater. Res. Bull.* **39** (2004) 2209.

[28] R. Maetina, J. Martin, *J. Alloys Compd.* **203** (1994) 7.

[29] E. Makovicky, T. Balic-Zunic, *Acta Crystallogr.* **B54** (1998) 766.

[30] D. W. J. Cruickshank, *Acta Crystallogr.* **9** (1956) 754.

[31] D. W. J. Cruickshank, *Acta Crystallogr.* **9** (1956) 1005.

[32] V. Schomaker, K. N. Trueblood, *Acta Crystallogr.* **B24** (1968) 63.

[33] K. N. Trueblood, *Acta Crystallogr.* **A34** (1978) 950.

Table 4-1

Structural parameters and atomic displacement parameters ($\times 10^{-2}$ nm^2) at 295 K and 1073 K

	295 K	1073 K
a (nm)	0.971872(6)	0.97963(6)
c (nm)	0.718733(3)	0.72304(3)
La1 site, $4f$ (2/3, 1/3, z)		
occpancy	0.869(1)	0.868(2)
z	0.0007(2)	0.0001(6)
U_{11}	0.0080(2)	0.0305(9)
U_{33}	0.0219(4)	0.038(1)
La2 site, $6h$ (x, y, 1/4)		
occpancy	0.978	0.977
x	0.01236(9)	0.0128(3)
y	0.23963(6)	0.2405(2)
U_{11}	0.0061(3)	0.023(1)
U_{22}	0.0099(4)	0.027(1)
U_{33}	0.0100(2)	0.0276(8)
U_{12}	0.0035(3)	0.010(1)
Si site, $6h$ (x, y, 1/4)		
x	0.4031(3)	0.4022(9)
y	0.3730(2)	0.3739(9)
U_{11}	0.011(1)	0.028(5)
U_{22}	0.006(2)	0.028(5)
U_{33}	0.010(1)	0.024(4)
U_{12}	0.006(1)	0.016(4)
O1 site, $6h$ (x, y, 1/4)		
x	0.3217(5)	0.323(2)
y	0.4834(6)	0.484(2)
U_{11}	0.028(4)	0.07(1)
U_{22}	0.024(4)	0.07(1)
U_{33}	0.017(4)	0.04(1)
U_{12}	0.021(4)	0.05(1)
O2 site, $6h$ (x, y, 1/4)		
x	0.5265(6)	0.531(2)
y	0.1219(4)	0.124(1)
U_{11}	0.008(4)	0.05(1)
U_{22}	0.015(4)	0.05(1)
U_{33}	0.022(4)	0.04(1)
U_{12}	0.006(3)	0.04(1)
O3 site, $12i$ (x, y, z)		
x	0.3443(5)	0.343(1)
y	0.2564(4)	0.257(1)
z	0.0704(3)	0.073(1)
U_{11}	0.052(3)	0.071(9)
U_{22}	0.015(3)	0.033(8)
U_{33}	0.013(3)	0.046(8)
U_{12}	0.020(3)	0.025(7)
U_{13}	-0.015(2)	-0.028(6)
U_{23}	-0.003(2)	-0.004(6)
O4 site, $2a$ (0, 0, 1/4)		
U_{11}	0.025(4)	0.05(1)
U_{33}	0.26(1)	0.24(3)

The site symmetries give the following constraints: $U_{11}=U_{22}=2U_{12}$ for La1 site, $U_{13}=U_{23}=0$ for O4 site and $U_{13}=U_{23}=0$ for La2, Si, O1 and O2 sites.

Table 4-2

Selected interatomic distances (nm) and angles (°)

	295K	1073K
La1 site		
La-O1 [×3]	0.2496(4)	0.251(1)
La-O2 [×3]	0.2547(4)	0.255(1)
La-O3 [×3]	0.2878(4)	0.292(1)
Mean	0.264	0.266
La2 site		
La-O1	0.2744(5)	0.277(2)
La-O2	0.2523(4)	0.257(1)
La-O3 [×2]	0.2476(2)	0.2498(5)
La-O3' [×2]	0.2610(3)	0.263(1)
La-O4	0.22712(9)	0.2296(2)
Mean	0.253	0.255
Si site		
Si-O1	0.1621(4)	0.162(1)
Si-O2	0.1619(6)	0.162(1)
Si-O3 [×2]	0.1621(3)	0.1622(7)
Mean	0.162	0.162
O1-Si-O2	113.5(2)	114.7(4)
O1-Si-O3 [×2]	110.1(1)	110.4(2)
O2-Si-O3 [×2]	108.6(2)	108.2(3)
O3-Si-O3	105.5(2)	104.5(4)

Figure captions
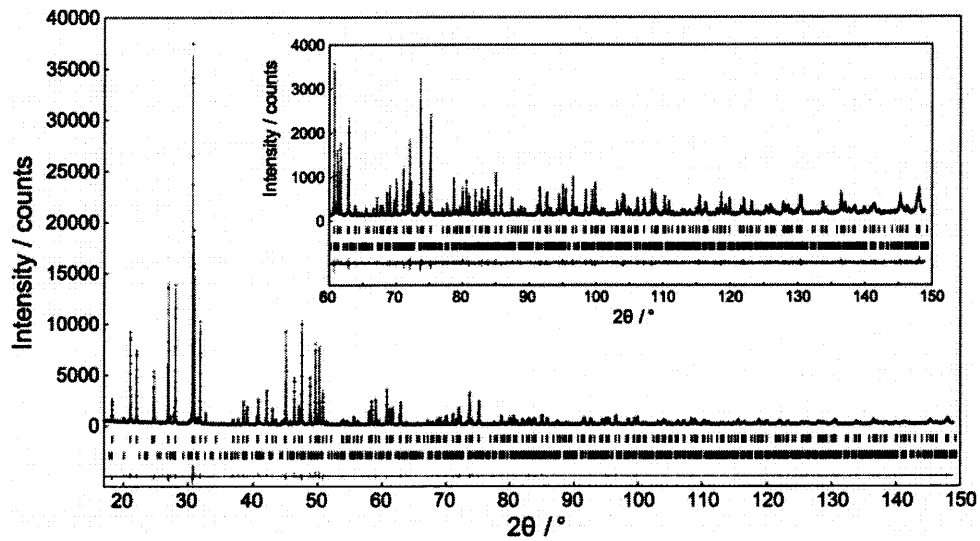
Fig. 4-1. Comparison of the observed diffraction patterns (symbol: +) of $La_{9.33}(SiO_4)_6O_2$ and La_2SiO_5 with the corresponding calculated patterns (upper solid line). The difference curve is shown in the lower part of each diagram. Upper vertical bars indicate the positions of possible Bragg reflections for $La_{9.33}(SiO_4)_6O_2$ and those of the lower for La_2SiO_5. The profile intensities collected at (a) 295 K and (b) 1073K.
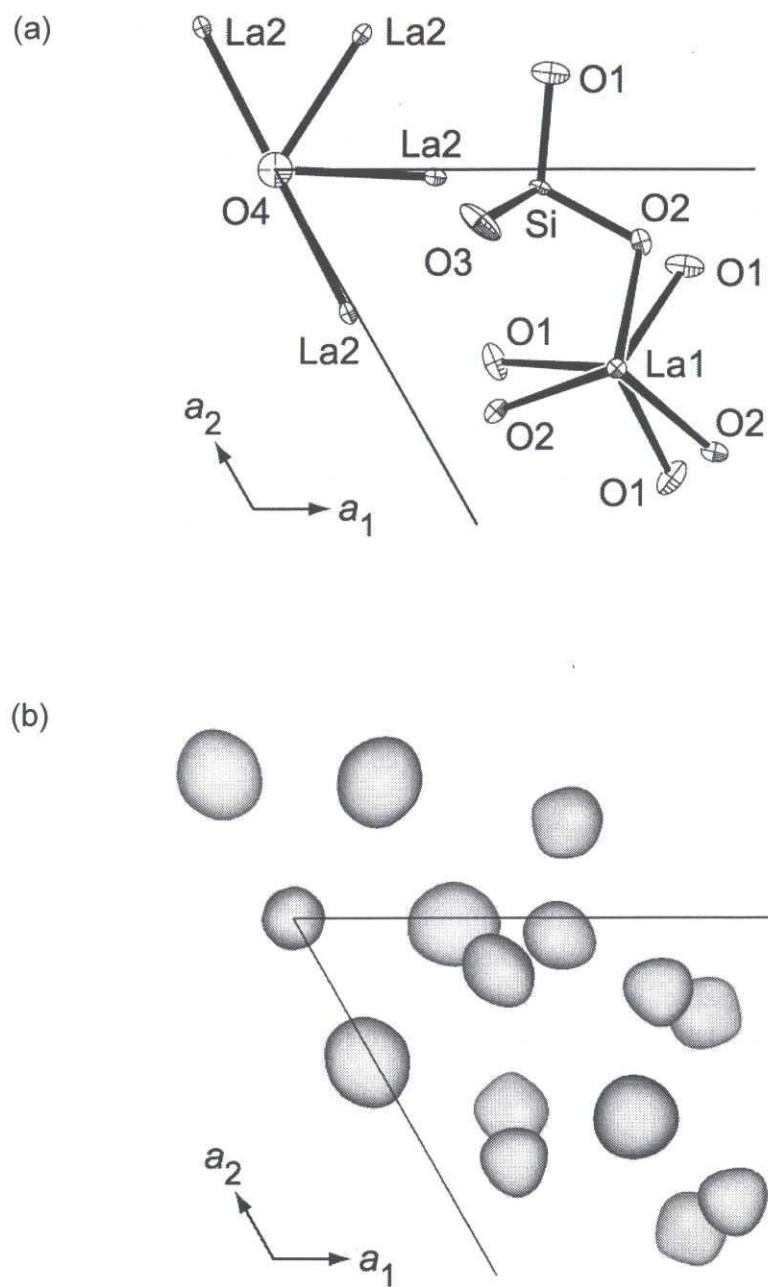
Fig. 4-2. Comparison of (a) the refined structural model of 295 K with (b) the corresponding electron density distribution determined by MPF method. Thermal ellipsoids represent 50% of probability. Isosurfaces expressed in smooth shading style for an equidensity level of 0.0025 nm^{-3}.
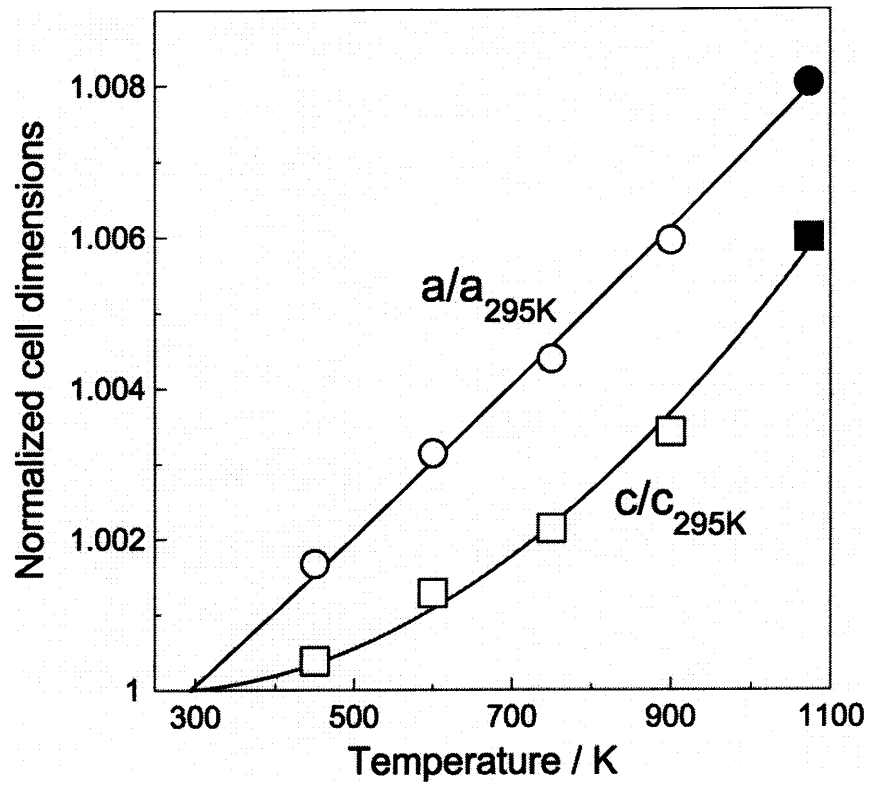
Fig. 4-3. Changes of normalized cell dimensions with temperature for (● and ■) $La_{9.33}(SiO_4)_6O_2$ and (○ and □) $Nd_{9.33}(SiO_4)_6O_2$. The data of the latter material taken from a previous study [4].
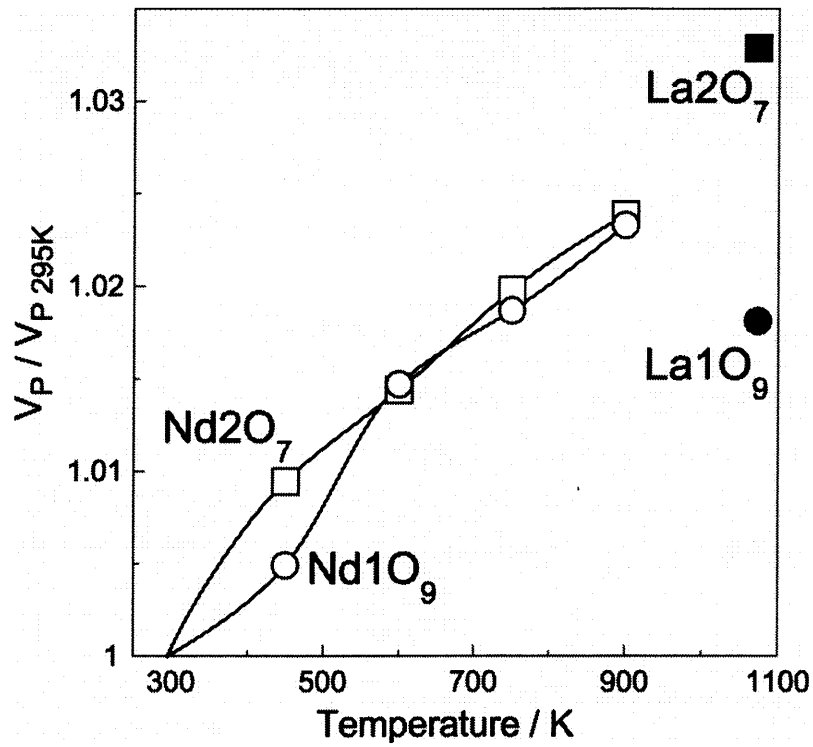
Fig. 4-4. Changes of normalized polyhedral volumes with temperature for $RE1O_9$ and $RE2O_7$, where RE = La and Nd. The polyhedral volumes with RE = Nd found from calculation on the basis of the structural parameters of $Nd_{9.33}(SiO_4)_6O_2$ [4]. The polyhedral volumes determined from calculation using the computer program IVTON [16].
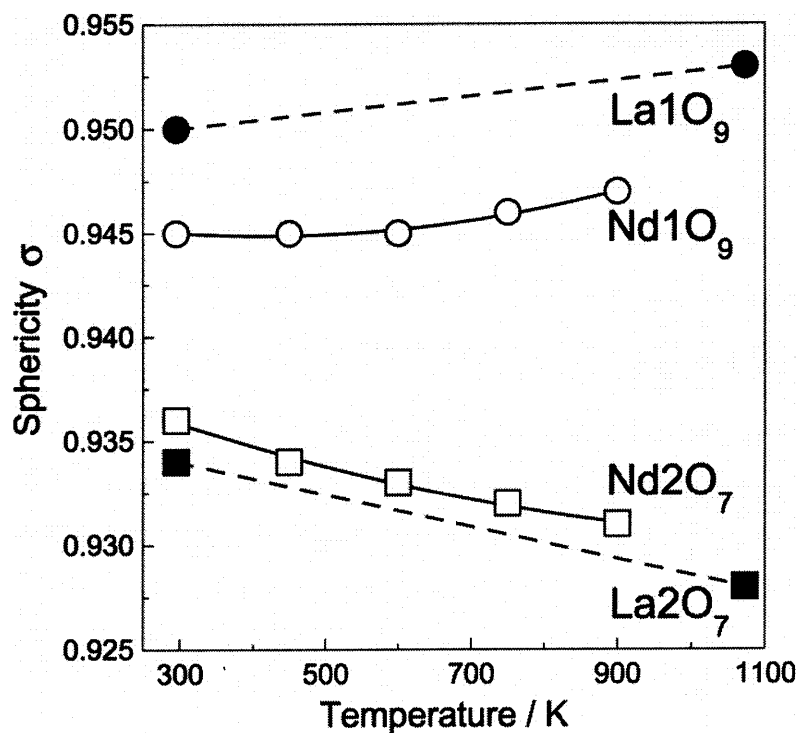
Fig. 4-5. Changes of sphericity with temperature for $RE1O_9$ and $RE2O_7$ polyhedra, where RE = La and Nd. The sphericity of polyhedra with RE = Nd found from calculation on the basis of the structural parameters of $Nd_{9.33}(SiO_4)_6O_2$ [4]. The sphericity values determined from calculation using the computer program IVTON [16].
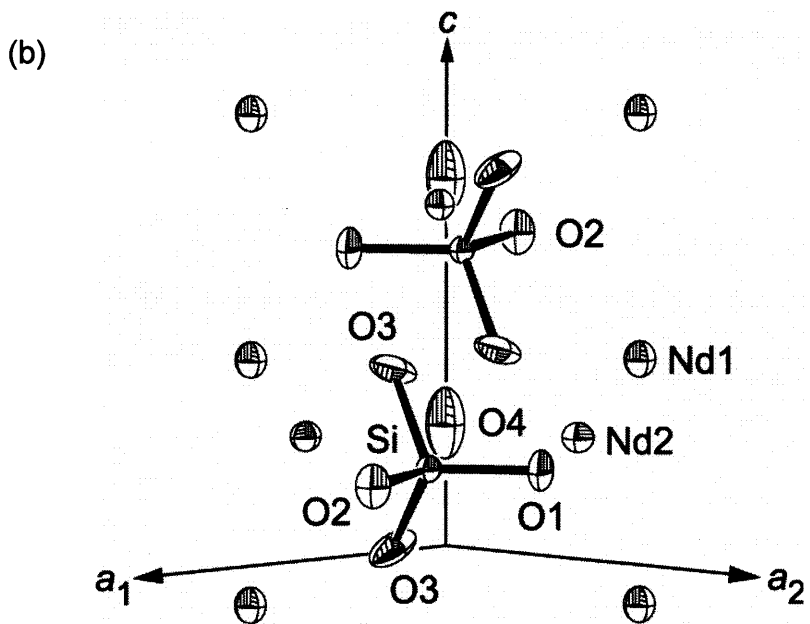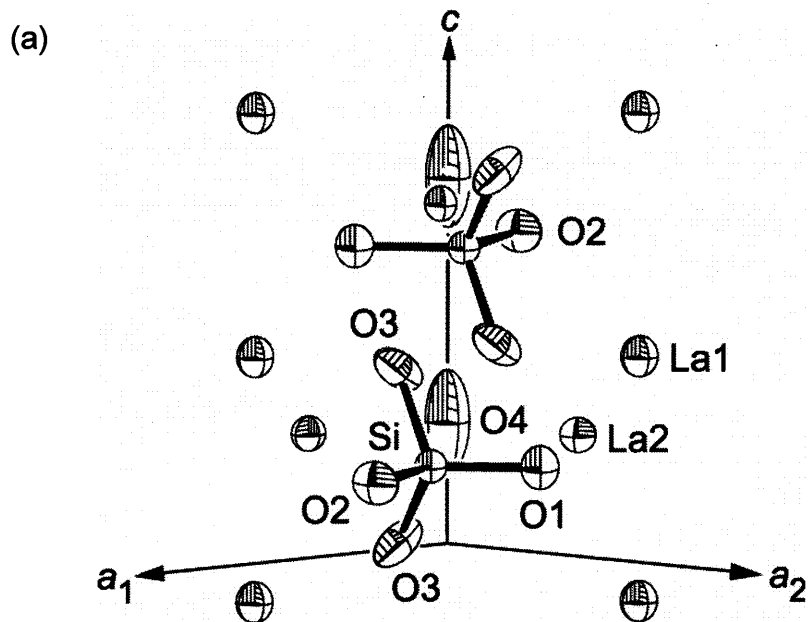
Fig. 4-6. ORTEP diagrams of (a) $La_{9.33}(SiO_4)_6O_2$ at 1073 K and (b) $Nd_{9.33}(SiO_4)_6O_2$ at 900 K [3] viewed along [441]. Thermal ellipsoids represent 50% of probability.

4.2 Lanthanum- and oxygen-deficient crystal structures of oxide-ion conducting apatite-type silicates

Abstract

Structural change of $La_{9.33-2x}(SiO_4)_6O_{2-3x}$ with increasing x-value was investigated by means of laboratory X-ray powder diffraction $(CuK\alpha_1)$. Crystal structures of the three-types of specimens with x = 0, 0.06 and 0.085 were refined by the Rietveld method, with the anisotropic displacement (U) parameters being assigned for all atoms. Each crystal structure was composed of three types of polyhedra, $La1O_9$, $La2O_7$ and SiO_4. With increasing x-value, the occupancies (g) of both La1 and La2 sites steadily decreased. The La vacancies were charge balanced by the deficiency of the mobile O atoms that were not covalently bonded to Si atoms. The polyhedral volume of $La2O_7$ steadily decreased about 0.7 % with the decrease of g(La2)-value from 0.995 to 0.982. On the other hand, the polyhedral volume of $La1O_9$ showed an increase of about 1.0 % with the decrease of the g(La1)-value from 0.841 to 0.818. The marked difference in deformation behavior of the two-types of polyhedra could be attributable to the distinction in site occupancies between La1 [g(La1) < 0.85] and La2 [g(La2) > 0.98]. For the mobile O atoms, the displacement magnitudes, being evaluated from the U parameters, steadily decreased with increasing x-value. The positional disordering of these atoms might be related to their mobilities at high temperatures.

Keywords: Lanthanum silicate; Oxide-ion conductor; Apatite-type structure; X-ray powder diffraction; Rietveld method

4.2.1 Introduction

Apatite-type lanthanum silicates are among the most promising materials for gas-sensing devices and electrolyte materials because of the relatively high oxide-ion conductivity at moderate temperatures as well as at low oxygen partial pressures [1, 2] Okudera *et al.* have confirmed, using a single-crystal X-ray diffraction method, that the crystal structure of lanthanum silicate belongs to the space group $P6_3/m$ at ambient temperature [3]. Iwata *et al.* have investigated the temperature dependence of structural parameters in $La_{9.33}(SiO_4)_6O_2$ up to 1073 K using an X-ray powder diffraction method [4]. These two structural studies are reconciled with each other on the basis of the absence of interstitial oxygen sites in the crystal lattices. The interstitial oxide ions are considered to mediate the fast oxide-ion conductivity in rare earth silicates [5-10]. Recently, the influence of cationic and/or anionic vacancies on the ionic conductivity has been investigated for SrO-doped lanthanum silicates [11]. However, structural details of the lanthanum- and oxygen-deficient apatite-type silicates have still not been elucidated.

In the La_2O_3-SiO_2 binary system, there are two other compounds established so far [12], La_2SiO_5 [13] in the La_2O_3-rich region and $La_2Si_2O_7$ [14, 15] in the SiO_2-rich region. The latter crystal has two polymorphs; one is monoclinic (denoted by m-$La_2Si_2O_7$) and the other tetragonal (t-$La_2Si_2O_7$). These three types of compounds tend to coexist with the apatite-type lanthanum silicate even though the samples were carefully prepared.

In the present study, we have characterized the crystal structures of lanthanum- and oxygen-deficient apatite-type silicates, the general formula of which is represented by $La_{9.33-2x}(SiO_4)_6O_{2-3x}$, ($0 \leq x \leq 0.085$). The crystal structures of x = 0.06 and 0.085 have been compared with that of x = 0 with a view to clarifying the structural change with increasing x-value.

4.2.2 Experimental Procedure

(1) Syntheses

Three types of powder specimens with different molar ratios of La/Si, ranging from 8.87/6 to 9.33/6, were prepared from reagent-grade chemicals of La_2O_3 (Aldrich, 99.9%) and SiO_2 (Prolabo, 99%). Hygroscopic lanthanum oxide was pre-calcined at 1073 K for 30 min in order to remove lanthanum hydroxide and/or oxycarbonate phases to obtain the appropriate amount of La_2O_3. Individual well-mixed chemicals were heated at 1773 K for 4 h, and followed by quenching in air. The reaction products were slightly sintered polycrystalline materials. They were finely ground to obtain powder specimens. With increasing La/Si ratio, the samples were termed S-A (La/Si = 8.87/6), S-B (9.10/6) and S-C (9.33/6).

(2) Characterization

Two types of XRPD patterns with and without the reflections from the internal standard Si were collected for each sample on a diffractometer (PANalytical X'Pert PRO Alpha-1) in Bragg-Brentano geometry using monochromatized $CuK\alpha_1$ radiation (45kV, 40mA) and a continuous-scan technique in a 2θ range from 9.00718° to 148.90557° (total of 16744 datapoints and total experimental time of 11.1 h). The automatic divergence slit was employed to maintain an illumination length of 5 mm on the sample. Thus, the quantitative profile intensities were collected over the whole 2θ range. The structural data were standardized using the computer program STRUCTURE TIDY [16]. The structural models were visualized with the computer program ORTEP-3 [17]. The polyhedral parameters (i.e., volume and eccentricity) were determined from calculation using the computer program IVTON [18].

4.2.3 Results and discussion

(1) Structure refinements and chemical compositions of apatite-type crystals

The XRPD patterns (Fig. 4-7) showed that the individual samples were composed mainly of the apatite-type lanthanum silicate with small amounts of impurities such as La_2SiO_5 [13], m-$La_2Si_2O_7$ [14] and t-$La_2Si_2O_7$ [15]. The unit-cell parameters of the apatite-type crystals were refined by the Le Bail method [19] for the XRPD data with Si reflections using the computer program RIETAN-FP [20]. The derived unit-cell parameters were used as the starting parameters in the subsequent Rietveld analysis for structure refinement using the program RIETAN-FP. The initial structural parameters were taken from Okudera et al. [3] for $La_{9.33}(SiO_4)_6O_2$, in which the occupancies (g) of $4f$ (La1) and $6h$ (La2) sites were 0.858 and 0.983, respectively. The structural models of the impurities were added into the refinement as additional phases. A Legendre polynomial was fitted to background intensities with twelve adjustable parameters. The pseudo-Voigt function [21] was used to fit the experimental peak profiles. We initially assigned isotropic atomic displacement parameters, and subsequently assigned anisotropic atomic displacement (U) parameters to all atoms of the apatite-type lanthanum silicate.

In the initial stage of the refinement process, the occupancies of La1 and La2 sites in the apatite-type crystals were independently refined without any constrains. With S-A and S-B, the total number of La atoms in the unit cell (= $4 \times g$(La1) + $6 \times g$(La2)) eventually converged to the smaller values than 9.33, indicating the additional vacancies in La sites. Because the oxygen atoms other than O4 are covalently bonded to Si atoms, the La vacancies must be charge balanced exclusively by the deficiency of O4 atoms. Thus, we have refined the crystal structures under the charge-balance constrains of $3 \times g$(La1) + $4.5 \times g$(La2) = g(O4) + 6. The refinement resulted in the lanthanum and oxygen-deficient chemical compositions, the chemical formulas of which were represented by $La_{9.16(3)}(SiO_4)_6O_{1.75(4)}$ for S-A and $La_{9.21(2)}(SiO_4)_6O_{1.81(3)}$ for S-B, where the numbers in parentheses

86

indicate standard deviations. With S-C, attempt was made to independently refine the occupancies of La1 and La2 sites. However, the total number of La atoms in the unit cell remained almost unchanged. This implies that the chemical formula of the apatite-type crystal is $La_{9.33}(SiO_4)_6O_2$. Thus we imposed the linear constrains on occupancies of $4 \times g(La1) + 6 \times g(La2) = 9.33$ in successive least-squares cycles. The refined structural model in S-C was comparable to the initial model, although the refined site occupancies were slightly different from those of the previous studies [3, 4]. The site occupancies could sensitively reflect the processing conditions (e.g., heating time and cooling rate) of the samples. The crystal data of the lanthanum silicates in S-A, S-B and S-C are given in Table 4-3, and the final positional and U parameters of atoms are given in Table 4-4. The final structural models are shown in Fig. 4-8.

Quantitative X-ray analysis with correction for microabsorption according to Brindley's procedure [22] was implemented in the program RIETAN-FP. The resulting phase compositions of the samples S-A, S-B and S-C are given in Table 4-5. On the basis of the phase constitution, the bulk chemical compositions of the three samples were, in turn, determined from calculation. The bulk La/Si ratios were found to be 8.87/6 for S-A, 9.10/6 for S-B and 9.33/6 for S-C. Each composition was in excellent agreement with that of the corresponding initial mixture, indicating that the chemical compositions of the lanthanum silicates that were determined by the Rietveld method are quite reliable. As a result, the coupled deficiency of lanthanum and oxygen atoms was confirmed for the lanthanum silicates in S-A and S-B. The present lanthanum silicates were satisfactorily represented by the general formula of $La_{9.33-2x}(SiO_4)_6O_{2-3x}$ with $x = 0.085(13)$ for S-A, $x = 0.06(1)$ for S-B and $x = 0$ for S-C, where the numbers in parentheses indicate standard deviations.

In S-C, the crystals of $La_{9.33}(SiO_4)_6O_2$ [La/Si = 9.33/6 (= 1.56)] and La_2SiO_5 (La/Si = 2) coexisted (Table 4-5). This implies that the existence of the apatite-type crystals with La/Si > 9.33/6 in the La_2O_3-SiO_2 binary system are improbable at least in samples synthesized by the present experimental method. These apatite-type crystals are considered to have relatively high oxide-ion conductivity owing to the existence of interstitial oxygen atoms in the crystal lattices.[5-10]

(2) Structure description

With increasing x-value, the a-axis length of $La_{9.33-2x}(SiO_4)_6O_{2-3x}$ steadily decreased, while the c-axis length varied in an opposite manner with a particularly strong linear correlation of $c = 0.71848 + 0.0068x$ nm (Fig. 4-9). Due to this adverse effect, the unit-cell volume remained almost unaltered regardless of the x-value.

Selected interatomic distances and bond angles, together with their standard deviations, are given in Table 4-6 The mean Si-O bond lengths ranging from 0.1623 nm to 0.1624 nm in the SiO_4 tetrahedra are in good agreement with that expected from the bond valence sum (0.162nm). With the increase in x-value, the mean La2-O distance (especially La2-O1 and La2-O2), the volume of the $La2O_7$ polyhedra and its eccentricity steadily decreased (Table 4-4 and Figs. 4-10 and 4-11). On the other hand, the mean La1-O bond length (especially La1-O1), the $La1O_9$ polyhedral volume and the eccentricity increased with increasing x-value. Neither the deformation nor volumetric change is recognized for SiO_4 tetrahedron (Table 4-5).

The site occupancies of $g(La1)$, $g(La2)$ and $g(O4)$ decreased steadily with increasing x-value (Fig. 4-12). When compared the occupancies of La1 and La2 sites, the former occupancy was much lower than that of the latter regardless of the x-value; the values of $g(La1)$ were necessarily lower than 0.85 and those of $g(La2)$ were always higher than 0.98. The polyhedral volume of $La2O_7$ steadily decreased about 0.7 % with the decrease of $g(La2)$-value from 0.995 to 0.982 (Fig. 4-13(B)). On the other hand, the polyhedral volume of $La1O_9$ showed an increase of about 1.0 % with the decrease of the

g(La1)-value from 0.841 to 0.818 (Fig. 4-13(A)). The marked difference in deformation behavior of the two types of polyhedra could be attributable to the distinction between the occupancies of La1 and La2 sites. The extraction of the positively charged La ions from the $La1O_9$ polyhedron could more effectively induce the anion-anion repulsion between the neighboring oxygen atoms, which would eventually cause the volumetric expansion of the $La1O_9$ polyhedron. Actually the O1-O1 and O1-O2 distances of the polyhedron appreciably increased, respectively, from 0.313(1) to 0.321(1) nm and from 0.3655(2) to 0.3666(2) nm with the decrease of the g(La1)-value from 0.841 (x = 0) to 0.818 (x = 0.085).

The oxygen atoms other than O4 are covalently bonded to Si atoms. Hence, the conduction species in the apatite-type lanthanum silicate must be O4 atoms. The conduction paths of the O4 atoms, which could be affected by the polyhedral deformation of both $La1O_9$ and $La2O_7$ in the crystal structure, as well as the site occupancy in O4 would strongly correlate with the oxide-ion conductivity. In the present refinements of the structural models, we have succeeded in assigning the U parameters, which reflect the space- and time-averaged distribution of atoms around their mean positions in the crystal lattice. The U parameters are usually found to be composite quantities with contributions from static or dynamic disorder, motions (libration, translation, internal vibrations), and systematic error. At ambient temperature, the parameters can be regarded mostly as quantities with contributions from static disorder. With x = 0, the positional displacement of O4 atom was highly anisotropic with the largest magnitude in the c-axis direction [Fig. 4-8(C)], while, with increasing x-value up to 0.085, the displacement became nearly isotropic with the much smaller magnitudes [Figs. 4-8(A) and 4-8(B)]. The reduction in displacement magnitude could be induced by the steady increase of the La2-O4 interatomic distance from 0.2300 nm (x =0) to 0.2314 nm (x = 0.085). The positional disordering of O4 atoms might be closely related to their mobilities at high temperatures, although the relationship still remain unclear, and should be investigated further.

4.2.4 Conclusion

We successfully refined the crystal structures of apatite-type lanthanum silicates $La_{9.33-2x}(SiO_4)_6O_{2-3x}$ with x = 0, 0.06 and 0.085. The g(La1)-, g(La2)- and g(O4)-values steadily decreased with increasing x-value. The $La2O_7$ polyhedron showed a steady contraction in volume with decreasing g(La2)-value from 0.995 to 0.982. On the other hand, the polyhedral volume of $La1O_9$ showed an expansion of about 1.0 % when the g(La1)-value decreased from 0.841 to 0.818. The distinction in site occupancies between La1 [g(La1) < 0.85] and La2 [g(La2) > 0.98] could cause the difference in deformation behavior of the two types of polyhedra.

References

[1] S. Nakayama, T. Kageyama, H. Aono, and Y. Sadaoka, *J. Mater. Chem.*, **5**, 1801-5 (1995).

[2] S. Nakayama and M. Sakamoto, *J. Eur. Ceram. Soc.*, **18**, 1413-18 (1998).

[3] H. Okudera, Y. Masubuchi, S. Kikkawa, and A. Yoshiasa, *Solid State Ionics*, **176**, 1473-78 (2005).

[4] T. Iwata, K. Fukuda, E. Béchade, O. Masson, I. Julien, E. Champion, and P. Thomas, *Solid State Ionics*, **178**, 1523-29 (2007).

[5] J. E. J. Sansom, D. Richings, and P. R. Slater, *Solid State Ionics*, **139**, 205-10 (2001).

[6] J. R. Tolchard, M. S. Islam, and P. R. Slater, *J. Mater. Chem.*, **13**, 1956-61 (2003).

[7] L. León-Reina, E. R. Losilla, M. Martínez-Lara, S. Bruque, and M. A. G. Aranda, *J. Mater. Chem.*, **14**, 1142-49 (2004).

[8] L. León-Reina, E. R. Losilla, M. Martínez-Lara, S. Bruque, A. Lolbet, D. V. Sheptyakow, and M. A. G. Aranda, *J. Mater. Chem.*, **15**, 2489-98 (2005).

[9] J. E. H. Sansom, J. R. Tolchard, M. S. Islam, D. Apperley, and P. R. Slater, *J. Mater. Chem.*, **16**, 1410-13 (2006).

[10] L. León-Reina, J. M. Porras-Vázquez, E. R. Losilla, and M. A. G. Aranda, *Solid State Ionics*, **177**, 1307-15 (2006).

[11] P. J. Panteix, I. Julien, P. Abelard, and D. Bernache-Assollant, *J. Eur. Ceram. Soc.*, **28**, 821-28 (2008).

[12] N. A. Toropov and I. A. Bondar, *Izv. Akad. Nauk SSSR, Ser. Khim.*, **5**, 739-44 (1961).

[13] K. Fukuda, T. Iwata, and E. Champion, *Powder Diffr.*, **21**, 300-3 (2006).

[14] A. N. Christensen, *Z. Kristallogra.*, **209**, 7-13 (1994).

[15] A. M. Dago, D. Y. Pushcharovskii, E. E. Strelkova, E. A. Pobedimskaya, and N. V. Belov, *Dokl. Akad. Nauk SSSR*, 252, 1117-21 (1980).

[16] L. M. Gelato and E. Parthé, *J. Appl. Crystallogr.*, **20**, 139-43 (1987).

[17] L. J. Farrugia, *J. Appl. Crystallogr.*, **30**, 565 (1997).

[18] T. Balic-Zunic and I. Vickovic, *Acta Crystallogr.*, **A29**, 305-6 (1996).

[19] A. Le Bail, H. Duroy, and J. L. Fourquet, *Mater. Res. Bull.*, **23**, 447-52 (1988).

[20] F. Izumi and T. Ikeda, *Mater. Sci. Forum*, **321-324**, 198-203 (2000).

[21] H. Toraya, *J. Appl. Crystallogr.*, **23**, 485-91 (1990).

[22] G. W. Brindley, *Bulletin de la Societe Chimique de France*, D59-63 (1949).

Table 4-3.

Crystal data and structure refinement of $La_{9.33-2x}(SiO_4)_6O_{2-3x}$

| Sample | x | Chemical composition | Unit-cell dimensions | | | Reliability indices |
			a / nm	c / nm	V / nm^3	R_{wp} (S), R_p, R_B and R_F
S-A	0.085	$La_{9.16}(SiO_4)_6O_{1.75}$	0.972492(7)	0.719052(4)	0.588929(7)	5.94 (1.15), 4.58, 1.48 and 0.88
S-B	0.06	$La_{9.21}(SiO_4)_6O_{1.81}$	0.972669(4)	0.718886(2)	0.589007(4)	6.12 (1.24), 4.74, 1.59 and 0.99
S-C	0	$La_{9.33}(SiO_4)_6O_2$	0.972892(3)	0.718475(2)	0.588940(4)	5.53 (1.16), 4.23, 1.83 and 1.11

Table 4-4.

Structural parameters and atomic displacement parameters ($\times 10^{-2}$ nm^2) of La$_{9.33-2x}$(SiO$_4$)$_6$O$_{2-3x}$

Sample	S-A	S-B	S-C
x	0.085	0.06	0
Chemical composition	La$_{9.16}$(SiO$_4$)$_6$O$_{1.75}$	La$_{9.21}$(SiO$_4$)$_6$O$_{1.81}$	La$_{9.33}$(SiO$_4$)$_6$O$_2$
La1, $4f$(1/3, 2/3,z)			
z	0.0009(2)	0.0005(2)	0.0004(2)
occpancy	0.818(2)	0.820(2)	0.841(1)
U_{11}	0.0097(3)	0.0095(2)	0.0112(2)
U_{33}	0.0270(4)	0.0297(4)	0.0283(4)
La2, $6h$ (x, y, 1/4)			
x	0.24455(6)	0.24460(6)	0.24257(6)
y	0.23078(6)	0.23097(5)	0.22986(6)
occpancy	0.982(3)	0.988(2)	0.995
U_{11}	0.0105(3)	0.0092(3)	0.0124(3)
U_{22}	0.0100(3)	0.0100(3)	0.0126(3)
U_{33}	0.0096(2)	0.0097(2)	0.0114(2)
U_{12}	0.0061(2)	0.0050(2)	0.0066(2)
Si, $6h$ (x, y, 1/4)			
x	0.0298(2)	0.0310(1)	0.0326(2)
y	0.4001(2)	0.4008(2)	0.4025(2)
U_{11}	0.0134(19)	0.0064(16)	0.0056(15)
U_{22}	0.0092(14)	0.0072(12)	0.0084(11)
U_{33}	0.0055(11)	0.0087(11)	0.0087(10)
U_{12}	0.0053(14)	0.0025(12)	0.0028(11)
O1, $6h$ (x, y, 1/4)			
x	0.1169(8)	0.1200(6)	0.1227(7)
y	0.5925(5)	0.5933(6)	0.5951(7)
U_{11}	0.0202(37)	0.0171(34)	0.0148(32)
U_{22}	0.0167(39)	0.0243(39)	0.0381(41)
U_{33}	0.0051(36)	0.0047(33)	0.0089(33)
U_{12}	0.0124(32)	0.0113(30)	0.0172(31)
O2, $6h$ (x, y, 1/4)			
x	0.4841(6)	0.4831(5)	0.4843(6)
y	0.1619(6)	0.1607(6)	0.1590(6)
U_{11}	0.0161(41)	0.0151(38)	0.0148(37)
U_{22}	0.0075(36)	0.0228(39)	0.0172(36)
U_{33}	0.0248(44)	0.0230(41)	0.0204(37)
U_{12}	0.0003(29)	0.0030(29)	-0.0034(27)
O3, $12i$ (x, y, z)			
x	0.0877(4)	0.0870(3)	0.0883(4)
y	0.3439(5)	0.3428(4)	0.3442(5)
z	0.0680(2)	0.0679(2)	0.0678(5)
U_{11}	0.0406(32)	0.0383(29)	0.0374(27)
U_{22}	0.0577(36)	0.0419(30)	0.0488(30)
U_{33}	0.0313(31)	0.0196(26)	0.0178(24)
U_{12}	0.0425(29)	0.0305(24)	0.0314(23)
U_{13}	-0.0234(23)	-0.0131(20)	-0.0120(19)
U_{23}	-0.0257(25)	-0.0155(20)	-0.0145(20)
O4, $2a$ (0, 0, 1/4)			
occpancy	0.873	0.907	1
U_{11}	0.0133(37)	0.0104(33)	0.0224(33)
U_{33}	0.0147(56)	0.0298(58)	0.1020(85)

The site symmetries give the constraints: $U_{11}=U_{22}=2U_{12}$, $U_{13}=U_{23}=0$ at La1 and O4 sites; $U_{13}=U_{23}=0$ at La2, Si, O1 and O2 sites.

Table 4-5.

Phase compositions (mol %) determined by the Rietveld method

Sample	Constutient phases			
	$La_{9.33-2x}(SiO_4)_6O_{2-3x}$	m-$La_2Si_2O_7$	t-$La_2Si_2O_7$	La_2SiO_5
S-A	76.8 ($x = 0.085$)	16.7	6.5	ND
S-B	90.6 ($x = 0.06$)	ND	9.4	ND
S-C	99.4 ($x = 0$)	ND	ND	0.6

ND: not detectable.

Table 4-6.

Selected interatomic distances (nm) and angles (°) of $La_{9.33-2x}(SiO_4)_6O_{2-3x}$

Sample	S-A	S-B	S-C
x	0.085	0.06	0
Chemical composition	$La_{9.16}(SiO_4)_6O_{1.75}$	$La_{9.21}(SiO_4)_6O_{1.81}$	$La_{9.33}(SiO_4)_6O_2$
La1-O1 [×3]	0.2577(5)	0.2559(3)	0.2544(4)
La1-O2 [×3]	0.2496(4)	0.2501(3)	0.2500(4)
La1-O3 [×3]	0.2880(4)	0.2890(3)	0.2878(4)
Mean	0.265	0.265	0.264
La2-O1	0.2477(4)	0.2495(4)	0.2512(5)
La2-O2	0.2727(6)	0.2727(4)	0.2762(6)
La2-O3 [×2]	0.2446(3)	0.2442(2)	0.2451(3)
La2-O3' [×2]	0.2633(2)	0.2629(2)	0.2622(4)
La2-O4	0.23142(5)	0.23157(4)	0.23006(4)
Mean	0.253	0.253	0.253
Si-O1	0.1623(4)	0.1624(5)	0.1624(6)
Si-O2	0.1624(4)	0.1624(4)	0.1624(6)
Si-O3 [×2]	0.1624(2)	0.1623(2)	0.1624(4)
Mean	0.162	0.162	0.162
O1-Si-O2	110.7(3)	111.47(2)	111.5(3)
O1-Si-O3 [×2]	108.6(2)	108.8(1)	108.7(2)
O2-Si-O3 [×2]	110.7(2)	110.1(1)	110.2(2)
O3-Si-O3	107.47(2)	107.46(3)	107.5(3)
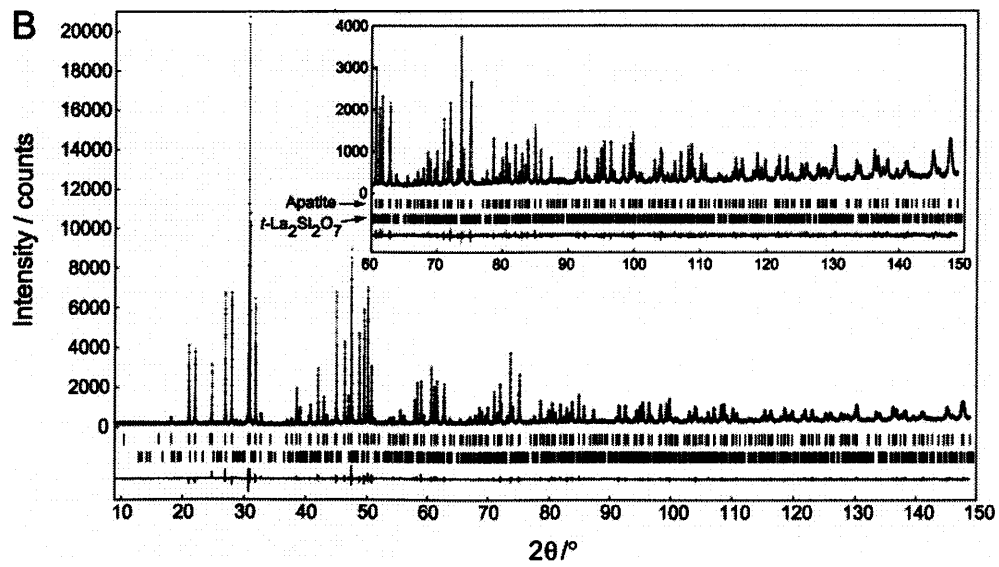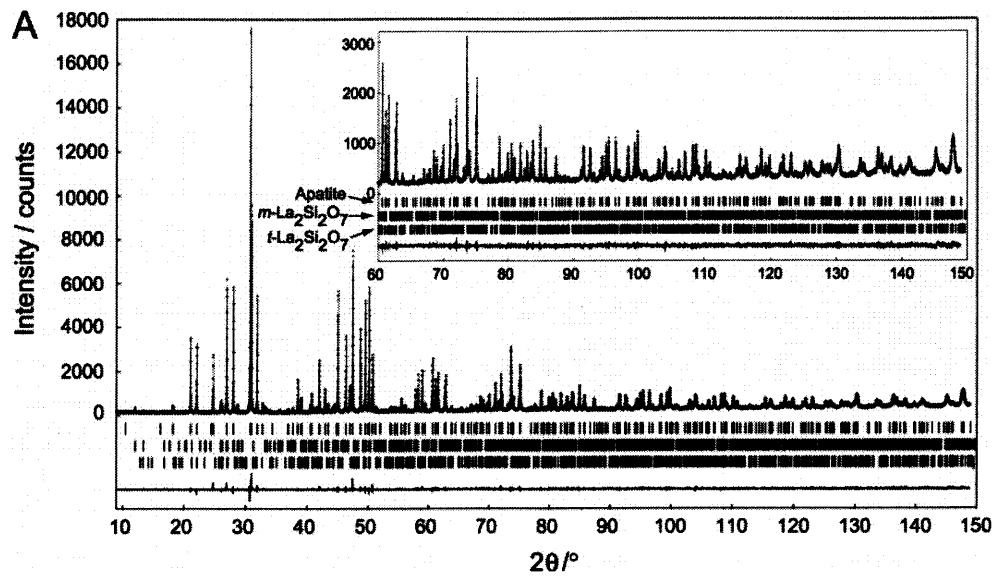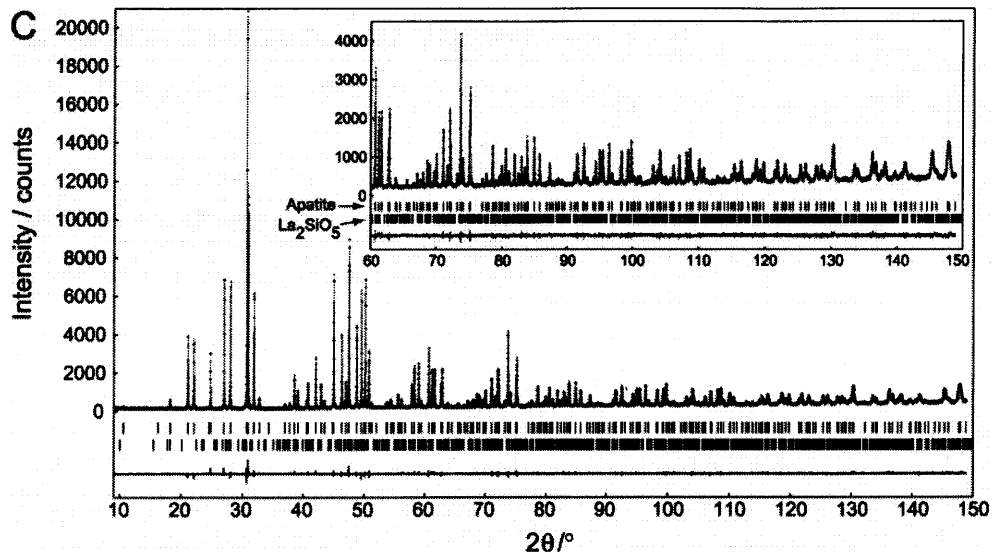
Fig.4-7. Comparison of the observed diffraction patterns (symbol: +) with the corresponding calculated patterns (upper solid line). The difference curve is shown in the lower part of each diagram. The vertical bars indicate the positions of possible Bragg reflections. The profile intensities collected for (A) S-A, (B) S-B and (C) S-C.
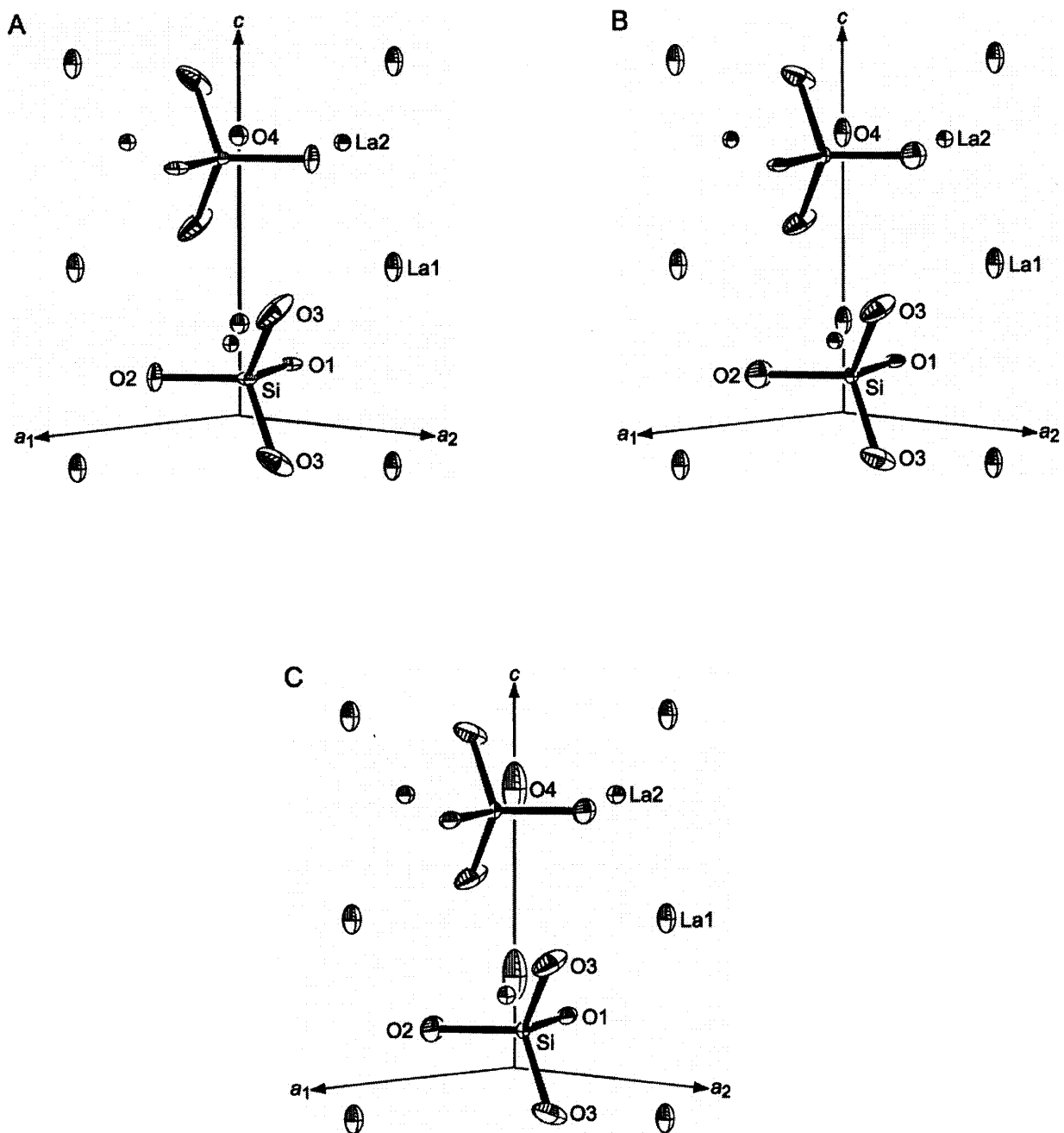
Fig.4-8. ORTEP diagrams of (A) $La_{9.16}(SiO_4)_6O_{1.75}$ ($x = 0.085$) in S-A, (B) $La_{9.21}(SiO_4)_6O_{1.81}$ ($x = 0.06$) in S-B and (C) $La_{9.33}(SiO_4)_6O_2$ ($x = 0$) in S-C. Thermal ellipsoids represent 50% of probability.
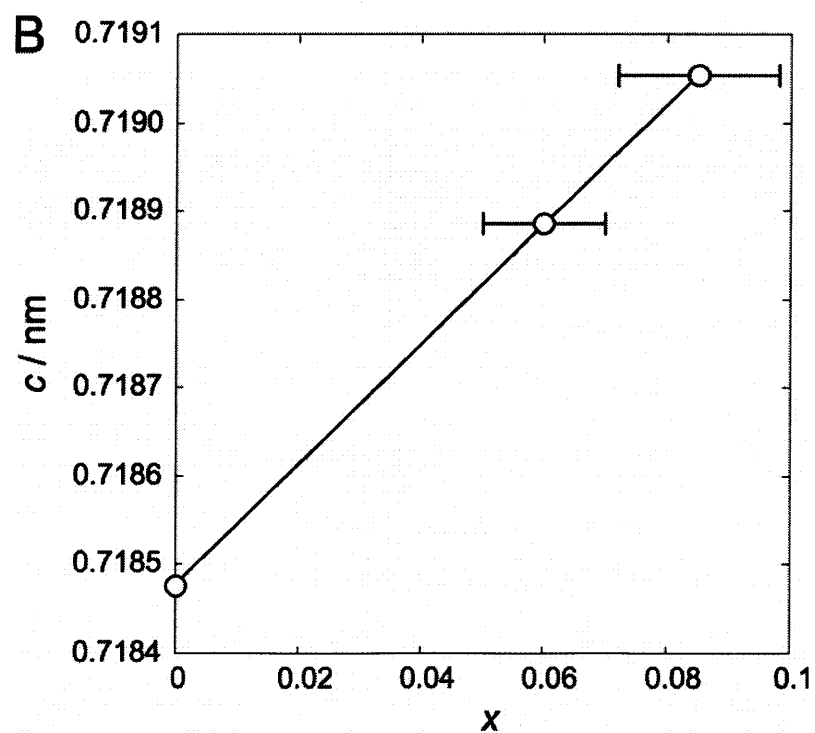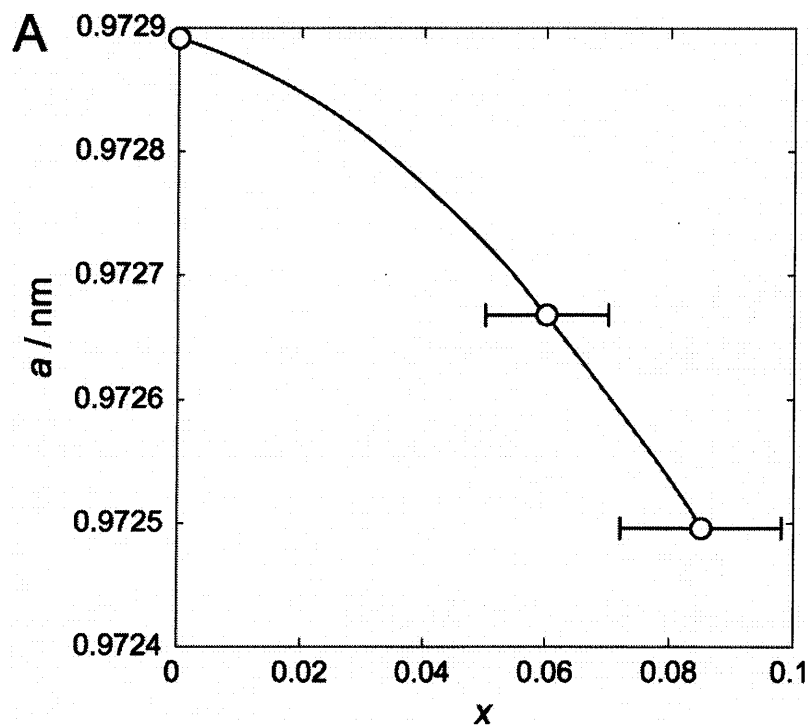
Fig.4-9. Changes of cell dimensions with x-value for $La_{9.33-2x}(SiO_4)_6O_{2-3x}$. (A) a-axis and (B) c-axis.
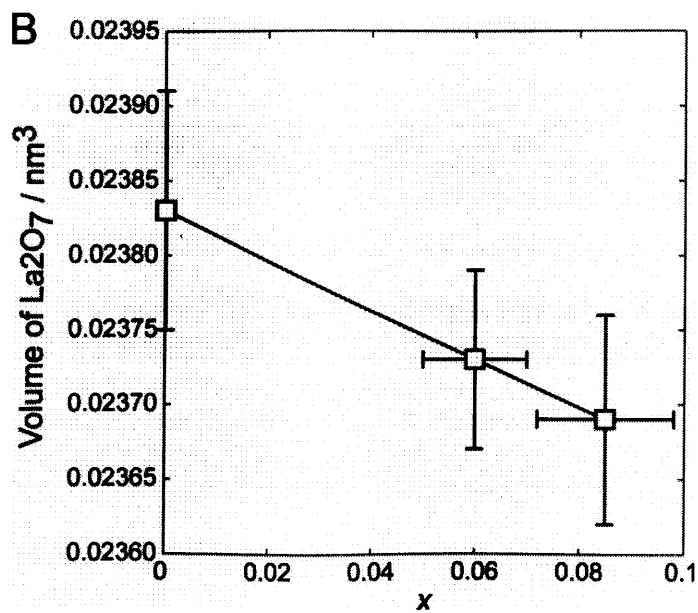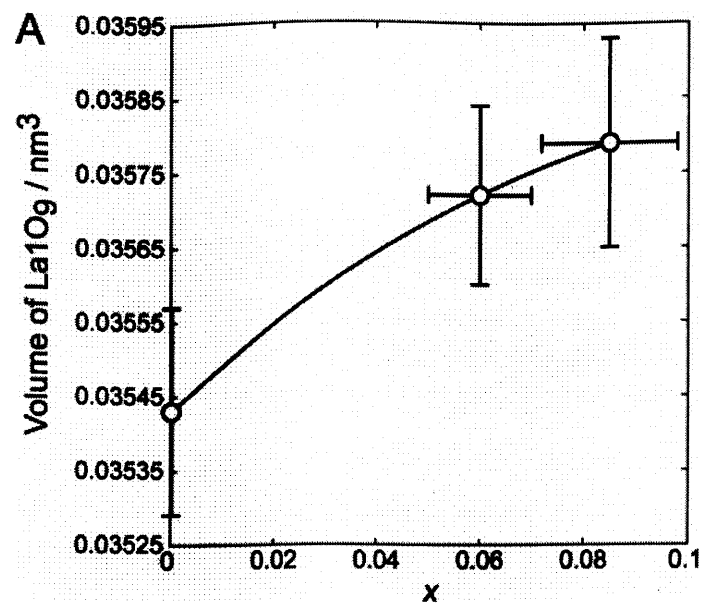
Fig.4-10. Changes of polyhedral volumes with x-value for (A) La1O$_9$ and (B) La2O$_7$ in La$_{9.33-2x}$(SiO$_4$)$_6$O$_{2-3x}$. The polyhedral volumes determined from calculation using the computer program IVTON.[18]
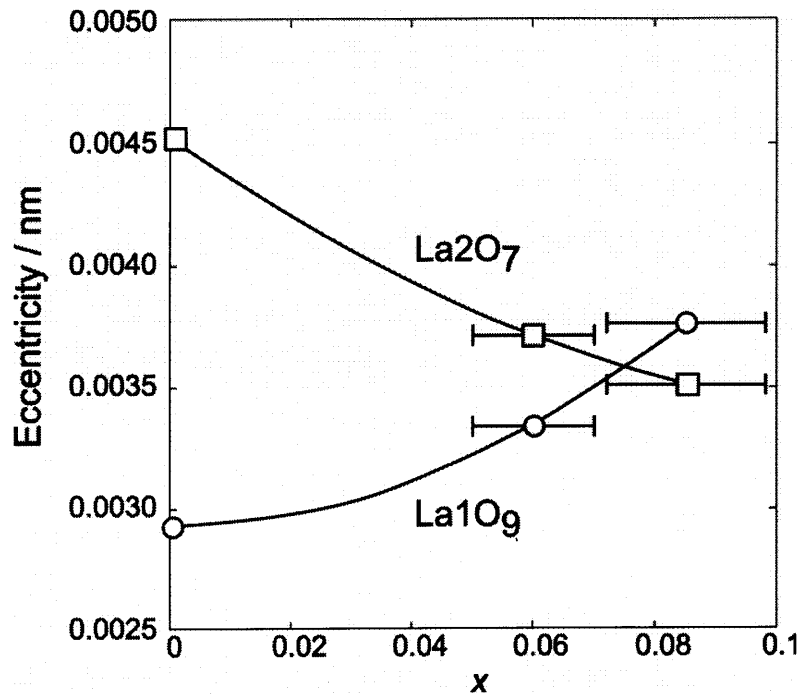
Fig.4-11. Changes of eccentricity with x-value for $La1O_9$ and $La2O_7$ in $La_{9.33-2x}(SiO_4)_6O_{2-3x}$. The eccentricity values determined from calculation using the computer program IVTON.[18]
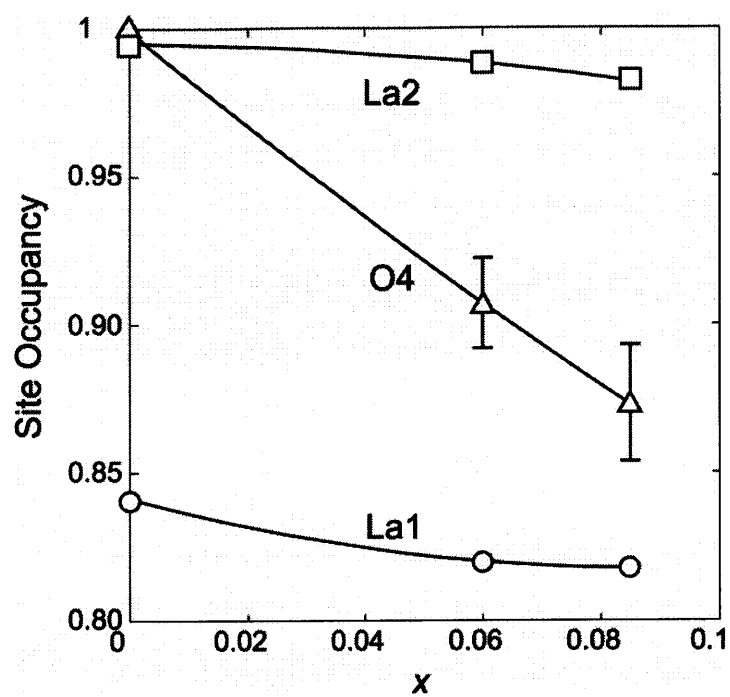
Fig.4-12. Changes of occupancies in La1, La2 and O4 sites with x-value for $La_{9.33-2x}(SiO_4)_6O_{2-3x}$.
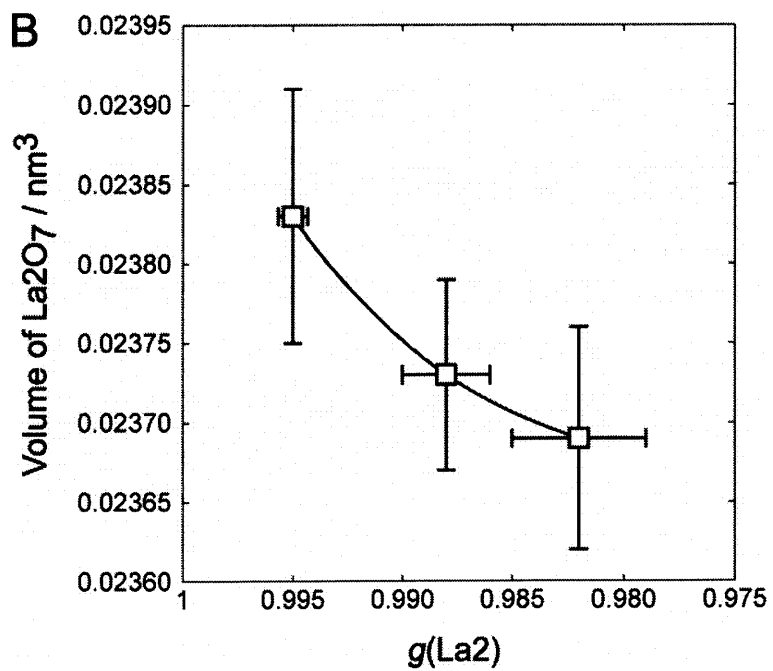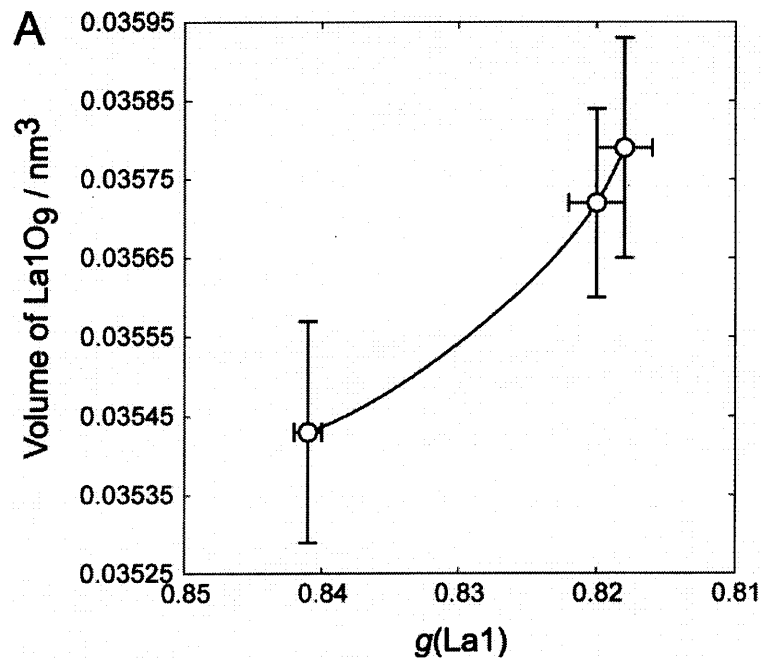
Fig.4-13. Changes of polyhedral volumes with site occupancies for (A) La1O$_9$ and (B) La2O$_7$ in La$_{9.33-2x}$(SiO$_4$)$_6$O$_{2-3x}$. The polyhedral volumes determined from calculation using the computer program IVTON.[18]

Chapter 5

Summary

In Chapter 1, the methodology, background and objectives of the dissertation were introduced. In Capter 2, the author explained the advantages of the combined use of the Rietveld method, the maximum-entropy method (MEM) and the MEM-based pattern fitting (MPF) method, which enabled us to disclose new structural details. Crystal structures were clearly from electron-density distributions determined by MPF. The author applied these methods to clarify the structural details of $Ca_{12}Al_{14}O_{32}Cl_2$ and $Ba_3MgSi_2O_8$. In Chapter 3, the author, for the first time, synthesized five types of layered carbides, $ZrAl_4C_4$, $ZrAl_8C_7$, $Zr(Al,Si)_8C_7$, $Zr(Al,Si)_4C_4$ and $[Al_{16.8}Si_{1.2}][O_{3.0}C_{11.0}]$. All of these crystal structures were sucessfully determined by XRPD method. The last compound was found to show complicated structural disorder induced by twinning. The split-atom model was constracted and subsequently verified by the three-dimensional electron density distributions, which was determined by MEM. Finally, in Chapter 4, the author characterized the crystal structures of oxide-ion-conducting lanthanum silicates from XRPD data to clarify the conducting mechanism.

List of publications

1) T. Iwata and K. Fukuda, "Analysis of Unknown and Disordered Structures from Laboratory X-Ray Powder Diffraction Data (in Japanese)," *Ceramics*, **43**, 929-932 (2008).

2) T. Iwata, M. Haniuda and K. Fukuda, "Crystal Structure of $Ca_{12}Al_{14}O_{32}Cl_2$ and Luminescence Properties of $Ca_{12}Al_{14}O_{32}Cl_2{:}Eu^{2+}$," *J. Solid State Chem.*, **181**, 51-55 (2008).

3) T. Iwata, T. Horie and K. Fukuda, "Reinvestigation of crystal structure and structural disorder of $Ba_3MgSi_2O_8$," *Powder Diffr.*, **24**, 180-184 (2009).

4) T. Iwata, E. Hattori, S. Hashimoto and K. Fukuda, "Synthesis and Crystal Structure of a New Layered Carbide $ZrAl_4C_4$," *J. Am. Ceram. Soc.*, **91**, 2713–2715 (2008).

5) T. Iwata, K. Sugiura, S. Hashimoto and K. Fukuda, "Synthesis and Crystal Structure of a New Layered Carbide $ZrAl_8C_7$," *J. Am. Ceram. Soc.*, **91**, 3758-3761 (2008).

6) T. Iwata, E. Hattori, K. Sugiura, S. Hashimoto, H. Nakano and K. Fukuda, "Syntheses and Crystal Structures of Si-Bearing $ZrAl_4C_4$ and $ZrAl_8C_7$," *J. Ceram. Soc. Jpn*, **117**, 37-41 (2009).

7) T. Iwata, M. Kaga, H. Nakano and K. Fukuda, "First Discovery and Structural Characterization of a New Compound in Al-Si-O-C System," *J. Solid State Chem.*, **182**, 2252-2260 (2009).

8) T. Iwata, K. Fukuda, E. Béchade, O. Masson, I. Julien, E. Champion and P. Thomas, "Structural Change of Oxide-Ion-Conducting Lanthanum Oxyapatite on Heating from 295 to 1073 K," *Solid State Ionics*, **178**, 1523-1529 (2007).

9) T. Iwata, E. Béchade, K. Fukuda, O. Masson, I. Julien, E. Champion and P. Thomas, "Lanthanum and Oxygen Deficient Crystal Structures of Apatite-Type Silicates," *J. Am. Ceram. Soc.*, **91**, 3714-3720 (2008).

10) K. Fukuda, M. Hisamura, T. Iwata, N. Tera and K. Sato, "Synthesis, Crystal Structure and Thermoelectric Properties of a New Carbide $Zr_2[Al_{3.56}Si_{0.44}]C_5$," *J. Solid State Chem.*, **180**, 1809-1815 (2007).

12) K. Fukuda, M. Hisamura, Y. Kawamoto and T. Iwata, "Synthesis, Crystal Structure and Thermoelectric Properties of a New Layered Carbide $(ZrC)_3[Al_{3.56}Si_{0.44}]C_3$," *J. Mater. Res.*, **22**, 2888-2894 (2007).

Acknowledgments